University of Oklahoma

Graduate College

III-V and Thin Film Photovoltaics for Extraterrestrial Application

A DISSERTATION

SUBMITTED TO THE GRADUATE FACULTY

in partial fulfillment of the requirements for the

Degree of

Doctor of Philosophy

By

COLLIN RICHARD BROWN
Norman, Oklahoma
2019

III-V and Thin Film Photovoltaics for Extraterrestrial Application

A DISSERTATION APPROVED FOR THE
HOMER L. DODGE DEPARTMENT OF PHYSICS AND ASTRONOMY

BY THE COMMITTEE CONSISTING OF

Dr. Ian R. Sellers, Chair

Dr. Michael B. Santos

Dr. Lloyd A. Bumm

Dr. Arne Schwettmann

Dr. Bin Wang

Acknowledgements

I am extremely grateful to have worked with Dr. Ian Sellers as my adviser over these past years, for the many enlightening conversations we have had, and for the direction and guidance in my research career.

Dr. Vincent Whiteside has been a great support to the group and to me personally over these years. I am grateful for his experimental expertise, and his passing on those skills to those around him.

I thank my committee members, Dr. Michael Santos, Dr. Lloyd Bumm, Dr. Arne Schwettmann, and Dr. Bin Wang for their support, collaboration, and guidance through my graduate career.

I have had many wonderful opportunities to work with great people in Dr. Sellers lab, both former and current members of the group. I would like to thank Dr. Yang Cheng, Dr. Hamidreza Esmaielpour, Mr. Michael Whitaker, Mr. Anthony Meleco, Mr. Joshua Corona, Mr. Jinfeng Tang, Dr. Brandon Durant, Mr. Hadi Afshari, Mr. Shashi Sourabh and Mr. Kyle Dorman for their friendship, input and collaboration. I have also had the pleasure of working with many great undergraduate students, and I thank Mr. Tyler Erickson, Ms. Hannah Harrell, Mr. Jesse Aragon de Galvez, Mr. Nathan Lydick, Mr. Johannes Byle, and Ms. Ally Dicarlo for their support and contribution to the research here.

I am grateful for many fruitful collaborations over my years at OU, and I thank Dr. Khalid Hossain, Dr. Mangal Dhoubhadel, and Dr. Terry Golding at Amethyst Research Inc., Dr. Joseph Tischler, Dr. Chase Ellis, Dr. Evan Glaser, and Mr. Dave Scheiman at the Naval Research Laboratory, Dr. Dmitry Poplavskyy formerly at Miasolé Hi-Tech Corp., Dr.

Seth Hubbard and Dr. Steven Polly at NanoPower Research Labs, Dr. Mathieu Leroux and Dr. Mohamed Al Khalfioui at CNRS-CRHEA, Dr. Giles Eperon at the National Renewable Energy Laboratory, Mr. Jeremiah McNatt at NASA Glenn Research Center, Dr. Nicholas Materer at Oklahoma State University, Dr. Paremeswar Harikumar at the University of Tulsa, and Ms. Tong Mou at University of Oklahoma.

I would like to thank the members of the Graduate Recruiting and Selection committee, for their understanding and for offering me a chance to prove myself here at the University of Oklahoma.

Last, but not least, I thank my wonderful, beautiful wife, Jennifer, for supporting me through these past years. I am grateful for her effort in bearing and raising our three children we have welcomed in my time here. The joy and pride I feel in my family has been an incalculable driving force in pushing forward my research.

My research over my time here has been funded by the NASA EPSCoR program (Grant #NNX16AQ97A). While not directly supported by any other grants, I have worked on projects funded by OCAST grants (Grant OARS 12.2-040 and OARS AR18-052-1), and by an NSF grant (DMR-1305770). I express my gratitude to the funding agencies responsible.

Table of Contents

List of Tables

List of Figures

List of Publications

1. **C. R. Brown**, V. R. Whiteside, D. Poplavskyy, K. Hossain, M. Dhoubhadel, and I. R. Sellers, "Flexible Cu(In,Ga)Se_2 Solar Cells for Outer Planetary Missions: Investigation Under Low-Intensity Low-Temperature Conditions," *IEEE Journal of Photovoltaics*, vol. 9, no. 2, pp. 552-558, Mar. 2019.

2. **C. R. Brown**, G. E. Eperon, V. R. Whiteside, and I. R. Sellers, "Potential of High-Stability Perovskite Solar Cells for Low-Intensity–Low-Temperature (LILT) Outer Planetary Space Missions," *ACS Applied Energy Materials*, vol. 2, no. 1, pp. 814-821, 2019.

3. **C. R. Brown**, N. J. Estes, V. R. Whiteside, B. Wang, K. Hossain, T. D. Golding, M. Leroux, M. Al Khalfioui, J. G. Tischler, C. T. Ellis, E. R. Glaser, and I. R. Sellers, "The effect and nature of N-H complexes in the control of the dominant photoluminescence transitions in UV-hydrogenated GaInNAs," *RSC Advances*, vol. 7, no. 41, pp. 25353-25361, 2017.

4. T. Mou, S. Li, **C. R. Brown**, V. R. Whiteside, K. Hossain, M. Al Khalfioui, M. Leroux, I. R. Sellers, and B. Wang, "Role of In in Hydrogenation of N-Related Complexes in GaInNAs," *ACS Applied Electronic Materials*, vol. 1, no. 4, pp. 461-466, 2019.

5. H. Afshari, B. K. Durant, **C. R. Brown**, K. Hossain, D. Poplavskyy, and I. R. Sellers, "Role of metastability and concentration in the performance of CIGS solar cells under LILT conditions", In Preparation.

List of Presentations

Below is a list of the presentations or posters I have presented at conferences.

1. **C. R. Brown**, H. Afshari, V. R. Whiteside, D. Poplavskyy, K. Hossain, M. Dhoubhadel, and I. R. Sellers, "Effect of Low-Intensity-Low-Temperature and High Radiation conditions on Flexible Cu(In,Ga)Se_2 Solar Cells " *2019 IEEE 46th Photovoltaic Specialists Conference (PVSC), Chicago, 2019 poster.*

2. **C. R. Brown**, G. E. Eperon, V. R. Whiteside, and I. R. Sellers, "An Assessment of Perovskite Solar Cells for Low-Intensity-Low-Temperature (LILT) Space Missions" *2019 IEEE 46th Photovoltaic Specialists Conference (PVSC), Chicago, 2019 talk.*

3. **C. R. Brown**, V. R. Whiteside, D. Poplavskyy, K. Hossain, M. Dhoubhadel, and I. R. Sellers, "Flexible Cu(In,Ga)Se_2 Solar Cells for Outer Planetary Missions—Investigation Under Low Intensity Low Temperature Conditions" *2019 MRS Spring Meeting & Exhibit, Phoenix, 2019 poster.*

4. **C. R. Brown**, G. E. Eperon, V. R. Whiteside, and I. R. Sellers, "Potential of High Stability Perovskite Solar Cells for Low-Intensity-Low-Temperature (LILT) Outer Planetary Space Missions " *2019 MRS Spring Meeting & Exhibit, Phoenix, 2019 talk.*

5. **C. R. Brown**, V. R. Whiteside, D. Poplavskyy, K. Hossain, M. Dhoubhadel, and I. R. Sellers, "An investigation of flexible Cu(In,Ga)Se_2 solar cells under low intensity low temperature for potential application for outer planetary missions" *Space Photovoltaic Research and Technology Conference, NASA Glenn Research Center, Cleveland, 2018 talk.*

6. N. J. Estes, M. Fukuda, V. R. Whiteside, B. Wang, **C. R. Brown**, K. Hossain, T. D. Golding, M. Leroux, M. Al Khalfioui, J. G. Tischler, C. T. Ellis, E. R. Glaser, and I. R. Sellers, "The role of N-H complexes in the control of localized center recombination in hydrogenated GaInNAs" *2019 SPIE Photonics West, San Fransisco, 2017 talk.*

7. **C. R. Brown**, V. R. Whiteside, I. R. Sellers, A. Petrou, W-C. Chou, "Dynamics of the matrix in DMS Type-II quantum dot systems" *2016 APS March Meeting, Baltimore, 2016 talk.*

8. D. D. Allred, R. R. Vanfleet, J. K. Anderson, **C. R. Brown**, R. S. Hansen, D. McKenna, R. C. Davis, "Preparation and Characterization of CVD & ALD Tungsten & Molybdenum Thin Films for CNT-M Metallic Microstructures" *AVS 60th International Symposium & Exhibition, Long Beach, 2013 talk.*

Abstract

Photovoltaic power is one of the few options available for electrical devices stationed outside of our atmosphere. As the satellite market turns to smaller satellites based on the CubeSat and SmallSat form factor, these limited size vehicles need enough power to complete their missions. Costs over mission lifetime also need to remain competitive when considering the typically shorter mission lifespan of these CubeSats. Increasing efficiency of current space photovoltaics while maintaining cost is one approach to this problem, though using flexible thin film solar arrays is an additional low-cost option that may still meet the power requirements under certain conditions.

Increasing the number of junctions in a multijunction solar cell is the direct approach to increase efficiency, and the quaternary GaInNAs has long been suggested as a fourth junction in the standard GaInP/GaAs/Ge cells, though material quality issues have prevented its penetration into the commercial sector. Here, optical GaInNAs samples carefully hydrogenated via a UV-activated process show evidence of impurity and defect passivation, completely removing the 's-shape' in the temperature dependent photoluminescence, while retaining the lower band gap that results from nitrogen incorporation. Radiative recombination is dominated by the free-excitonic transition, rather than emission due to carriers localized by non-ideal alloy fluctuations, as is common in this material system at low temperature. Density functional theory simulations show the elimination of N and Ga associated defect levels by hydrogenation, where the formation of N-H bonds act as donors. At higher hydrogenation concentrations, levels from Ga-H_2-N complexes are pushed into the conduction band. These

hydrogen complexes and the change in the band structure can explain the reduced emission observed from localized centers.

Two thin film PV technologies, $Cu(In,Ga)Se_2$ (CIGS) solar cells and triple cation based perovskite solar cells, are both assessed under low-intensity-low-temperature (LILT) conditions consistent with orbits around Saturn, Jupiter, and Mars. Under these extreme conditions, evidence of unintentional barriers is observed in both material systems, though photovoltaic performance is relatively unaffected. In the CIGS devices, evidence of this photo-activated barrier appears consistent with metastable defect complexes and the CIGS/CdS interface. A similar interface appears responsible for the low fill factor in the perovskite solar cells at low temperature, where thermionic emission limits carrier extraction. Low intensity illumination reveals a recovery of the fill factor and efficiency, suggesting the potential of these devices in deep space conditions even in situations where sample degradation can occur in transit. CIGS devices studied here show no issues under thermal cycling measurements, and the perovskite devices demonstrated stability via temperature dependent photoluminescence, where no phase change was observed. Proton-irradiation experiments were performed on the CIGS devices, where degradation and subsequent self-healing from annealing conditions was observed. These results show promise for CIGS and Perovskite solar cells in space, individually and perhaps in tandem/multijunction applications.

Finally, InP based devices have shown greater radiation tolerance than other III-V materials, and the addition of quantum confined structures has also shown to increase this behavior. To further investigate this, Type II InP/InAlAs quantum well devices are grown by MOCVD, and investigated via photoluminescence, current density-voltage, external quantum efficiency, and photoreflectance measurements. Photovoltaic behavior is observed,

and investigation into the various interface transitions is performed to better understand the physics in these devices.

Chapter 1

Introduction

1.1 Solar Power in Space

While photovoltaics are becoming an increasingly important part of the energy landscape terrestrially, for off world power solutions solar power is one of the few options available, and has been used in space since 1958 with Vanguard I [1], [2]. Batteries, nuclear power, and fuel cells are some of the only alternatives. Batteries can be used as a main power source, but are limited in capacity and thus are only used for probes that are designed to have a very short lifetime. Batteries are also included on satellites that use solar power to provide power when the satellite is eclipsed by the earth or other body it is orbiting.

Nuclear power in the form of radio-isotope thermoelectric generators (RTG) has seen widespread use on space probes, from the Voyager satellites now in interstellar space to the Mars Science Laboratory named Curiosity [3], [4]. RTGs do not rely on the sun for power, and provide a steady, but small, source of power for an extended period of time. However, RTGs traditionally use plutonium-238 as the fuel source, with material coming from reactors that were used for weapons production. As nuclear weapons are no longer being produced, the production of plutonium-238 ceased for a number of years. NASA's supply of this fuel source is dwindling, though efforts are underway to produce more plutonium-238, with Oak Ridge National Laboratory recently producing 50 grams of new material after a gap of almost 30 years [5]. Higher power fission reactors for space exploration are also under investigation, with more plentiful uranium-235 being used as the fuel source [6]. Regardless, because of

the limited supply, power output, and weight of RTGs coupled with various space mission requirements, research continues on solar power options for both smaller and deeper space probes.

Most satellites powered by solar power use multijunction solar cells based on III-V semiconductors, with the notable exception of silicon panels on the International Space Station [7]. Multijunction photovoltaics are currently the most efficient solar cells with record efficiencies of 39.2% under standard conditions, and even greater efficiency under concentration [8]. With processing techniques like inverted metamorphic growth (IMM) [9] and epitaxial lift off (ELO) [10] these solar cells can also be made to be quite lightweight and flexible. However, in comparison to thin film photovoltaics, multijunctions are relatively susceptible to radiation damage, which requires thick cover glass to allow the solar arrays to achieve a sufficient end of life (EOL) efficiency [11].

Additionally, multijunctions can be quite expensive in comparison to silicon and other terrestrial solar options [12]. As the satellite market turns to massive constellations of smaller and shorter life satellite networks from companies like SpaceX, OneWeb, Amazon, Facebook and others [13], it may be reasonable to use cheaper flexible solar power alternatives like perovskites or CIGS.

In order to be competitive, these cheaper power options must be able to compete in terms of array mass specific power, which is a function of array specific power, array area density, cell efficiency and packing factor [14]. This array mass specific power is the amount of power produced per unit mass, and is particularly important for satellites as each extra kilogram increases launch costs. A cheaper solar cell may be competitive if it is lightweight and flexible enough for good packing, even if the cheaper solar cell has lower efficiency.

1.2 Solar Cell Basics

1.2.1 Semiconductor Basics

From quantum mechanics, we have learned that atoms have discrete energy levels, and electrons in atoms must occupy those energy levels. This model is consistent with atoms that are well separated from their neighbors, such as gases. However, as atoms are brought into close proximity, a periodic crystal structure forms and the energy levels overlap forming a periodic potential for the electrons. This periodic potential results in the large bands of states as the atomic spacing is decreased, as shown in Figure 1.1. The nature of gaps between the bands of states is what allows semiconductor technology and our modern world to function.

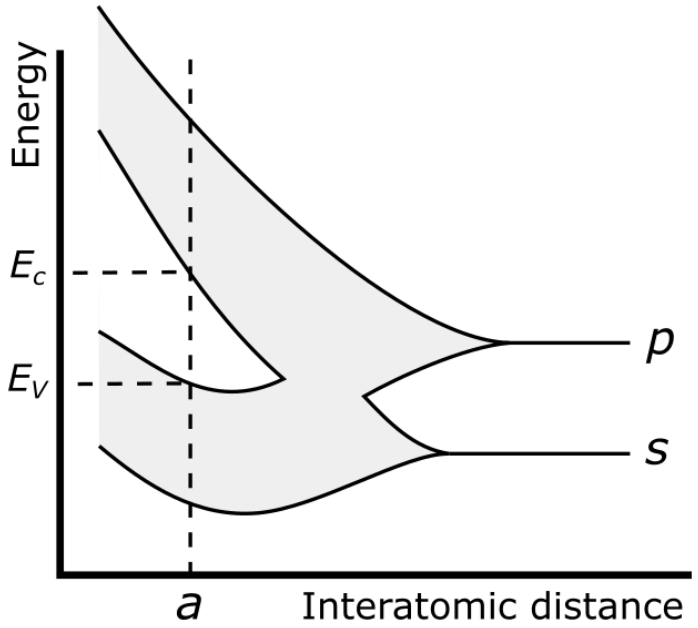

Figure 1.1: Figure of energy levels and bands with respect to atomic spacing. Figure adapted from [15]

The bottom band of states is known as the valence band (E_{V} or VB), and in a semiconductor this band is usually completely filled with electrons. The upper band is known as the conduction band (E_{C} or CB). When a semiconductor interacts with a photon of light that has energy greater than the energy separation of the bands (band gap), then the photon is absorbed and an electron is excited from the valence band to the conduction band. The empty state left behind is referred to as a "hole", and behaves like an electron, but with a positive charge and a negative effective mass. These electrons in the conduction band and holes in the valence band are free to move about, and are influenced by external factors like electric and magnetic fields.

Most pure semiconductors have limited conductivity because of this filled valence band, where limited thermal excitation across the gap is the source of mobile charge carriers. This semi-insulating nature can be changed by introducing other atoms which contain a different number of electrons in their valence shell than the host material. For example, silicon has 4 electrons that occupy the valence shell, and so atoms such as boron or aluminum with 3 electrons in the valence shell are introduced to subtract electrons, essentially adding holes to the system. This is known as p-type doping. In the same manner, atoms like phosphorus or arsenic with 5 electrons in the valence shell are added to introduce extra electrons into the system, which is known as n-type doping. The dopants are known as acceptors for p-type and donors for n-type, referring to their proclivity to accept or donate an electron.

1.2.2 P-N Junction

Many photovoltaic devices use what is known as a p-n junction, where two regions of the semiconductor are doped to be p-type and n-type respectively. The region where these doped

layers meet is the junction. At the junction, free electrons and free holes from the respective doped layers are free to diffuse into the opposite layer. The free electrons from the n-doped layer diffuse into the p-doped layer, and are able to fill the holes located at acceptor sites. This results in positively charged ions in the n-doped layer, and negatively charged ions in the p-doped layer, which then prevent further diffusion of charges, as the electric field increases, shown in Figure 1.2. The region over which this phenomenon occurs is known as the depletion width, or space-charge region.

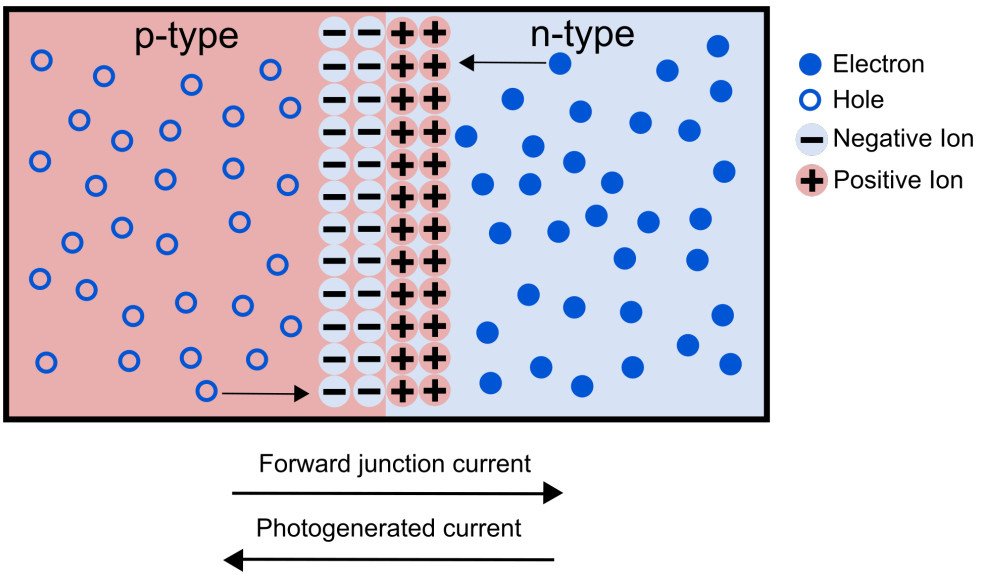

Figure 1.2: A schematic of the depletion width that forms in a p-n junction. The free carriers diffuse to the opposite sides of the junction, and then passivate the dopants, leading to stationary ions.

Due to these internal stationary ions, the space-charge region behaves somewhat like a parallel plate capacitor, where the distance between the plates is the width of this region. This space-charge region generates an electric field and built-in potential. In a solar cell, this internal electric field serves to separate photogenerated electrons and holes, and direct them

to the appropriate contacts. This electric field also prevents majority carriers (electrons in n-layer, holes in p-layer) from flowing, though applying an external bias to this junction can overcome this internal field, and allow the junction to pass current. This p-n junction forms a diode, and is the basis for all optoelectronic devices.

1.2.3 Charge Carrier Generation and Transport

In a solar cell, incident photons are absorbed by the main semiconductor material, whereby an electron is excited into the conduction band, leaving a hole in the valence band. These photogenerated electrons and holes in a solar cell are referred to as minority carriers, in that they are the minority species of carrier in the layer in which they are generated (electrons in p-layer, holes in n-layer). This refers to the relative concentration of electrons and holes in each layer, though typically there are significant amounts of both carrier type.

The electric field that results from the depletion region of the p-n junction produces a force on these charged particles, moving the electrons toward the n-layer and the holes toward the p-layer. This movement of carriers within the electric field is known as drift, while movement without an electric field is more random in nature. This more random movement is known as diffusion, where carriers move from regions of high concentration to regions of low concentration. Both of these methods of transport are present in solar cells, though diffusion transport can be limited if numerous defects and recombination centers are present.

These minority carriers, once they reach the depletion region, are swept to the opposite side of the junction where they are then majority carriers. Through diffusion these carriers can then be extracted at the contacts and result in a reverse or negative current as compared to the forward current flow of the diode. Current flow for these processes (according to

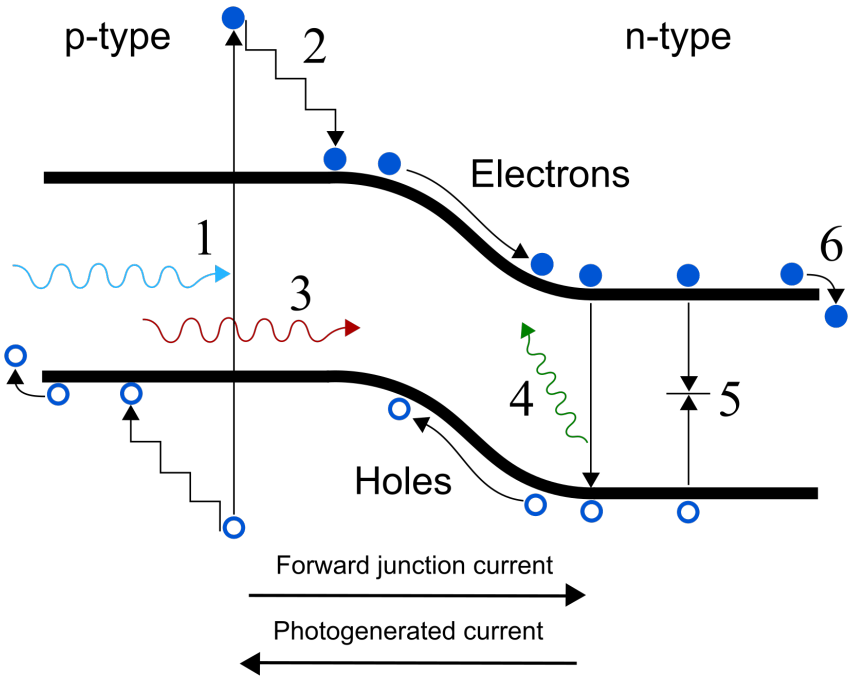

Figure 1.3: A schematic of a p-n junction with relevant processes labeled. (1) Absorption of high energy photons. (2) Thermalization of high energy carriers with the crystal lattice. (3) Transmission of below band gap photons. (4) Radiative recombination. (5) Defect mediated or non-radiative recombination. (6) Contact loss.

convention) are depicted by arrows in Figure 1.2 and 1.3. Competition between this reverse photogenerated current and the forward current of the diode results in a point where no current flows known as the open-circuit voltage, which will be explained further in the next chapter.

1.2.4 Fundamental Losses in a Solar Cell

Due to the nature of the band gap of a semiconductor, absorption and extraction of energy from light works best when the light absorbed is roughly the same energy as the band gap.

When designing detectors, for example in the telecommunications industry, material for a detector can be easily found that provides high efficiency for the relatively few wavelengths of light being detected. However, the sun is a blackbody emitter, and so emits light in a broad swath of the electromagnetic spectrum, rather than a single wavelength. This mismatch between the solar spectrum and the absorption of a semiconductor leads to a number of fundamental losses, some of which are shown in Figure 1.3. The first is below gap transmission, as light with energy lower than the band gap is not absorbed. Light with energy greater than the band gap is absorbed, but the extra energy imparted by the high energy photons is rapidly lost as the high energy carriers interact with vibrations in the crystal lattice generating heat, and relax down to the band edge. Additional losses come from the ability of the semiconductor to re-emit or radiate light if carriers recombine. In lower quality material, defects can trap carriers, causing losses in the form of non-radiative recombination. Finally, there is inherent loss at extraction, as the voltage is defined by the quasi fermi level separation at the contacts, which is always somewhat less than the full band gap.

As we can see from Figure 1.4, the major losses are in the form of below gap transmission and above gap thermalization. In the first case, semiconductor material with a lower band gap could be chosen, which would allow for more light to be absorbed and more current produced. However, the lower band gap would reduce the maximum voltage possible. From Ohm's law, we know power is the product of current and voltage, and thus there is a fundamental trade off. This fundamental limit is known as the detailed balance limit and was first put forth by Shockley and Quiesser in 1961 [16]. They showed that there was an preferred value for the band gap of photovoltaic devices of around 1.32 eV, where the tradeoff between voltage and current is optimized.

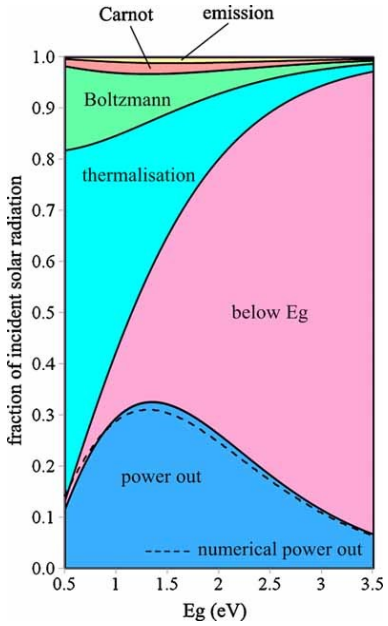

Figure 1.4: Loss processes vs Band Gap (Eg). Reproduced with permission from: L. C. Hirst and N. J. Ekins-Daukes, "Fundamental losses in solar cells," *Progress in Photovoltaics: Research and Applications*, vol. 19, no. 3, pp. 286–293, 2011. [Online]. Available: `https://onlinelibrary.wiley.com/doi/abs/10.1002/pip.1024` [17]

There are many research groups now who not only study and improve traditional photovoltaics, but also are investigating means of increasing the efficiency of solar cells past this limit. Multijunction solar cells, as have been mentioned previously, are one method to bypass this limit. Multiple solar junctions are stacked in series, where each absorbs a different portion of the solar spectrum. Each junction is tuned to produce the same current, and the voltage of each junction adds together. This method of bypassing the limit has been very successful, and commercial devices are available, though their cost limits their application to concentrator and extraterrestrial application [12].

Hot carrier and intermediate band solar cells are two other methods currently under investigation to bypass the fundamental limit. Intermediate band solar cells attempt to realize a multijunction solar cell in a single device by introducing a well confined intermediate band [18]. This intermediate band would allow for the absorption of more below main gap photons, but the confinement should mean that the voltage is still defined by the main gap. Hot carrier solar cells attempt to limit the thermalization process and extract the energy of the high energy photons. Band engineering is used to limit the effect of lattice vibrations on the electrical carriers [19]. Thus, the band gap could be lowered to absorb more of the solar spectrum, but the voltage would be defined by the hot carrier energy. It should be noted that these concepts are challenging to implement in devices, and to date, no intermediate band or hot carrier solar cells have been demonstrated.

1.3 Space Environmental Considerations

1.3.1 Orbital Solar Intensity and Solar Array Temperature Conditions

As a spacecraft travels further and further from the sun, as would be required if the probe were sent to Jupiter, the solar intensity falls off as $1/\text{distance}^2$. Jupiter is roughly 5 times the distance from the Sun as the earth, and so receives around 25 times less solar radiation. The decreased solar radiation means less photons are being absorbed, and less current is produced. Additionally, the panels radiate most of their heat to the vacuum of space, and experience very low temperatures, as can be seen in Figure 1.5. The low equilibrium temperature of a flat-plate solar array can be calculated from Equation 1.1, which comes from the Stefan-Boltzmann equation. This temperature is dependent on the efficiency of the solar cell (η),

the incoming radiation power (I), the solar absorptivity (α), and the emissivity of the front and back sides of the array (ϵ), with σ being the Stefan-Boltzmann constant [20].

$$T_{eq} = \left[\frac{(\alpha - \eta)I}{(\epsilon_f + \epsilon_b)\sigma} \right]^{\frac{1}{4}}, \tag{1.1}$$

These conditions are usually referred to as Low-Intensity-Low-Temperature (LILT), and photovoltaic performance can be affected by mechanisms that are usually insignificant under standard conditions. Detrimental effects under LILT conditions were reported in 1982 in silicon solar cells, and were attributed to adverse metallurgical interactions between the silicon substrate and the metal contact, resulting in loss of fill factor [21]. Since then, the so-called flat spot has also been observed in III-V multijunction solar cells [22], and appears to be related to the top cell or tunnel junctions. Thus, to manufacture panels for LILT missions, cells are screened under low intensity at room temperature (LIRT) [23]. Unfortunately, it has also been reported that some cells that are rejected using LIRT appear to work well under LILT conditions [24], meaning if no additional screening is performed some LILT suitable cells may be lost. At low temperature, the photo-generated carriers have low thermal energy, and so band alignment is more important at lower temperatures. Specifically, small band offsets that don't significantly affect performance at standard operating conditions may become barriers to current flow at low temperatures, as will be discussed later in Chapters 4 & 5.

These LILT conditions can also be beneficial under certain conditions. The low thermal energy of the carriers results in lower dark current, and in most materials the low temperature causes the crystal lattice to shrink, shifting the band gap to higher energies [25]. For some

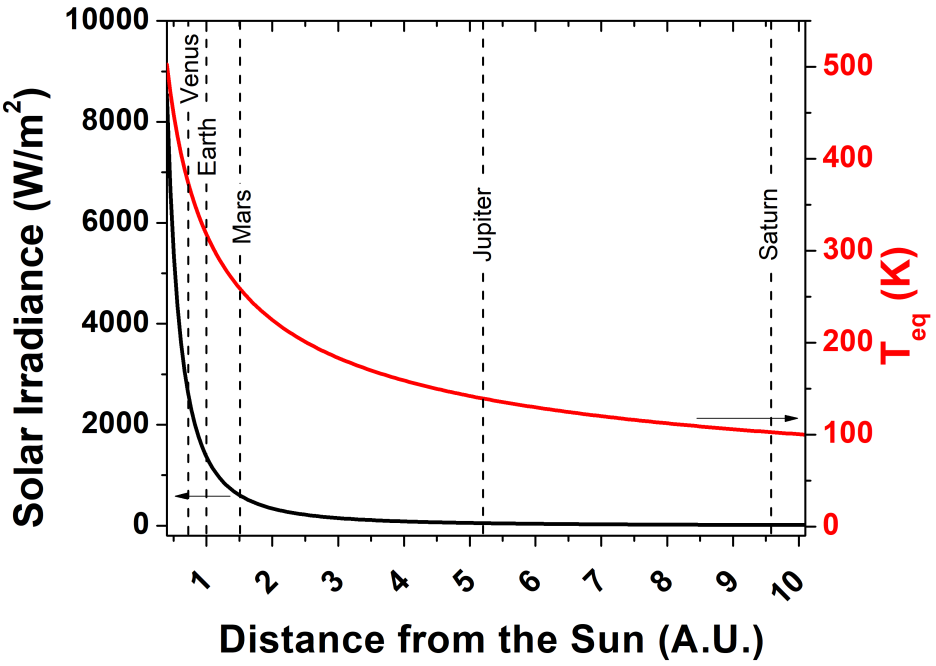

Figure 1.5: Solar intensity and flat-plate equilibrium temperature of a 20 percent solar cell as a function of distance from the Sun. Emissivities of 85% were used for the front and back surfaces of the array.

materials, this band gap increase can result in a better match with the solar spectrum, increasing efficiency. Interestingly, under low temperature, the addition of low intensity conditions can actually also be beneficial in the case of non-optimum band offsets and barriers. If these barriers are mediated by thermionic emission, and have a favorable rate, the small current flow generated by low intensity light can pass the barrier easily, as will be discussed in Chapter 5.

As has been shown, LILT conditions can illuminate defects and barriers that may not be problematic at standard terrestrial operating conditions. In transit to the mission location, probes may also encounter elevated temperatures. These elevated temperatures have the potential to produce irreversible damage to some photovoltaics, particularly some of the thin

film materials [26], [27]. Thus, to determine the temperature range of interest, we take a closer look at the various orbital trajectories used to reach Jupiter and Saturn.

In general, the most basic route between Earth and the outer planets is by using a Hohmann transfer orbit [28]. This type of orbital transfer does have limitations, in that it requires the planets to be aligned in certain ways, and can take a long time. Gravity assists have been used in transfer orbits since 1959 to provide greater flexibility of launch dates and of available launch hardware [29], though gravity assist transfer orbits also require certain planetary alignments. Due to the fuel requirements, transfer orbits using gravity assists have been used on most missions to the outer planets [30].

Various different transfer orbits using Venus, Earth, and Mars have been suggested and used for transit to the outer planets [31]. Complex transfers involving halo orbits have also been studied, which allow for economical transfers without gravity assists [32]. A halo orbit is a complex orbit around certain Lagrange points that exist in a three-body system. For the purposes of the discussion here, we will assume that the minimum orbital distance will be no closer than Venus, which gives us an upper bound on the solar intensity encountered. This solar intensity, along with the parameters listed above, give us around 375 K for the panel temperature from Equation 1.1. In the cases that this intensity and corresponding temperature may be too high, the solar arrays may be rotated at an angle to the sun to absorb less solar radiation [33].

1.3.2 Space Radiation

Damaging energetic particles in space can come from a number of different sources. The solar wind produced by the sun is the main source of radiation encountered in the solar system, and

consists of mainly protons, electrons, and alpha particles (He nuclei) [34]. Similar particles also come from outside the solar system, with extremely high energies, and are generally referred to as cosmic rays.

The direct interaction of these particles with the spacecraft leads to damaging events, which can create defects in semiconductors. These defects can lower the performance of photovoltaic arrays and cause errors in semiconductor processors and memory chips [20], [35]. Thus it is important to use materials which are resistant to radiation damage for the longevity of the spacecraft.

On earth, we experience very little of these damaging particles, due to the protecting influence of the planet's strong magnetic field. This magnetic field deflects the incoming charged particles, and directs them along magnetic field lines to the poles of the earth. The charged particles tend to collect in regions of the magnetic field known as the Van Allen belts, with the size of the belts being proportional to the strength of the planet's magnetic field. While we enjoy the protection provided by the magnetic field, the belts produced also cause increased radiation exposure while spacecraft are travelling through these belts. Of particular concern for satellite networks is the South Atlantic Anomaly, a region of space where the earth's magnetic field is weaker, and allows damaging particles into orbits closer to the earth's surface [36].

A number of the outer planets also have magnetic fields, and so also have planetary radiation belts. Jupiter, in particular, has a magnetic field a few orders of magnitude stronger than Earth's, and consequently has very intense radiation belts [37]. Spacecraft that have visited Jupiter have taken certain orbits in order to minimize time in these extremely dangerous regions [38]. However, future missions that intend to study Jupiter's moons

like Europa may not have that luxury, and so radiation tolerant photovoltaics are under investigation.

Chapter 2

Characterization Techniques and Experimental Setups

In this chapter, the details of the characterization techniques used in this research are explained. Electrical characterization methods are described first, which include current density-voltage (J-V) measurements, external quantum efficiency measurements (EQE), and capacitance-voltage measurements (C-V). The theory and methods for the spectroscopic experiments of photoluminescence spectroscopy (PL) and photoreflectance spectroscopy (EL) are then put forth.

2.1 Electrical Characterization

2.1.1 Current-Voltage Measurements

The relationship between current transport under various bias conditions is a standard measurement for diodes, resistors and optoelectronic devices. Many different parameters such as internal resistances, diode quality, and evidence of barriers can be extracted from this data. This measurement is also quite simple, as it only needs a device which can source a voltage, and sink the current drawn. If the area of the device is known, this measurement also gives the current transported per unit area, and can be compared to devices of different size. This is the measurement most used in photovoltaic research, and is known as the current density-voltage (J-V) measurement.

From the previous chapter, we know that a standard p-n junction diode has a built in potential from the stationary ions present at the interface. As a bias is applied across this

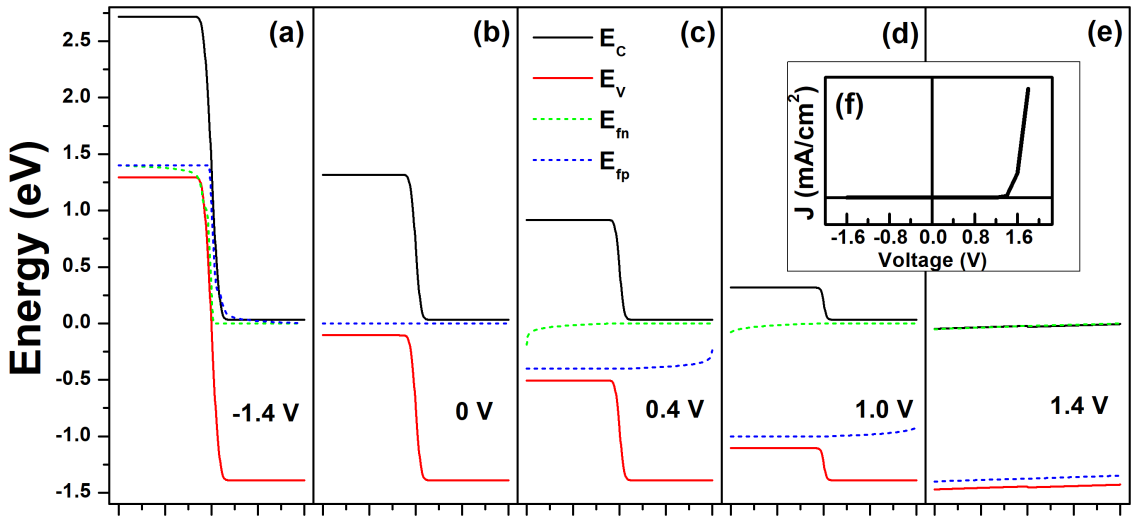

Figure 2.1: Band structure simulation of a simple GaAs p-n junction under different bias conditions. As the bias increases, the built in potential is over come, and the diode then allows current to flow. (a) -1.4 V (b) 0 V (c) 0.4 V (d) 1.0 V (e) 1.4 V (f) J-V curve produced by simulation at these various biases. E_C and E_V are the conduction band and valence band, while E_{fn} and E_{fp} refer to the electron and hole quasi-fermi levels, respectively.

interface, the bias will either work against or with the internal potential. In reverse bias, the internal potential is increased, and the energy bands in the p- and n- regions are shifted more with respect to each other, as shown in Figure 2.1 (a). This shift in the bands means that almost no majority current flows. Current flow in reverse bias is negligible, except for the small amount of thermally generated current known as dark current, and in the case of breakdown at large reverse bias values.

As a forward bias is applied to the junction, the applied bias works against and reduces the internal potential. This reduces the shift in the energy bands, and with enough applied bias, the bands become flat and allow majority current to flow, as seen in Figure 2.1 (c-e).

As the applied bias increases the barrier to majority carriers decreases, allowing current to flow. This behavior is well described by the diode equation

$$J = J_0(e^{\frac{Vq}{nk_BT}} - 1), \tag{2.1}$$

where J_0 is the reverse saturation current, V is the applied bias across the diode, q is the electron charge, k_B is the Boltzmann constant, T is the temperature, and n is the diode ideality factor. An exponential increase in the current flow below turn on, consistent with this equation, is seen in the J-V data, inset (f) of Figure 2.1.

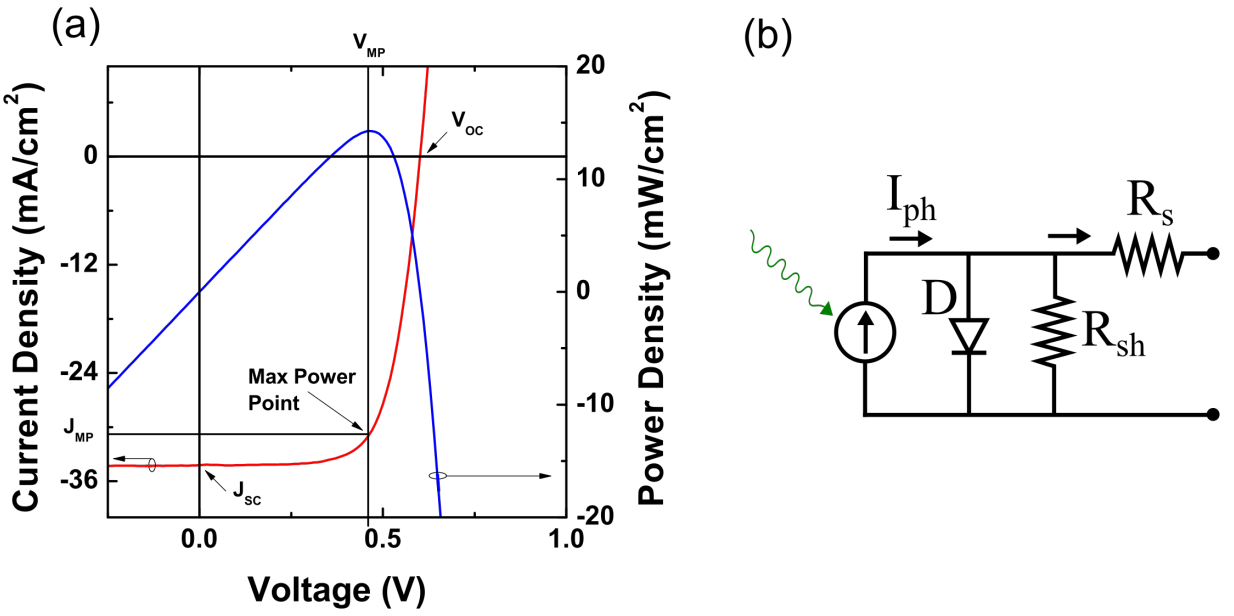

Figure 2.2: (a) An example of current density vs. voltage and power density vs. voltage data from a solar cell, with various features labeled. (b) Example schematic of single diode model of a solar cell with a single diode, shunt and series resistances.

From the previous chapter (1), we know that solar cells are minority carrier devices, and under illumination generate negative current flow. For simple devices, the J-V curve

under illumination is essentially the dark J-V curve shifted downward by the short-circuit photocurrent [39]. Here we outline the J-V characteristic of a solar cell, and put forth the common nomenclature. The point at which the cell is under short-circuit, or where the voltage across the sample is zero, is known at the short-circuit current (J_{sc}). If the cell is in the open-circuit condition, that is the current is set to zero, the voltage produced is known as the open-circuit voltage (V_{oc}). As power is voltage multiplied by current, the cell produces the most power in forward bias, at the so-called maximum power point (P_{max}) with associated max power photovoltage (V_{mp}) and photocurrent (J_{mp}). The fill factor (FF) of the J-V curve refers to the "squareness" of the J-V curve, and is defined in Equation 2.2.

$$Fill\ Factor\ (\%) = \frac{V_{\mathrm{mp}} \cdot J_{\mathrm{mp}}}{V_{\mathrm{oc}} \cdot J_{\mathrm{sc}}} = \frac{P_{\mathrm{max}}}{V_{\mathrm{oc}} \cdot J_{\mathrm{sc}}}, \tag{2.2}$$

Information about the parasitics such as series resistance (R_{s}) and shunt resistance (R_{sh}) can also be qualitatively extracted from the J-V characteristic. The series resistance is usually related to slope of the J-V curve around V_{oc}, while the shunt resistance is usually related to the slope around J_{sc}. Information about the diode ideality factor (n), and quantitative results regarding R_{s} and R_{sh} can be extracted by fitting the J-V data with a simple diode model.

In this work, fitting of the light J-V curve was accomplished by following the methods outlined in [40]. The mathematical equivalent of the circuit shown schematically in Figure 2.2 (b) is outlined in the equation

$$J = J_0 \left(exp\left(\frac{q\,(V - R_{\mathrm{s}}J)}{n k_{\mathrm{B}} T} \right) - 1 \right) + \frac{V - R_{\mathrm{s}}J}{R_{\mathrm{sh}}} - J_{\mathrm{ph}}, \tag{2.3}$$

where R_s, R_{sh}, and n are described above, J_0 is the saturation current density, q is the electron charge, V is the applied voltage, J is the current density, k_B is the Boltzmann constant, T is the temperature, and J_{ph} is the photocurrent density. As the dependent variable J is on both

sides of this equation (an implicit function), it can complicate the curve fitting process. As Zhang *et al.* and others have shown, the Lambert-W function can be used to obtain explicit functions of J and V, which along with some simple assumptions can greatly simplify the fitting procedure.

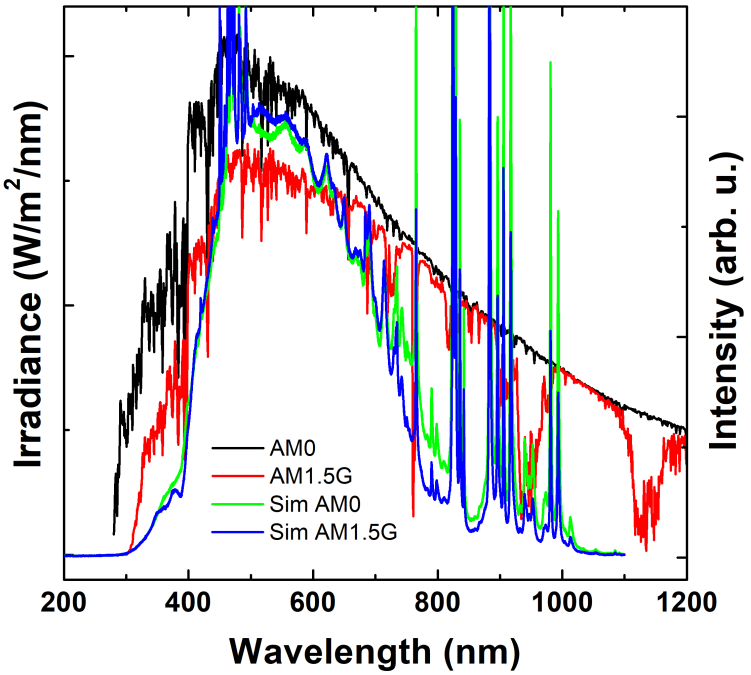

Figure 2.3: A comparison of solar irradiance data from [41] and the 94022A solar simulator viewed with a spectrometer. Note that a number of mirrors were also used to direct the light into the spectrometer, and so this is only a general comparison.

Measurement of J-V is accomplished with a Keithley 2400 Sourcemeter. For the case of solar cells studied in this work, measurements are taken in the dark, under illumination from a Newport Oriel Sol2A 94022A solar simulator, or under monochromatic illumination for certain measurements. The solar simulator was modified slightly to improve dark performance of the shutter, and a dark box was added around the bottom of the simulator to allow for

Table 2.1: Approximate conditions used in Chapters 5 and 6 for LILT experiments. Parameters are taken from [20], [22], [45], [46]. Temperatures are the equilibrium flat plate temperature of a solar array, as described in Chapter 1.

Locations	I (AM0 Suns)	I (W/m^2)	T_{eq} (K)
Mars	0.431	586.2	263
Jupiter	0.037	50.26	135
Saturn	0.011	14.82	100

less-leaky dark measurements. For the light measurements, a filter (either for AM1.5G or AM0) is used to adjust the xenon lamp spectra so that it is closer to the solar spectrum. This solar simulator produces a class A spectral match (IEC 60904-9 2007) to the AM0 spectrum from 400-1100 nm. However, the solar simulator is still only an approximation, as the calibration is based on photon flux in wavelength bins, and so this approximation should be taken into account. For more precise measurements, particularly for multijunction solar cells, solar simulators with multiple sources are used [22]. In order to certify space cells, high altitude balloon flights, high altitude jet flights, or space flight time is used to characterize the cells under the real AM0 spectrum [42]–[44].

For the Low-Intensity-Low-Temperature (LILT) measurements studied in chapters 4 & 5, a set of mesh filters along with adjustments on the simulator were used to adjust the intensity to the appropriate value [22]. In this way, the shape of the spectrum is preserved as the intensity is changed, which may not always be the case with neutral density filters. The LILT conditions representative of orbits around Mars, Jupiter and Saturn are displayed in Table 2.1.

The Keithely 2400 Sourcemeter has the ability to perform 2 wire or 4 wire (Kelvin sensing) measurements. In the case of a 2 wire measurement, the voltage is sourced, and the sourcemeter determines the voltage across the device at the instrument. Accordingly, any resistance in the measurement introduced by the leads and wires going to the sample will not be accounted for. For the 4 probe measurement, two of the lines are sense lines, and should be connected as close to the sample as possible, while the other two lines source the voltage. In this way, the instrument can determine the voltage across the device without the influence of any additional resistances. In the case of small research scale photovoltaic devices, the 4 wire measurement is preferred.

2.1.2 External Quantum Efficiency

External quantum efficiency is a measure of the absorption and collection efficiency of a solar cell, and can be written as

$$EQE\,(\%) = \frac{\text{Photocurrent Collected}/q}{\text{Incident Photon Flux (\# of photons/sec)}/h\nu}, \tag{2.4}$$

where q is the charge of one electron, and $h\nu$ is the energy of one photon. The EQE is calculated from the collected photocurrent (I_{pc}) and reference scans as shown in the following equation:

$$EQE\,(\%) = \frac{I_{\text{pc}} \cdot AC \cdot hc}{\lambda} \cdot \frac{\text{Detector Responsivity}}{\text{Reference Spectrum}}, \tag{2.5}$$

where λ is the wavelength, hc is the Planck constant and the speed of light, and AC is either 1 if the incident light is continuous, or 2.2 if the incident light is chopped. This AC factor is particular to the Oriel/Newport system used here, and reflects the time response of the current pre-amplifier.

In an ideal device, one incident photon should result in the extraction of current from the electron-hole pair generated, and the EQE above the band gap would be 100%. In real devices, reflection, incomplete absorption, and transport mean that the EQE is less than the ideal case, as shown in Figure 2.4. A related measurement called internal quantum efficiency (IQE) measures the current produced from each photon *absorbed*, where the effect of reflection and transmission is subtracted out.

To perform the EQE measurement, light from a quartz-tungsten halogen or xenon lamp is passed through a mechanical chopper, a filter wheel and is dispersed via a monochromator. The selected light is then directed onto the sample via an optical system. The modulation of the light increases sensitivity, allows the EQE measurement to be performed while the room lights are on, and also allows for biasing of the sample with white light or bias, as will be discussed below.

In the J-V measurements described in the previous section, J_{sc} is the amount of current produced per area at short circuit conditions. Since EQE is a measurement of the current extracted, the J_{sc} can also be extracted from short circuit EQE measurements by convolving the solar spectrum with the EQE, and then integrating over the region of interest as in Equation 2.6.

$$J_{sc} = q \int_0^\infty \Phi(\lambda) \cdot EQE(\lambda)\, d\lambda, \tag{2.6}$$

Light bias dependent EQE measurements can also be performed to extract more information about the device. In cases where trap states are normally filled under normal operating intensity, these states may be empty under the small monochromatic light intensity of the EQE measurement, which can affect the measurement. To apply a light bias, the monochromatic light is mechanically chopped, and the bias light (broadband or otherwise)

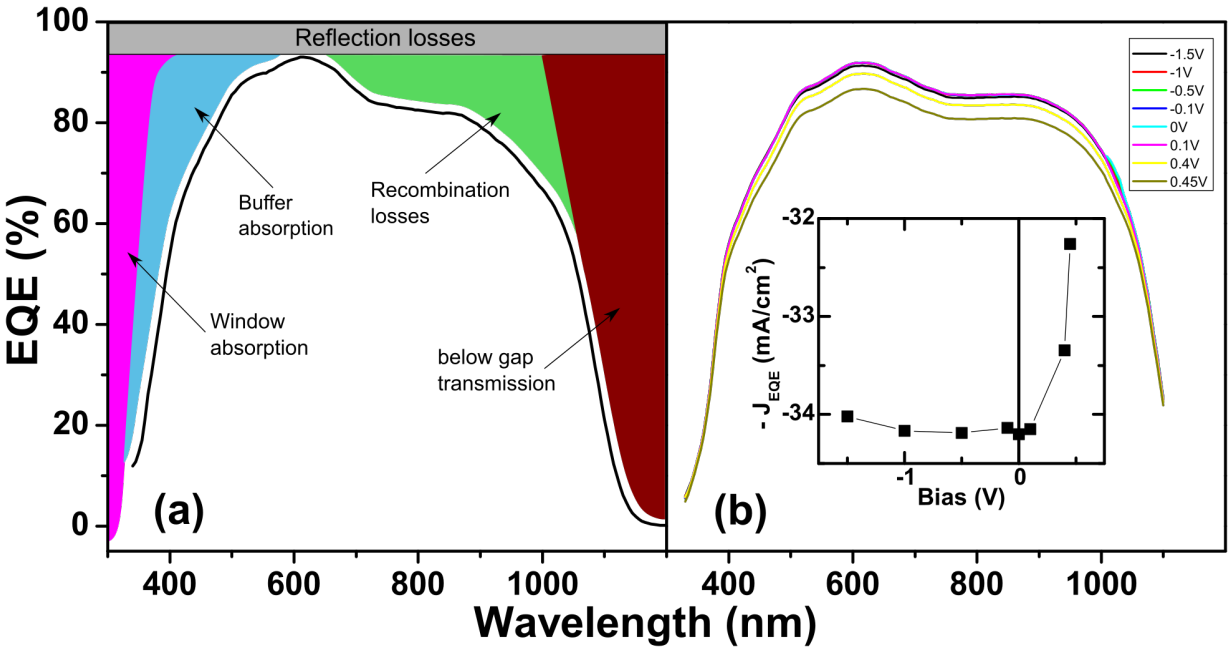

Figure 2.4: (a) Example EQE data showing various loss mechanisms, such as reflection, window and buffer absorption, recombination and transmission. (b) Example Bias dependent EQE data showing a reduction in overall EQE at forward bias. The inset shows the current extracted from the EQE at each bias condition. Panel (a) inspired by [47]

is then directed onto the sample. In this way, practical operation is mimicked and the trap states are filled. The small signal from the monochromatic probe beam is then detected with a current-to-voltage preamplifier and a lock-in amplifier. Care must be taken to adjust the intensity of the light bias so that the traps are filled, but the amplifier electronics are not overloaded.

With the proper electronics, voltage bias dependent measurements can be performed with the same modulated EQE setup. In the case of an applied bias, Equation 2.6 becomes the current extracted at that bias, rather than the J_{sc}. In this way, a J-V curve up to

V_{oc} could be produced from multiple bias dependent EQE data, as is shown in the inset of Figure 2.4 (b). This experimental method is useful in probing operating conditions, as commercial photovoltaic devices do not operate at short circuit current, but at the maximum power point. Thus it is pertinent to measure the EQE at V_{mp}, to determine if there are any significant differences in carrier collection as compared to short circuit conditions.

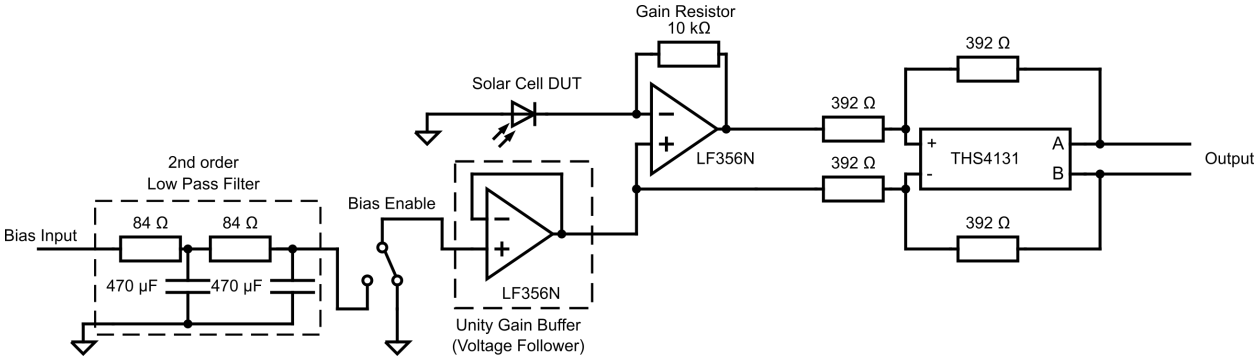

Figure 2.5: Electrical schematic of the preamplifier used to acquire Bias EQE data.

A custom built current pre-amplifier based of off the SR555 by Stanford Research Systems was built in order to perform bias EQE measurements. A THS4131 fully differential low noise amplifier is used to allow a bias to be applied over the device, while still detecting the change in current from the chopped incident light. An appropriate precision resistor is selected for the gain resistor so that the gain is the same as for the reference detector. A Keithley 230 programmable voltage source sets the bias, which passes through a 2^{nd} order low pass filter. This system (constructed by the author) is shown schematically in Figure 2.5.

2.1.3 Capacitance-Voltage Measurements

Capacitance-voltage measurements are a powerful method to extract information about the depletion width of the junction, defect density and the doping profile in the material.

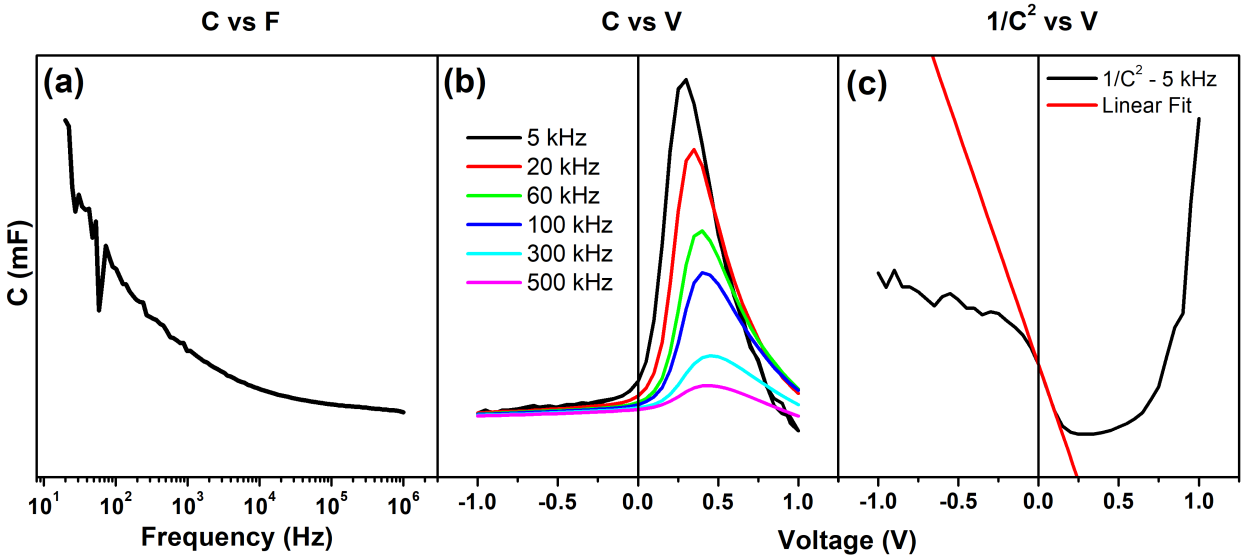

Figure 2.6: Example data of (a) C-F, (b) C-V and (c) $1/C^2$ data with linear fit to slope for built-in potential and doping density extraction.

As discussed in the introduction, a PN junction has a number of stationary charges that introduce a built in capacitance. This configuration can be probed using a small AC signal applied to the sample at a chosen frequency, which modulates the internal capacitance and provides information on the dynamics and non-idealities in the structure. In the LCR unit used in the research presented here, the current through, and the voltage across the sample, are measured. In conjunction with the phase angle between these two values, the capacitance and resistance of the sample can be calculated. An additional DC bias may be applied, around which the AC signal modulates the internal capacitance. This DC bias may be swept through different values, producing the capacitance under different bias conditions.

The frequency of the modulating AC signal must be chosen appropriately so as to account for the response time of defect sites in the sample. If the modulation is too slow, the trap sites will have time to respond (capturing or releasing charge carriers), and can appreciably

change the capacitance. For example, in Figure 2.6 (b), the various traps in the system shown here (GaInNAs) result in a larger capacitance at lower frequencies. In order to find a range of appropriate frequencies, an admittance scan (capacitance vs frequency) is usually taken (see Figure 2.6 (a)), and thereafter a number of capacitance-voltage scans are taken in a region where the frequency response is fairly flat. For the data used in the example here, the trap response time does not produce a flat response until the oscillation frequency is almost 1 Mhz. Some methods also lower the temperature of the sample, and have fast sweep rates to prevent trap response [48].

For an ideal junction with homogeneous doping, the slope of the $1/C^2$ vs V response (2.6 (c)) should be linearly dependent in the reverse bias regime on the bias voltage [49]. The capacitance of the space charge region can be written as

$$C = \sqrt{\frac{qN_{\mathrm{D}}\epsilon_s}{2(V_{\mathrm{bi}} - V - \beta^{-1})}}, \tag{2.7}$$

and rewritten as

$$\frac{1}{C^2} = \frac{2(V_{\mathrm{bi}} - V - \beta^{-1})}{qN_{\mathrm{D}}\epsilon_{\mathrm{s}}}, \tag{2.8}$$

where V_{bi} is the built-in voltage, V is the applied bias, $\beta = q/K_{\mathrm{B}}T$ is a Boltzmann factor, q is the charge of an electron, N_{D} is the doping density, and ϵ_{s} is the static dielectric constant of the semiconductor. The slope of a linear fit to the $1/C^2$ vs V response in 2.6 (c) can then be used to extract the doping density, and the x-intercept is used to extract the built-in potential, as per equation 2.8.

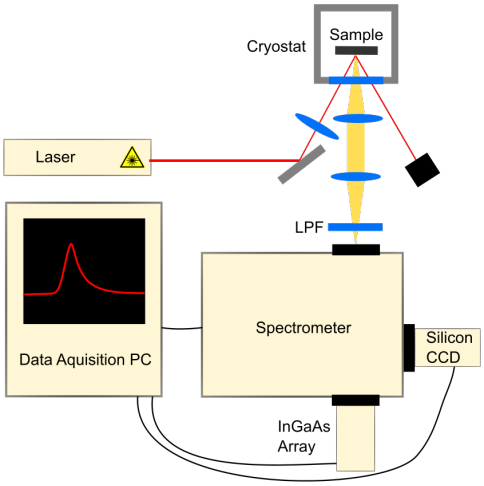

Figure 2.7: Experimental setup for photoluminescence spectroscopy.

2.2 Spectroscopic Characterization

2.2.1 Photoluminescence Spectroscopy

Photoluminescence spectroscopy (PL) is a powerful and simple technique that can extract information about inter and intraband transitions, carrier lifetimes, radiative and nonradiative processes, phonons, and other processes. Typically, monochromatic light from a laser with energy higher than the band gap of the material under test is directed onto the sample, which excites electrons from the valence band to the conduction band. As these electrons relax back down to the valence band, the resulting energy is conserved through the emission of photons. These photons are collected by an optical system and dispersed in a spectrometer. An appropriate longpass filter prevents detection of the direct specular reflection of the laser and the harmonics of higher energy emission. The selected light is then detected by the appropriate detector, as is shown in Figure 2.7.

Different radiative transitions can be observed via photoluminescence spectroscopy, particularly in different temperature regimes. Band to band, excitonic, donor to acceptor, phonon emission, and many other transitions must be accounted for in the spectra [50]. These multiple transitions can prove problematic in photoluminescence analysis, as this method generally probes the lowest energy transitions in the system. When doing analysis of band to band transitions, the feature of interest may be obscured by emission from localized features or other defect states. However, analysis of the physics and information about the system can still be extracted from these lower energy transitions, which stresses the power of the photoluminescence measurement.

As discussed earlier, the band structure of the semiconductor depends on the atomic structure. As the semiconductor heats up, the crystal structure expands, resulting in a shift of the band to band emission as a result of the thermal expansion of the lattice, as shown in Figure 2.8 (c). This temperature dependence can be useful in identifying features, as emission from other features may not change appreciably with temperature.

Spectra obtained from photoluminescence can change depending on the temperature, intensity of the pump, applied bias across the sample, applied magnetic field, and polarization of the incident pump beam. These dependencies are used to identify features, and extract information about the sample. For example, an intensity or power dependent set of measurements might show a peak shifting to higher energies with increasing power. In Figure 2.8 (c), a shift to lower energies with increasing temperature is consistent with the thermal expansion of the crystal lattice and corresponding temperature dependence of the band gap [25].

The different behaviors of features in regard to position and intensity can be fit to equations to quantitatively determine information about the system. One common method of

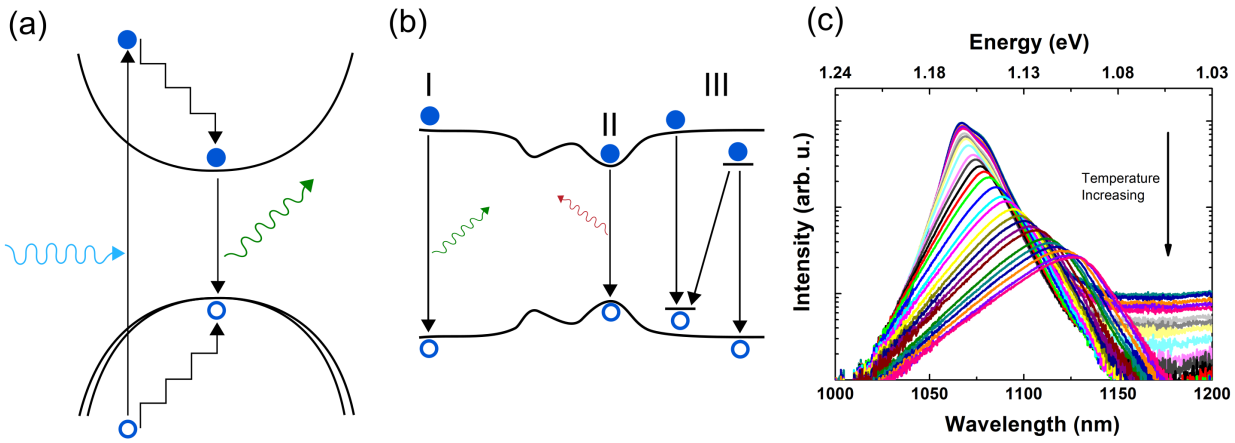

Figure 2.8: (a) Basic absorption and emission of a photon with respect to the gap. (b) Schematic of various PL emission process including (I) band-to-band emission, (II) emission from localized states due to fluctuations in alloy composition, (III) emission from defect to band, band to defect, or other related processes. (c) Example photoluminescence spectra showing a shift to lower energies (higher wavelengths) as temperature is increased.

analysis is to fit the temperature dependent quenching of the integrated PL intensity with a rate equation in an Arrhenius plot [51]. The natural log of the integrated intensity is plotted with respect to the inverse temperature, and is then fitted with an equation of the form

$$I(T) = \frac{I_0}{1 + C_0\, exp(-E_a/k_B T)}, \tag{2.9}$$

where I_0 is the integrated intensity of the PL at 0 K, C_0 is a rate constant, and E_a is the activation energy. Multiple exponential terms can be added to fit quenching behavior where more than one mechanism is responsible.

A second method of investigating the mechanisms behind features is through the integrated intensity dependence as a function of incident power, plotted on a log-log plot. The behavior of the intensity can be fitted to a power law of the form

$$I \propto P^k, \tag{2.10}$$

where k is a fitting parameter. On the log-log plot, the slope of the linear behavior is this k parameter, and is indicative of the recombination mechanism. If $k < 1$, then emission from defect states is suggested, and if $1 < k < 2$, then band-to-band or excitonic behavior is more likely [52], [53].

2.2.2 Photoreflectance Spectroscopy

Reflectivity of a semiconductor is related to the index of refraction and the complex dielectric function of the material. This dielectric function is in turn based on the band structure and intrinsic transitions in the material. Reflectivity and absorption measurements show broad features around the fundamental transitions of the material. Modulation of some parameter related to the system allows the derivative of the optical spectrum to be evaluated. In this case, the modulation of the joint density of states via injected carriers allows the observation of sharp features related to transitions in the material [54].

Various methods can provide this modulation, but in this work we discuss the modulation of the internal electric field induced by photo-injected carriers, using photoreflectance spectroscopy (PR) [55]. A pump source (usually a laser with energy greater than the band gap of the material) is used to excite the sample, creating electron-hole pairs. In the case of a bulk semiconductor, the dangling bonds at the surface of the sample pin the Fermi

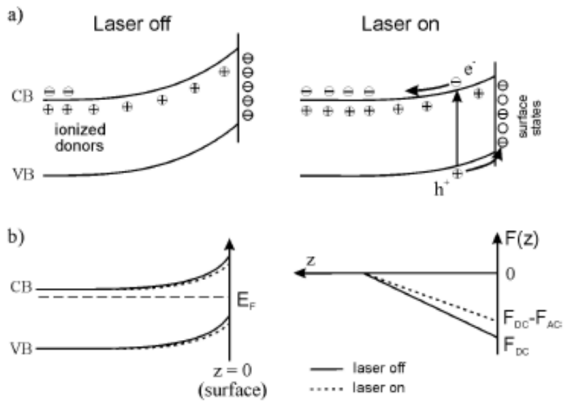

Figure 2.9: (a) Sample schematic of the band structure and the photoreflectance effect. (b) Bands and the built-in electric field for an n-type semiconductor. Reproduced from [*Materials Science Poland*, 2003, Vol. 21, No. 3, Pages 265-266], used under CC BY-NC-ND 3.0 (https://creativecommons.org/licenses/by-nc-nd/3.0/)

level, and this results in a depletion region at the surface, and an internal electric field. The internal electric field sweeps the photogenerated carriers, and the minority carriers travel towards the surface where they passivate the stationary ions, reducing the electric field. In systems where confinement is introduced, like quantum wells, impurities or bound excitons at low temperatures, the electric field cannot accelerate carriers. However, the periodic photogenerated carriers introduced will still affect internal potentials and bending of bands at interfaces in the structure, and modulate the dielectric function by changing the electric field around the quantum well [56]. In these confined cases like a QW, induced modulated electric fields may lead to Stark effects on the subbands and excitonic levels in the QW, rather than the Franz-Keldysh effect [57].

This modulation of the internal electric field, be it at the surface, a junction, or an interface, results in a perturbation of the dielectric function. The relative changes in the reflectivity due to this modulation are measured, and can be described as

$$\frac{\Delta R}{R} = \frac{R_{\text{off}} - R_{\text{on}}}{R_{\text{off}}} = \alpha(\epsilon_1, \epsilon_2)\Delta\epsilon_1 + \beta(\epsilon_1, \epsilon_2)\Delta\epsilon_2 \tag{2.11}$$

where R_{off} and R_{on} represent the reflectance when the pump laser is off and on, respectively [54]. The Seraphin coefficients α and β are related to the complex dielectric function, and are outlined in [58]. $\Delta\epsilon_1$ and $\Delta\epsilon_2$ are functions of the modulating electric field, and emerge from the application of the Kramers-Kronig dispersion relation. An alternative expression in terms of the real part of the index of refraction n and the extinction coefficient k is found in [50].

Photoreflectance spectra exhibit different line shapes based on the relative strengths of the internal electric field (referred to as the electro-optic energy - $\hbar\Omega$ - essentially the energy gained from acceleration by the field) and the lifetime broadening parameter (Γ). This electro-optic energy is defined as

$$(\hbar\Omega)^3 = \frac{q^2\hbar^2E^2}{2\mu} \tag{2.12}$$

where q is the charge of an electron, $\hbar$ is the reduced Planck constant, E is the electric field, and μ is the interband reduced mass evaluated in the direction of the field [59]. In the low-field regime where $\hbar\Omega \leq \Gamma$, the photoreflectance can exhibit either third-derivative or first derivative line shapes. Bulk semiconductors display these third-derivative like features, while systems that have bound states like quantum wells or excitons display first-derivative like shapes because of the absence of translational symmetry [54]. The intermediate field regime exists when $\hbar\Omega \geq \Gamma$, but qEa_0 is much less than the band gap energy, where q and E are the same as above, and a_0 is the lattice constant of the material. In this regime,

Franz-Keldysh oscillations (FKO) occur, where the period of the oscillations depend on the dominant field in the structure. The high field regime is when qEa_0 is comparable to the band gap, and in this regime the electromodulation produces stark shifts [60].

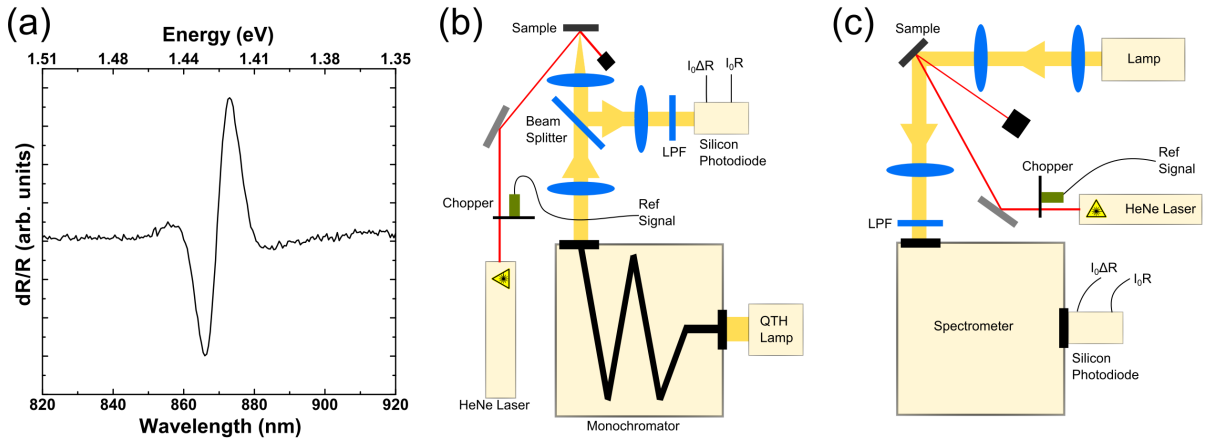

Figure 2.10: (a) Example PR spectra of GaAs at room temperature, acquired during testing of this system. Experimental setups for photoreflectance spectroscopy in the (a) dark configuration and (b) bright configuration.

An example of a basic photoreflectance spectra is shown in Figure 2.10, where the main feature in GaAs at 300 K can be observed. This sharp feature is representative of the third derivative type features typical of bulk transitions in photoreflectance spectra. The slight initial rise at $\sim$ 855 nm may be signs of weak Franz-Keldysh oscillations in this material, probably washed out by the temperature and relatively weak incident pump beam used.

For photoreflectance spectroscopy, there are several derivative setups that can be used. All configurations implement a monochromatic pump beam which is modulated, and is the source of the modulated electric field in the sample. In our case, the laser is modulated by a mechanical chopper, and the reference signal is sent to the reference input of a lock-in

amplifier. The signal from the detector is sent to the input of the Stanford Research System SR830 lock-in amplifier which detects the in-phase component of the modulated signal. The constant (DC signal) is sent from the detector and recorded on a digital multimeter.

The first setup is shown in Figure 2.10 (b), and is labeled here as the dark configuration. Light from a quartz-tungsten halogen lamp is dispersed with a monochromator, which is then reflected off of the sample into a detector. The monochromator allows the wavelength to be scanned over the area of interest. A longpass filter prevents the majority of the scattered laser light from being detected.

In the bright configuration, shown in Figure 2.10 (c), broadband white light from a lamp is reflected off of a sample, and is directed through a longpass filter and into a spectrometer. The spectrometer grating disperses the light, which is sent into a detector.

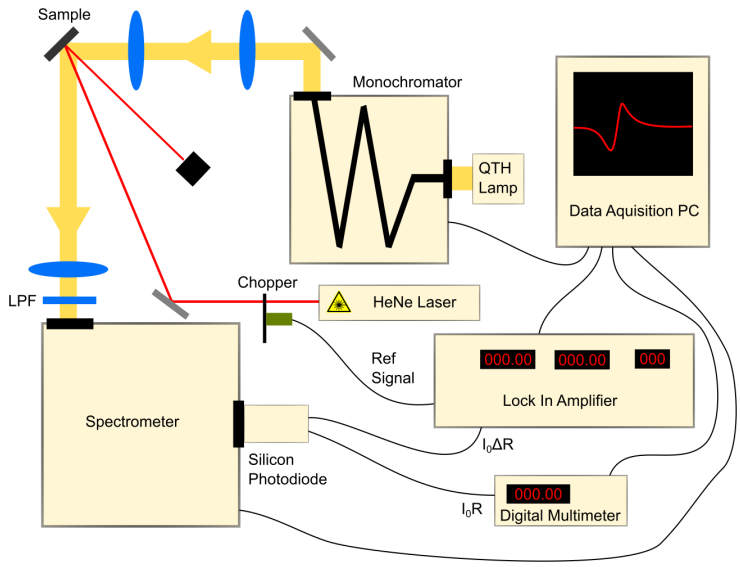

Figure 2.11: Experimental setup for photoreflectance spectroscopy in the dual spectrometer configuration.

In the dual configuration, shown in Figure 2.11, a lamp and monochromator is used to produce the probe beam, and a spectrometer collects and disperses the reflected light into a detector. This configuration provides even more rejection of stray laser light than the dark configuration, and the lower overall intensity of the probe beam can help limit shifts in signal associated with the photovoltage effect [61].

When working with samples that have bright photoluminescence even at room temperature, such as quantum well or quantum dot based samples, it is important to collimate the incoming probe beam on to the sample, and to use long focal length optics so the collection lens can be placed as far from the sample as possible. This, as well as adjusting the power of the pump beam, will limit the collection of any unwanted photoluminescence signal.

Experimental Results and Analysis

Chapter 3

Hydrogenation in GaInNAs Solar Cells

3.1 Introduction to GaInNAs

3.1.1 Multijunction Solar Cells

An established method to sidestep the fundamental limits of single band gap solar cells is the so called multi-junction solar cell. Though expensive to produce, these devices have found use in concentrator solar power systems, and in space applications where power per unit mass can justify higher costs. The traditional three junction (3J) cell based on GaAs has been widely successful in the space market, and efforts have long been underway to improve the performance by adding additional junctions [62].

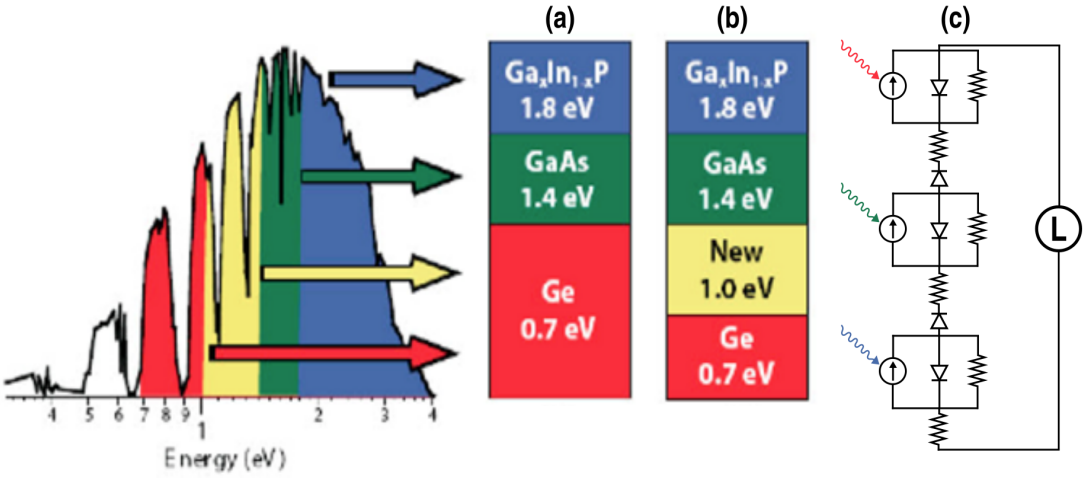

Figure 3.1: (a,b) Addition of a GaInNAs 3rd junction to produce a 4J multijunction solar cell. (c) Example electrical schematic of a epitaxially grown multijunction solar cell. Parts (a) and (b) inspired by Ref. [63]

Monolithic multijunction solar cells are interconnected by tunnel junctions; high band gap (optically transparent) and electrically conductive interfaces that allow the different junctions to be connected in series [64]. Each junction acts as a diode, and these diodes are connected in series as illustrated in the schematic shown in Figure 3.1 (c). Thus, the total current extracted from the device is limited by the smallest current producing junction. Consequently, the choice of materials for, and the thickness of, each junction is critical to enable the highest efficiency. A schematic of a traditional 3J solar cell using GaInP, GaAs and Ge junctions is shown in Figure 3.1 (a). In the 3J device, the Ge junction produces about 50% more current compared to the upper junctions, which is therefore wasted. Splitting the Ge junction into two sub cells is one method to solve this issue [65], [66]. However, pursuit of this method beyond calculations appears limited by the lack of a high quality tunnel junction in these materials.

Epitaxially grown solar cells are restricted by the lattice constant of the materials used. If a crystal is grown on top of a material that has a significantly different lattice constant, then defects result from the inevitable relaxation of stress and/or strain introduced into the crystal by the mismatch. These defects will then propagate up in the growth direction, and negatively affect all subsequently grown layers. Some solar cell production methods, such as inverted metamorphic multijunctions (IMM), try to address this issue by growing an inverted solar cell structure, and graded buffer layers [9]. In this way, the inevitable defects are confined to the mismatched final grown junction, and don't affect the upper junctions. This method has gained some traction, and commercial devices based on this technology are now coming to market [67]. However, the additional growth and fabrication necessary

does increase the cost above other III-V multijunction solar cells, bringing economics into the balance.

3.1.2 GaInNAs: Potential and Problems

In order to develop upon a conventionally grown epitaxial multijunction solar cell based on GaAs, a material with the proper lattice constant and band gap is needed. The introduction of small amounts of N into InGaAs has the effect of decreasing the band gap of this material, due to introduction of isoelectronic states that are close to, and resonant with the conduction band minima, as described in the so called band anticrossing model [68]. This remarkable effect occurs due to the interaction and resulting repulsion between conduction band states and localized states that result from N_{As} isoelectronic impurities. This quaternary (GaInNAs) can be grown lattice matched to GaAs with a gap of 1 eV, and thus has been suggested for use in four junction solar cells for a number of years [69], [70]. However, short minority carrier diffusion lengths typically seen in these materials have thus far prevented their widespread usage in high-efficiency photovoltaic devices [71]. Some success has been observed when using Sb as a surfactant (and inevitably a constituent) during growth, which resulted in a world record device with a PCE of 44% from Solar Junction [72]–[76].

The issue with this material is derived from the need to use low temperature growth conditions for the prevention of phase separation, yet high temperatures are better for incorporation of nitrogen [77]. This results in relatively poor material quality upon the introduction of nitrogen, as a result of unavoidable gallium vacancies, cluster defects such as Ga-N_4 and Ga-In-N_3, and other non-idealities. These defects provide recombination centers that reduce solar cell performance [63], [78], [79].

An increase in material quality and passivation of defects has been observed when rapid thermal annealing (RTA) the dilute nitride material in a nitrogen-rich environment. This annealing appears to facilitate increased N-As substitution, promotes the reordering of the nearest neighbor environment from Ga-N to In-N, and reduces the density of interstitials and vacancies [78], [80]–[83]. Time resolved experiments give a PL decay time with nearly a 100% increase upon annealing, corresponding to a large reduction in number of nonradiative defect centers [84]. Despite this large improvement with RTA, alloy fluctuations and larger nitrogen clusters remain [79], [85]–[87]. Additionally, the substitution of As with N results in distinct local electrical properties due to the high electronegativity and small size of nitrogen [49]. Annealing from high intensity laser radiation should be mentioned, as it has been observed in GaAsN and to some degree in GaInNAs, though this effect is not expected here as no irreversible change in the PL is observed with excitation power [88].

Single nitrogen centers, or isoelectronic impurities, are inherent to this system, and thus are present in even the highest quality material. In dilute GaAsN and GaInNAs, larger clusters and nearest neighbor nitrogen pairs exhibit states below the gap, while single nitrogen center levels have been observed in the conduction band continuum [89]–[92]. As mentioned above, the introduction of these nitrogen based isoelectronic states also results in the uncharacteristic lowering of the band gap.

Alloy fluctuations as a result of indium segregation have also been observed in GaInNAs [81], [82], [94]. Indium rich regions (lower band gap) in the material can act as quantum dots that will localize photogenerated carriers at low temperature [81], [94], increasing radiative recombination, and decreasing carrier lifetime and diffusion length at higher temperatures [85]. The behavior of these alloy fluctuations combined with deeper levels related to nitrogen

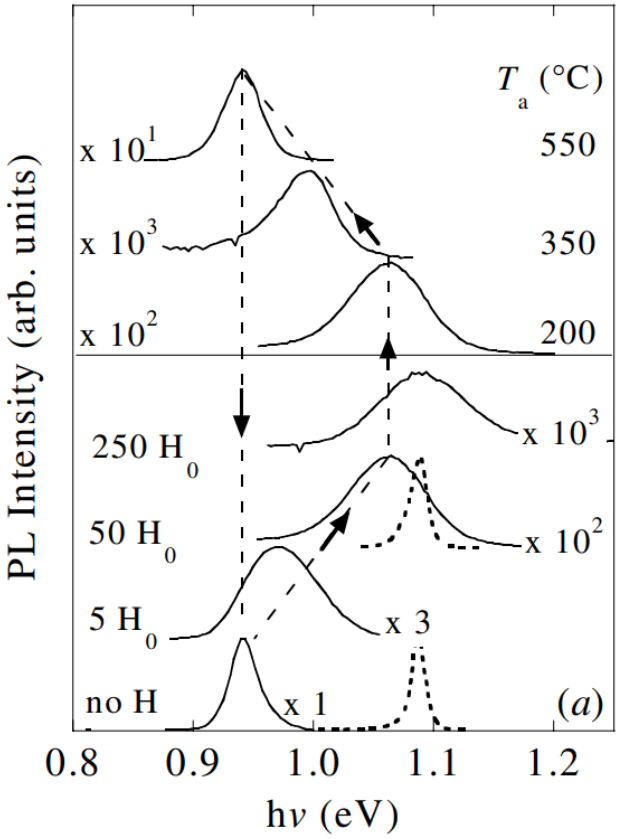

Figure 3.2: Hydrogenation and Annealing effects on PL of GaInNAs. Reproduced with permission from Ref. [93]

clusters serve to potentially increase efficiency of optical emitters, while impeding carrier collection in photovoltaic and detector applications. Studies on GaInNAs based solar cells have reported relatively poor quantum efficiencies as a result of this inhibited carrier collection and lifetime [63], [71], [85], [95].

Hydrogenation has been studied as a defect passivation method in various materials, including GaInNAs [93], [96], [97]. However, previous results in this material showed that high levels of hydrogenation removed the effect of the substitutional nitrogen [93], and also stabilized gallium vacancies [96], [97]. As the samples are hydrogenated, the PL emission

shows a blue shift to the band gap of the nitrogen free alloy, shown in Figure 3.2 [93]. Thus, the lowering of the band gap induced with the introduction of nitrogen is effectively removed with the formation of strong N-H complexes upon hydrogenation [91].

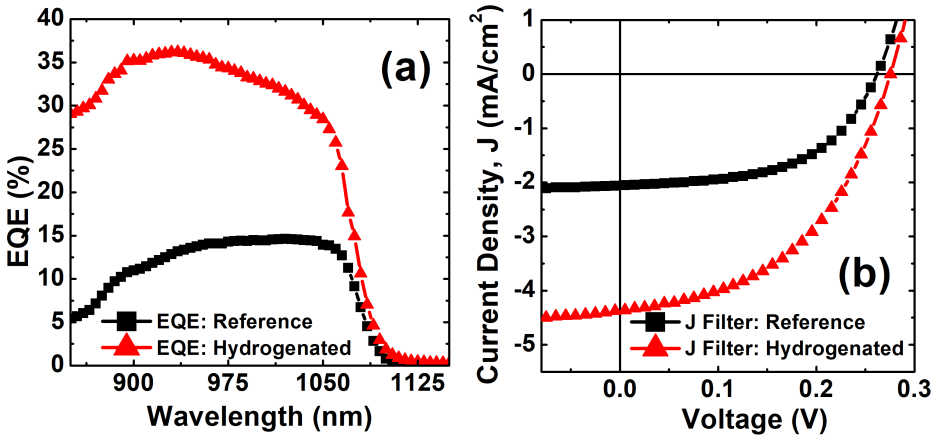

Figure 3.3: Effects of hydrogenation on the (a) EQE and (b) J-V characteristics of a GaInNAs solar cell. Reproduced with permission from Ref. [92]

Hydrogen has also been observed to affect the doping in this system, where intrinsically grown samples are usually slightly p-type due to the presence of gallium vacancies. When excess hydrogen is used in the MOCVD growth of samples, this background doping is seen to change to n-type [98]. This p- to n-type shift is correlated to stable N-H complexes that act as donors in GaInNAs and GaAsN, whereas in other III-V materials, hydrogen does not preferentially form donors or acceptors, specifically [93], [95]. The complete removal of the effects of the nitrogen-related impurities and defects upon hydrogenation is unique to the dilute nitride systems, as is the reversibility of this process when samples are subjected to high temperatures [79].

Hydrogenation of the dilute nitrides and the associated effects have been reported extensively in the literature [93], [99]. The removal of the characteristic 's-shape' in the temperature dependent PL energy is relatively new [92], [96], [100], and here, the demonstrated control of shallow localization centers is unique. In previous studies by our group, both deep defects and localization centers were observed to be passivated by careful control of the hydrogenation process, which is unique as these localization effects are observed in even the best dilute nitride material. Though the initial material quality was rather low, an almost three fold improvement in the EQE and corresponding increase in J_{sc} was observed upon hydrogenation (see Figure 3.3).

3.2 Optical Study of the role of N-H centers in UV-hydrogenated GaInNAs

To better understand the effect and mechanism behind hydrogenation in these solar cells and the control of radiative centers, a study of optical samples via power and temperature dependent PL measurements was undertaken. Additional theoretical support was provided by complementary DFT calculations to help determine the most likely role of hydrogen in the GaInNAs material.

This chapter is partially based on results described in Brown et al.'s paper published in *RSC Advances*, vol. 7, no. 41, pp. 25353-25361, 2017.

3.2.1 Experimental Details

The optical samples studied here were grown on a GaAs substrate by molecular beam epitaxy (MBE) at CNRS-CRHEA in France. A 550 nm-thick GaAs buffer was grown on the substrate at 580 °C, followed by a 1 µm-thick $Ga_{0.91}In_{0.1}N_{0.03}As_{0.97}$ layer grown at 420 °C, and finally capped by a 75 nm GaAs layer (see Figure 3.4 (a)). The composition of the dilute nitride layer was determined by a calibration epilayer, and nitrogen radicals for introduction of nitrogen were generated from a RF plasma source (ADDON) using high purity nitrogen gas (6N5). Post-growth annealing of these samples was performed at 800 °C for 30 seconds in a forming gas (high-nitrogen) atmosphere. RTA studies of similar samples were performed previously to determine the temperature that maximized the PL signal [101]. After annealing, one sample was kept as the reference, while the other two samples were hydrogenated using a UV-activated process [102] at two different concentrations, an "intermediate" level of 0.5 × 10^{15} atoms/cm^2 and the "highest" level explored here of 1.1 × 10^{15} atoms/cm^2, respectively.

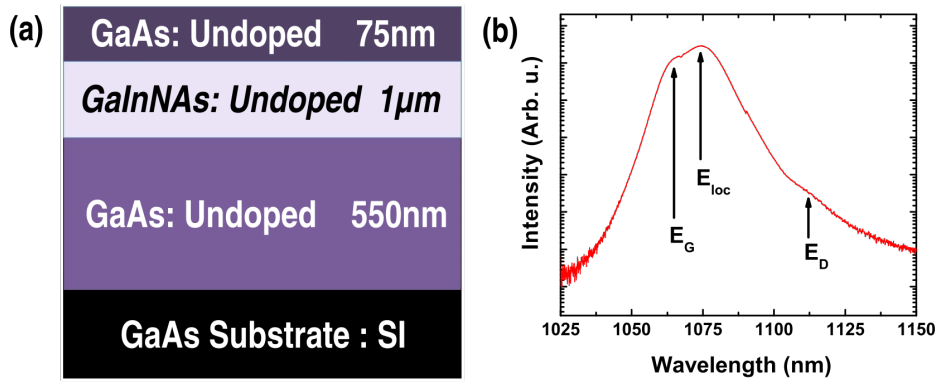

Figure 3.4: (a) Schematic of optical samples studied here. (b) Example PL spectra of the reference sample taken at 4.2 K, with relevant features labeled.

The UV-activated process used here employs high energy photons to dissociate molecular hydrogen on the surface of the material, where atomic hydrogen can then diffuse into the sample. The energy of these photons is great enough to break apart molecular hydrogen, but not enough to ionize, thus neutral hydrogen is produced at the surface. As the energetic photons must be present at the surface of the material, only the illuminated areas are hydrogenated, which can be used to selectively treat samples. Unlike hydrogenation processes using plasma, this procedure can be accomplished in a wide range of pressures (10^{-6} Torr to 10^{5} Torr) and relatively low temperatures. Ion beam analysis of test samples indicated hydrogen at a depth of $\sim$2 µm, indicating penetration completely through the nitride layer, though some excitation energy dependent (and thus depth dependent) PL appear to indicate grading of the hydrogen concentration with depth. The conditions used for the optical samples studied here were an excitation wavelength <325 nm, pressure of 42 Torr, exposure time of 4 hours, and a temperature of 330 °C and 382 °C, for the intermediate and highest concentrations, respectively.

Experimental details and setups for the relevant experiments shown here can be found in Chapter 2.

3.2.2 Experimental Results and Discussion

3.2.2.1 Temperature Dependence

The PL spectra of the reference sample at 4.2 K is shown in Figure 3.4 (b) on a log scale, where there are three features labeled. The dominant feature (E_{loc}) at low temperature is attributed to carriers localized at lower energy states, while the lower intensity and higher energy feature (E_G) is associated with the fundamental band gap transition of the material. The lower

energy feature that appears as a shoulder (E_D) is tentatively attributed to larger nitrogen clusters, and is further discussed later. Though these samples were grown to be intrinsic, thermopower measurements qualitatively suggest these are slightly p-type, as expected in such systems, where the low growth temperatures required to incorporate nitrogen result in the formation of gallium vacancies.

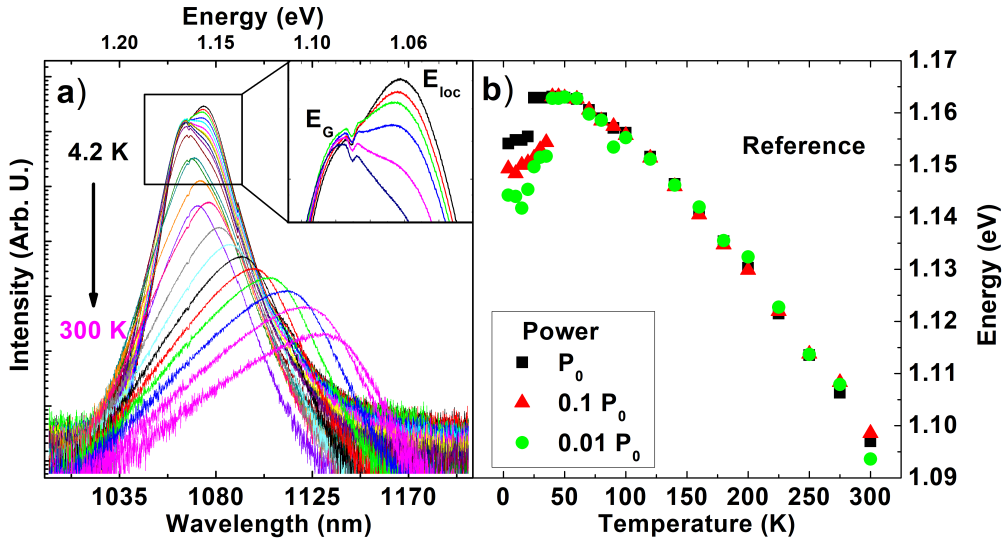

Figure 3.5: (a) Temperature dependent PL spectra for the reference sample. (b) Peak energy position of the PL as a function of temperature for three different powers, for the reference sample. P_0 corresponds to 13 kW/cm^2.

Temperature dependent PL spectra for the reference and the highest hydrogenated samples are shown in Figure 3.5 and Figure 3.6, respectively. As discussed above, both samples have overlapping features attributed to localized states (E_{loc}) and the fundamental gap transition (E_G). For the reference sample (Figure 3.5), the E_{loc} transition dominates the PL at low temperatures, and above 40 K contribution from this feature is reduced and the band gap E_G becomes the main peak. This transition from the lower states can be the result of carriers

with increased thermal energy, which with increasing temperature redistribute to higher energy states. This shift can be clearly seen in the inset to Figure 3.5 (a), where a magnified image of the low temperature peaks is shown.

This shift from low to higher energy states with increasing temperature is also illustrated when plotting the energy of the dominant peak versus temperature, as shown for the reference in Figure 3.5 (b). This 's-shape' temperature dependence is typical of these dilute nitride systems, and is indicative of the transition from PL dominated by emission from localized states to free carrier emission [103]. Again, this transition between these states is due to increasing thermal energy, which allows photogenerated carriers trapped in local potential minima to redistribute to higher energy states. In the reference sample, the onset of this thermal redistribution begins at temperatures above 25 K, and localization behavior occurs below 40 K.

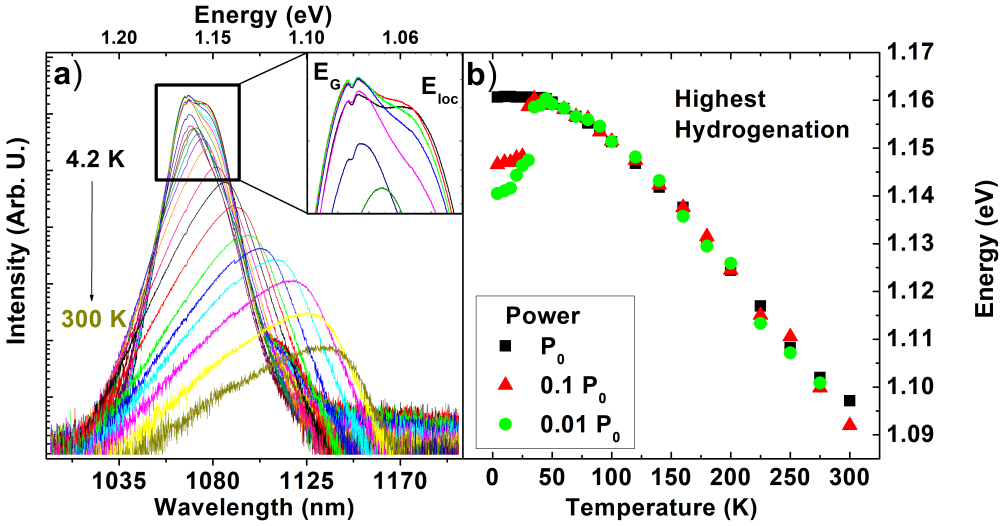

Figure 3.6: (a) Temperature dependent PL spectra highest hydrogenated sample. (b) Peak energy position of the PL as a function of temperature for three different powers, for the highest hydrogenated sample. P_0 corresponds to 13 kW/cm^2.

Increasing incident power also affects this redistribution of carriers, as can be seen in Figure 3.5 (b) for the different powers. The lowest power (green circles - 0.01 P_0) shows a localization potential of ∼20 meV, where the photo excited carriers are quickly localized by centers at temperatures below 25 K. As the power is increased to the intermediate (0.1 P_0) and highest power levels (P_0 - 13 kW/cm^2), a blueshift in the minimum of the 's-shape' is observed. Additionally, the temperature minimum shifts to a lower temperature upon increased power. Both of these behaviors are reflective of increased occupation of localized states as a result of the increased carrier excitation [52], [104], [105]. With an increase in temperature, evidence of carrier redistribution to the higher energy states of the band gap is observed, and above 40 K all powers exhibit traditional energy dependence of the band gap with temperature as outlined by Varshni [25].

Temperature dependent PL spectra for the highest hydrogenated sample is shown in Figure 3.6 (a), along with the associated peak energy versus temperature for three different powers in (b). Similar to the reference sample, at low temperatures features associated with carrier localization (E_{loc}) and the main band-to-band transition (E_G) are observed, though in this case, E_G is now the most intense feature even at the lowest temperature. The intensity of the band gap feature can clearly be seen in the inset of Figure 3.6 (a). This PL spectra was taken at full power (13 kW/cm^2), and as power is decreased, a recovery of the 's-shape' can be observed at low power and temperature, indicating that complete passivation of the defects responsible for localization was not achieved with the current hydrogen dosage (10^{15} H/cm^2).

3.2.2.2 Intensity Dependence

To better understand the various features in the PL, spectra were acquired at 4.2 K as a function of incident excitation power, which is displayed in Figure 3.7 and Figure 3.8 for the reference and the highest hydrogenation sample, respectively. The PL spectra was fit with a number of Gaussian peaks, one for each feature, to deconvolve the complicated nature of the emission. The energy and intensity of these fitted Gaussians was tracked as a function of excitation power, and are plotted in the side panels of each figure. As described in Chapter 2, the power dependent intensity of each feature can be fit to a power function, where the fitting parameter k is indicative of the recombination mechanism, either defect related recombination ($k < 1$) or excitonic related recombination ($1 < k < 2$) [52], [53].

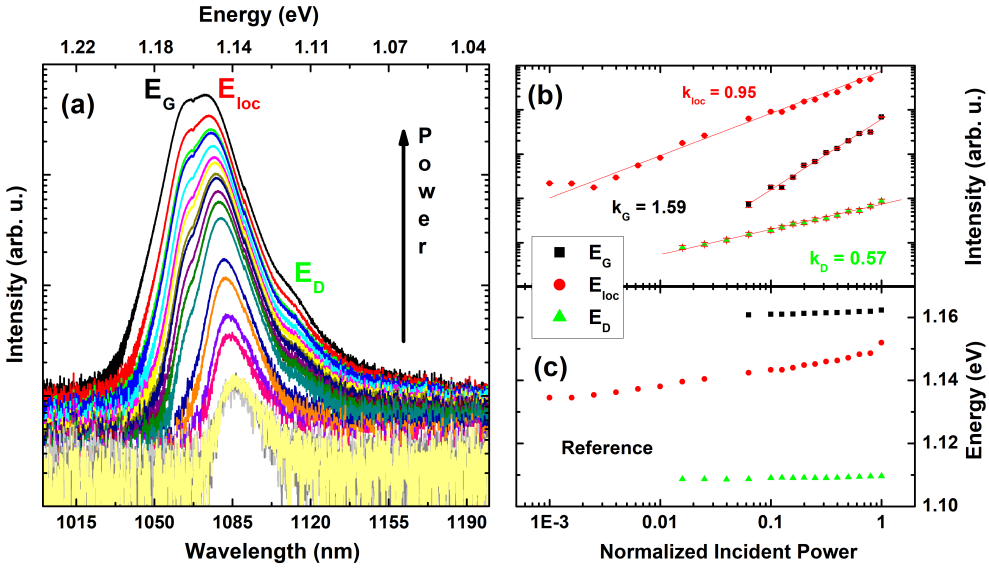

Figure 3.7: (a) Power dependent PL spectra acquired at 4.2 K for the reference sample. (b) Integrated intensity as a function of power of Gaussians fitted to the labeled features, plotted on a log-log plot. (c) Peak energy position of the fitted Gaussians plotted versus normalized incident power.

For the reference sample, an increase in the contribution of the band gap feature (E_G) can be observed with increasing power, likely due to filling of the limited number of localized states in the sample area probed. This increase in the E_G peak with power may also reflect a difference in the carrier capture cross sections of the two main radiative processes (E_G and E_{loc}). As was observed in the temperature dependent PL, in the reference sample the feature associated with carrier localization remains the most dominant peak at low temperature for all powers tested. Fitting of the integrated intensity of each feature versus power on the log-log plot in Figure 3.7 (b) gives $k_G = 1.59$ and $k_{loc} = 0.95$, both of which are consistent with the fundamental band-to-band transition and an excitonic transition, respectively.

The peak position of each feature is tracked, converted from wavelength to energy, and is plotted in Figure 3.7 (c), where all features show some increase in the energy with power. Here, this blueshift in energy, even for the E_{loc} feature, is most likely due to a combination of state filling effects, local heating, and/or spatial separation of carriers from localization centers [92], [100]. In the temperature dependent PL discussion, a change in the 's-shape' dependence with increasing excitation power is observed, and attributed to increased occupation of states (state filling) from localized centers. These carrier localization centers, and the mechanism behind their formation, will be discussed later, though their role in spatially separating photogenerated carriers is well known in this system [100] and has been seen to impact solar cell performance [85]. Blueshifting of peak energy with power can also occur in systems with Type-II interfaces, though since GaInNAs is a type-I system, this mechanism is unlikely here [106], [107], and is rather due to spatial separation of carriers in local potential minima [104].

For the highest hydrogenated sample, the PL spectra is dominated by the fundamental band gap E_G at the highest powers, though this behavior is intensity dependent, as was

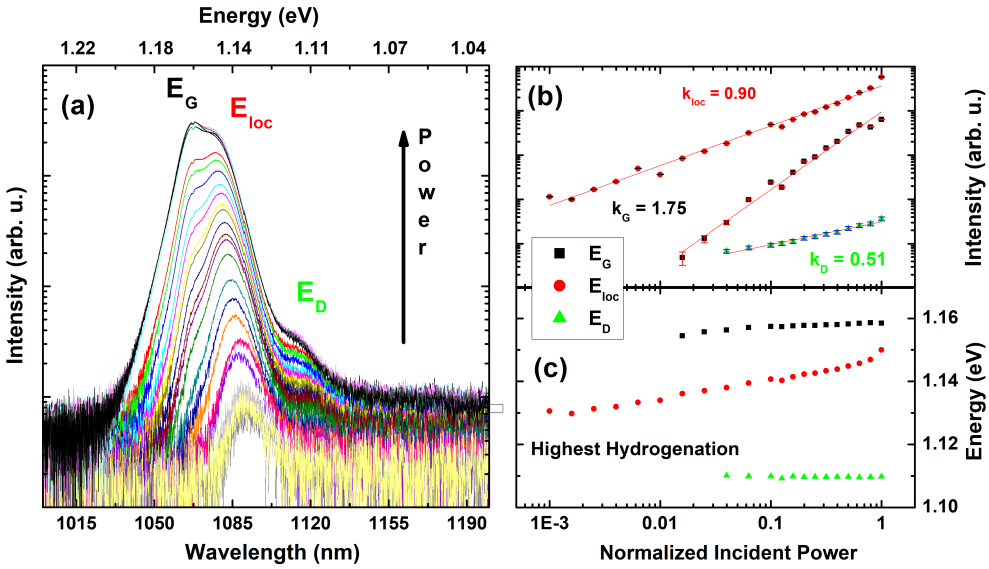

Figure 3.8: (a) Power dependent PL spectra acquired at 4.2 K for the highest hydrogenated sample. (b) Integrated intensity as a function of power of Gaussians fitted to the labeled features, plotted on a log-log plot. (c) Peak energy position of the fitted Gaussians plotted versus normalized incident power.

observed in the temperature dependent measurements. At lower excitation powers and temperatures, where the occupation of the lower energy localized centers is not saturated, emission from these localized states (E_{loc}) is the main feature in the PL. Fitting of the integrated intensity data in Figure 3.8 (b) shows similar values of $k_G = 1.75$ and $k_{loc} = 0.90$ as compared to the reference sample, lending further evidence to the origin of these features.

A lower energy feature around 1120 nm, labeled E_D, is apparent in both the reference and hydrogenated PL spectra taken at 4.2 K. This feature appears relatively unaffected by temperature. Fitting of the integrated intensity power dependence for this feature gives $k_D = 0.57$ for the reference and $k_D = 0.51$ or the hydrogenated sample, which confirm the defect related nature of this feature. Though more evidence is needed to determine the exact

mechanism behind this feature, larger nitrogen cluster defects may be responsible [94], [108], [109]. Several groups working in these systems have reported deep donor and/or acceptor states correlated with these nitrogen clusters.

These nitrogen cluster defects would result in states at energies similar to their binding energy, which at higher temperatures results in mid-gap states, contributing to non-radiative recombination [83]. Unlike reported hydrogenation effects on most defect centers, here E_D does not appear to appreciably change with hydrogenation. Earlier results in these systems have showed selective passivation of lower energy states correlated with larger nitrogen clusters [99].

Upon hydrogenation, E_D becomes more resolved, though this apparent increase may actually be due to the reduction of the E_{loc} peak. As shown in Figure 3.7 (c) and Figure 3.8 (c), almost no change in the peak energy position of E_D is observed with increasing excitation power, which is similar to the power dependence of the band gap E_G. This correlation suggests that this defect is related to the bulk GaInNAs material, perhaps connected to strain or interfaces deeper in the sample. As mentioned previously, though ion beam measurements indicated hydrogen to a depth of 2 µm, initial excitation energy dependent PL measurements suggest a non-uniform depth profile of the hydrogen concentration. As this concentration appears to decrease with increasing depth into the sample, defect centers which appear robust to hydrogenation may in fact be deeper in the sample. Increasing defect concentration towards the bottom of the bulk GaInNAs also seems likely, as any strain fields introduced would occur near the GaAs/GaInNAs interface close to the bottom of these optical samples.

Other possible mechanisms behind this defect feature are donor-acceptor or electron-acceptor transitions, or an LO-phonon related resonance. A conduction band to acceptor

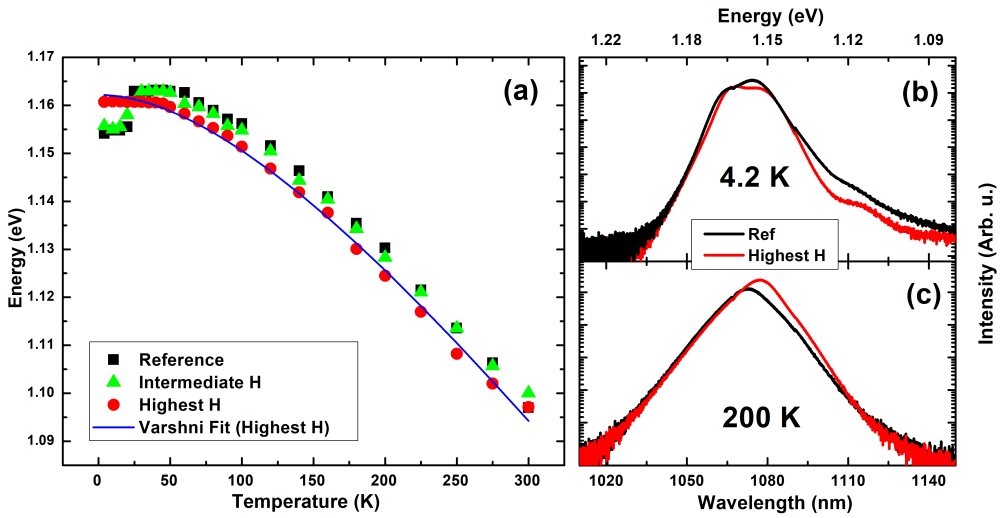

Figure 3.9: (a) Peak energy position of the PL spectra as a function of temperature for the samples studied here. (b,c) A comparison of the PL spectra acquired for the reference (black line) and highest hydrogenated sample (red line) taken at 4.2 K and 200 K, respectively.

impurity transition has also been observed in p-type GaInNAs [110], and the samples studied here are slightly, though unintentionally, p-type. Though much deeper than the similar transition in GaAs, the observed position of the impurity level at 42 meV below the conduction band [111] appears consistent with the position of the E_D feature at 4.2 K. However, the constant energy separation between E_D and E_G of 40-50 meV may also suggest a LO-phonon emission replica (2LO) [112]. The origin of this feature remains under investigation.

As previously discussed, at the highest power a removal of the characteristic 's-shape' was observed for the highest hydrogenated sample. This temperature dependence of the peak energy for the three samples is compared in Figure 3.9 (a). Over the temperature range where the band gap emission is dominant and follows traditional Varshni behavior [25], an

additional energy shift is evident for the highest hydrogenated sample. This reduction in the peak PL energy of the band gap at 30 K of ∼4 meV likely reflects relaxation of strain in the material, which is initially introduced by nitrogen during growth [91], and is reduced with the formation of N-H centers [97]. This hydrogenation serves to displace the Ga atoms, and expand the Ga-N bond, both which result in shifting the band gap to lower energies. Other shifts in the gap energy may result from the out-diffusion of nitrogen and/or indium during the hydrogenation process, though these would both result in a blueshift of the energy, which is not observed and thus not expected here.

Hydrogenation not only affects the relative change in emission intensity between the main band gap and other features, but also the overall PL intensity. To illustrate this change, a comparison between the PL spectra of the reference and the highest hydrogenated samples taken at 4.2 K and 200 K is shown in Figure 3.9 (b) and (c), respectively. The intensity of the reference PL at 4.2 K is observed to be greater than the hydrogenated sample, while at 200 K the PL emission of the reference is slightly lower. This behavior appears consistent with increased numbers of centers in the reference sample that localize carriers. At low temperature, these centers serve to confine photogenerated carriers and increase radiative recombination, while at higher temperature, these centers may contribute to non-radiative recombination. In the case of the hydrogenated sample, carrier localization is weaker, and thus radiative recombination is reduced. This appears beneficial, particularly in systems like GaInNAs and quantum dot solar cells, where evidence suggests carrier collection is limited by radiative recombination [85], [113].

As yet in this discussion, the source of these localization centers has not been discussed. Fluctuations in the alloy composition, observed by several groups to be driven by indium

segregation [81], [82], [94], would form local minima in the band gap potential, localizing carriers under a certain lattice temperature. However, here a feature associated with carrier localization appears affected by hydrogenation. It is unknown how the introduction of hydrogen would affect the currently accepted understanding behind this carrier localization, as DFT results have shown indium in GaInNAs to be relatively unaffected by hydrogen, though hydrogenation of an In-N complex can occur [114]. That is, other species, such as Ga, N, and larger nitrogen clusters in the material form bonds more readily when hydrogen is introduced, as compared to indium. A study in GaInNAs QW structures reported no variation in the localization energy (the 'depth' of the 's-shape') with different indium concentrations or QW thicknesses, and attributed this localization to nitrogen composition fluctuations [115], which may also be the mechanism here. Other possible mechanisms behind this localization include states introduced by the difference in size and electronegativity of arsenic and nitrogen (isoelectronic centers), or strain introduced in the sample.

Mentioned briefly above, there have been some advances in using Sb to improve material quality when growing GaInNAs, and high efficiency photovoltaic devices have been produced using these methods [72], [116]. However, this use of Sb in GaInNAs and in GaAsN appears to increase the prevalence of alloy fluctuations [82]. The material quality appears to improve, but evidence of unavoidable defects may not be apparent as carrier localization at these alloy fluctuations will screen the defects. This behavior has been observed in InGaN, where QD-like alloy fluctuations screen the problematic defects from the charge carriers [81], [83]. These defects, though screened, will still serve to reduce the performance of photovoltaic devices, particularly with respect to lifetime and yield. Therefore, hydrogenation as a selective

passivation process may still impact and improve the lifetime and performance of GaInNAs:Sb solar cells [81], [82].

3.2.3 Density Functional Theory results and Discussion

To better understand the mechanism behind the passivation of defect states and carrier localization effects, the nature of bonds and complexes formed by nitrogen and hydrogen (N-H) were investigated by density functional theory calculations. These computational investigations were performed by our collaborators in the Department of Chemical, Biological and Materials Engineering at the University of Oklahoma [114]. To first order, the added electronic effects of substitutional nitrogen are screened by the addition of hydrogen atoms. At high concentrations, this results in the complete removal of the band gap reduction [93].

The VASP package is used for these calculations [118], where a supercell of 64 atoms is generated, with 32 As atoms, 29 Ga atoms, and 3 In atoms for an InGaAs structure, which is displayed in the insets to Figure 3.10. For the GaInNAs material, one N atom is substituted for one of the As atoms, which corresponds to a nitrogen concentration of 3%, comparable to the samples investigated here. Hybrid functionals [119] with a k-point sampling of $3 \times 3 \times 3$ are used to calculate the density of states for the different materials, which are plotted as the black curve ($In_xGa_{1-x}As$), red curve ($Ga_xIn_{1-x}N_yAs_{1-y}$), and blue curve ($Ga_xIn_{1-x}N_yAs_{1-y}$-H) in Figure 3.10, respectively.

As nitrogen is introduced to the InGaAs alloy, a local maximum in the density of states is observed (red curve) at the bottom, or perhaps just below the conduction band. In the inset to Figure 3.10, these states (and subsequent photogenerated electrons) can be seen to be localized around the nitrogen atom. These insets show the supercell, where the charge

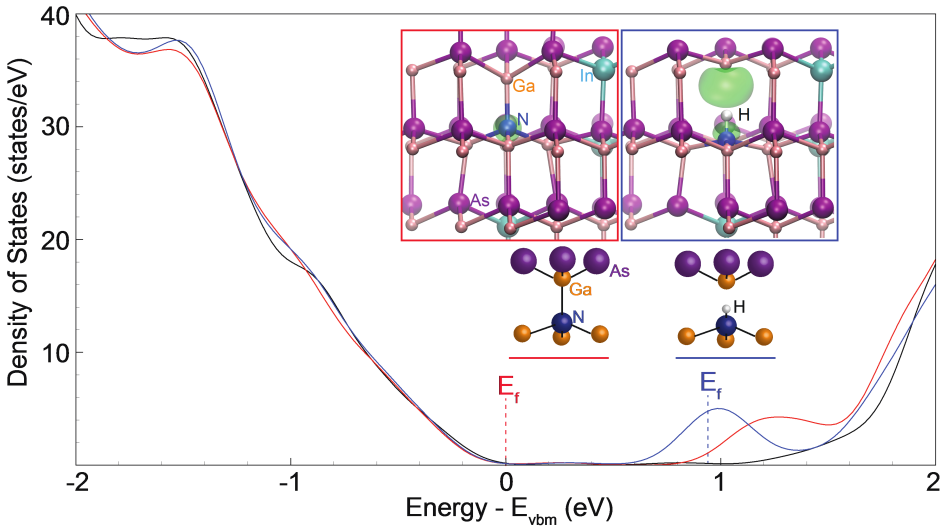

Figure 3.10: Density of states calculated by DFT methods plotted for InGaAs (black line), GaInNAs (red line), and GaInNAs-H (blue line). Insets show the supercell used with the charge density within 0.4 eV above the conduction band plotted as an isosurface, for the GaInNAs in the left inset and the hydrogenated case (GaInNAs-H) in the right inset. Reproduced from Ref. [117] with permission from the Royal Society of Chemistry.

density within 0.4 eV above the conduction band is shown as the colored surface. This local maxima appears consistent with the band anticrossing model, where the reduction of the band gap is a result of the introduction of nitrogen related states close to and resonant with the conduction band. The Fermi energy (E_f), or maximum occupied equilibrium state, is also plotted as dotted lines in Figure 3.10, and for both InGaAs (black) and GaInNAs (red) E_f is located at the top of the valence band.

For the singly hydrogenated case, the charge density surface is shown in the right inset to Figure 3.10, where the electrons now remain close to the Ga atom. This localization of electrons close to the gallium atom is the result of dangling bonds released by the hydrogenation of

the nitrogen atom. The formation of this N-H center with a single hydrogen atom appears to act as a donor in this system, as the Fermi energy is seen to shift into the local maxima at the bottom of the conduction band. This is consistent with previous studies of MOCVD grown dilute nitrides using hydrogen based precursors, where different growth parameters were seen to change the background doping [98], [120].

Increasing the hydrogen concentration by adding an additional hydrogen atom to the supercell results in the formation of N-H_2 complexes, and three of those with the lowest formation energy are investigated, with supercell and density of states plotted in Figure 3.11. The complexes N-H-H-Ga (green dashed) and H-N-H-Ga (purple dashed) are noted to have a more similar electronic structure, while N-H-Ga-H (orange) appears to retain an inflection in the density of states at the bottom of the conduction band, more akin to the singly hydrogenated case. In all of the doubly hydrogenated cases, the removal of states in the band gap is consistent with a previous report that calculated the formation energy of the N-H-Ga-H and H-N-H-Ga complexes [96].

All three configurations result in the removal of the local maxima in the density of states near the bottom of the conduction band. These states appear to move either up into the conduction band continuum, or down into the valence band. In either case, the resulting band structure appears similar to that calculated for InGaAs (black curve in Figure 3.11), which may explain the behavior observed by Polimeni *et al.* and mentioned previously. With hydrogenation, a shift in the PL emission energy was observed, from that of GaInNAs to that of InGaAs, showing a removal of the effect of the substitutional nitrogen [93].

The strength of the bonds formed by the extra hydrogen atoms is investigated by calculating the binding enthalpy for the atoms in each configuration. When the nitrogen

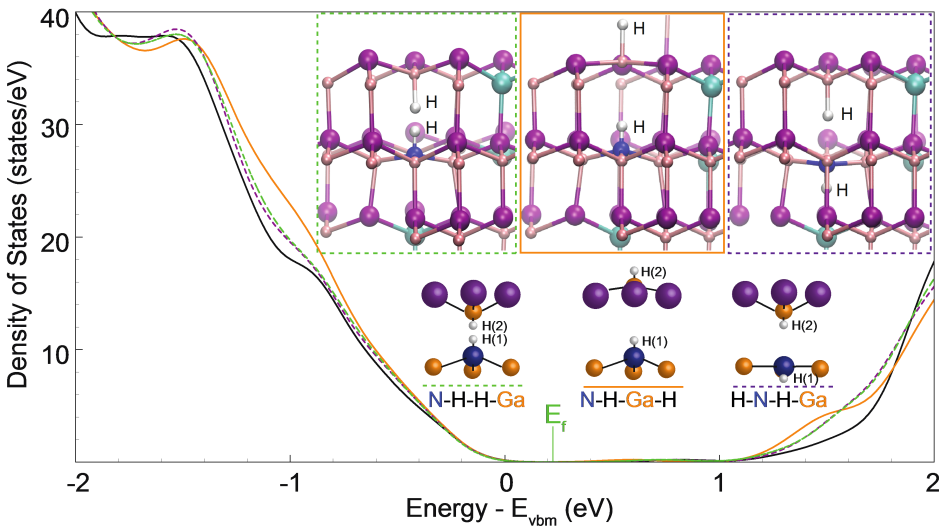

Figure 3.11: Density of states calculated by DFT methods plotted for InGaAs (black line) and three configurations of doubly hydrogenated GaInNAs-H_2. N-H-H-Ga is shown in and density of states is plotted by the green dashed line. N-H-Ga-H and H-N-H-Ga are likewise shown by the orange solid and purple dashed lines, respectively. Reproduced from Ref. [117] with permission from the Royal Society of Chemistry.

center is the sole place of hydrogenation, this binding energy is -0.49 eV per hydrogen atom. For the more likely configurations investigated here where N and Ga receive hydrogen bonds, binding energy calculations for each hydrogen atom give -0.72 eV for N-H-H-Ga, -0.75 eV for H-N-H-Ga, and -0.60 eV for N-H-Ga-H. A more negative binding energy here indicates a more energetically favorable configuration, and thus more likely at high concentration. These binding energy values also suggest removal of the hydrogen atoms is relatively easy when annealing at moderate temperatures, when including entropy effects. This result also appears consistent with the early PL results of Polimeni *et al.* that showed a return to the original GaInNAs PL emission energy upon annealing, indicating a removal of hydrogen [93]. Of the

three doubly hydrogenated configurations, the N-H-H-Ga structure may result in the easiest removal of hydrogen with annealing, as the proximity of the hydrogen atoms can facilitate their recombination.

The DFT calculations outlined here do not (indeed cannot with this size supercell) include anything similar to alloy fluctuations. However, the movement upon hydrogenation of these states correlated with nitrogen may reflect a contribution to carrier localization, and resulting decrease in emission from these states in the PL. For solar cell performance, it should be noted that even if states are moved into the continuum, the passivated defect centers responsible may still act as scattering centers, which can affect transport. Further measurements would be required to understand the transport properties.

3.3 Doping Effects of Hydrogen in GaInNAs

As mentioned previously in this chapter, a change in background doping has been observed in MOCVD grown samples when different hydrogen conditions were used [98], [120]. Additionally, the DFT calculations outlined previously suggest the N-H complex acts as a donor when formed. Preliminary C-V and impedance spectroscopy studies on the solar cells studied by Fukuda *et al.* appear to show a shift in the location of the junction upon hydrogenation, which indicates a change in the doping. In order to further investigate these doping effects of hydrogenation, a selection of n-type and p-type optical GaInNAs samples were selected and subjected to the UV-activated hydrogenation process.

3.3.1 Experimental Details

The optical samples investigated here have a similar structure to the samples investigated in the first section of this chapter, except that the dilute nitride layer is 2 µm thick, and the GaAs cap is ∼20 nm thick. All samples were initially subjected to a rapid thermal annealing process (850 °C for 30 s) to improve material quality. Selections of each sample type were kept as references, while the others were send to Amethyst Research Inc. for the UV-activated hydrogenation process, which was performed with similar conditions to the "highest" hydrogenated sample described earlier in this chapter. The GaAs cap was removed prior to PL measurements using common GaAs etchants. PL measurements were performed as outlined in Chapter 2, with the 632.8 nm being the excitation wavelength used here.

3.3.2 Experimental Results and Discussion

Temperature dependent PL measurements acquired from the reference and hydrogenated samples are shown in Figure 3.12 (a,b,d,e). Clear signatures of carrier localization are evident in both the p- and n-type reference samples, and furthermore in the temperature dependent peak energy in Figure 3.12 (c). A characteristic 's-shape' [92], [96], [100], [117] is observed for both the reference samples, and this carrier localization is extremely robust in the n-type reference, remaining the dominant peak until 200 K. For the p-type reference, there is a shift from the initial peak (D1), to an intermediate peak (D2), and finally to the band gap emission (E_G). The initial dominant peak is related to carrier localization by alloy fluctuations, while the intermediate peak is attributed to emission from isoelectronic centers and/or a conduction band to Be acceptor transition [110]. A large impurity band is also observed in the p-type reference, and is the brightest emission in the PL spectra from 25 to 60 K.

In the n-type reference, evidence of an impurity band is also observed, though the relative contribution to the emission is lower with respect to the p-GaInNAs. The dominant peak at low temperature may be representative of donor-acceptor pair transitions in this n-type sample [121], since both impurity types are present, in addition to other non-idealities and mid-gap states.

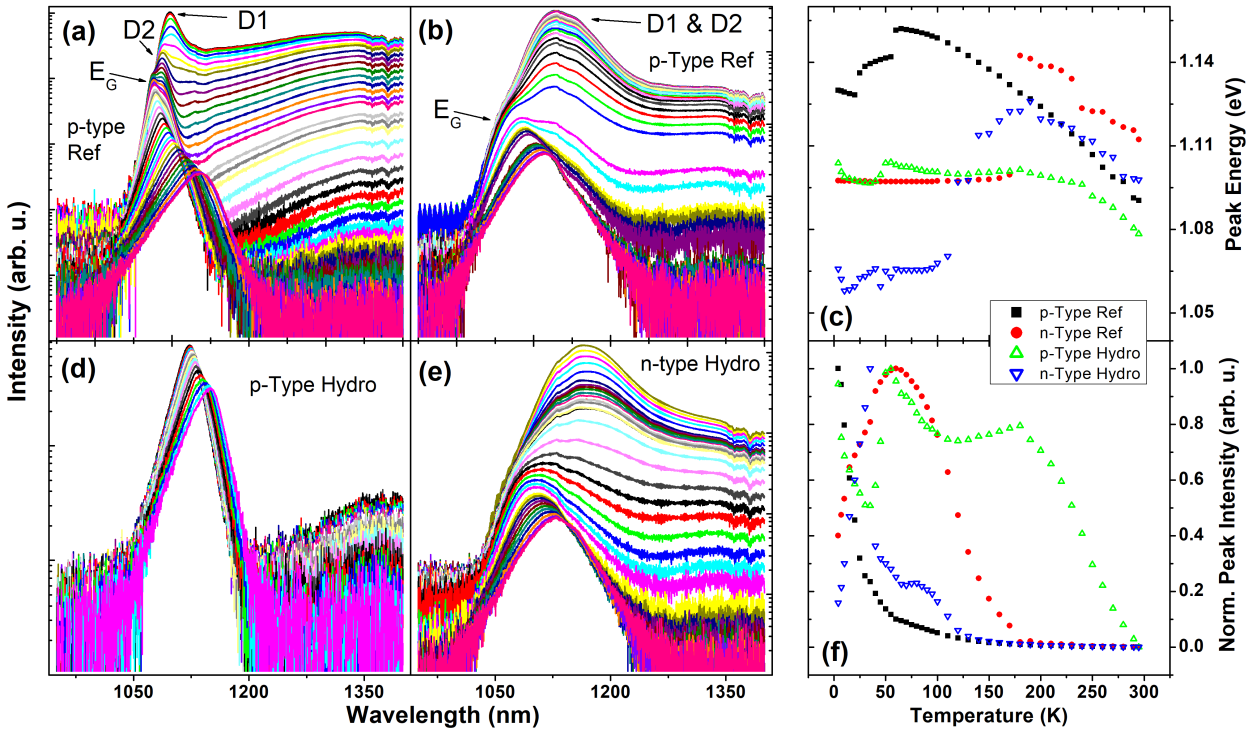

Figure 3.12: Temperature dependent PL spectra for the (a) p-type reference, (b) n-type reference, (d) p-type hydrogenated sample, and (e) n-type hydrogenated sample. Peak energy position and normalized peak intensity for each sample as a function of temperature are compared in (c) and (f), respectively.

Upon hydrogenation, an extreme change is observed in the PL spectra of the p-type sample. The impurity band is greatly reduced as has been observed previously, which was attributed to the filling of vacancies and passivation of impurities [92]. Additionally, the PL

spectra appears to be a single peak rather than multiple contributions. This reflects the effect of the hydrogen in passivating isoelectronic and deeper nitrogen cluster related trap states. In this p-type doped sample, the nitrogen related electron traps are only partially depleted by the excess holes from doping [122], and thus still display localization features before hydrogenation. Upon hydrogenation, many of the N-related traps are passivated by the hydrogen, and N-H complexes form that serve to act as donors, changing the doping from P-type to more intrinsic in nature. As there are less trap-states after hydrogenation, the holes from the p-type dopants are now able to deplete these states, resulting in recombination of photogenerated carriers primarily through band-to band processes.

However, the peak energy and intensity behavior with temperature of this p-type hydrogenated sample (shown in green triangles in Figure 3.12 (c,f)) are not typical of a traditional III-V semiconductor. The energy dependence does not follow the typical Varshni behavior [25], and appears to be correlated with changes in intensity. Such anomalies in the energy dependence may still be indicative of carrier localization, as the PL spectra has shifted to lower energies as compared to the reference for the entire temperature range investigated.

For the n-type sample that underwent hydrogenation, there are some differences in the PL spectra, though the qualitative behavior is relatively unchanged. A slight reduction in the impurity band intensity is observed, as is a softening of the 's-shape'. A reduction of the peak energy for the whole temperature range is observed, as well as a slight increase in the depth of the 's-shape', which may reflect a relaxation of strain upon the slight annealing conditions of the hydrogenation process. The overall behavior of the n-type sample appears consistent with the hypothesis suggested above, as no p-type dopants are introduced to deplete the electron traps, even though some of these electron traps may have been passivated.

These results, and preliminary Hall measurements on these samples (not presented here) suggest that the introduction of hydrogen in GaInNAs does produce an effect in the doping, namely to be more n-type in nature, which is driven by the formation of N-H complexes that act as donors [114].

3.4 Radiation Tolerance of a Dilute Nitride Solar Cell

To better understand how these dilute nitride solar cells would change when exposed to high energy particles outside the atmosphere of Earth, a sample was exposed to high-energy proton irradiation. As discussed in Chapter 1, high energy radiation is the main source of degradation encountered in space missions, and so it is important to understand how new materials will react to this energetic bombardment.

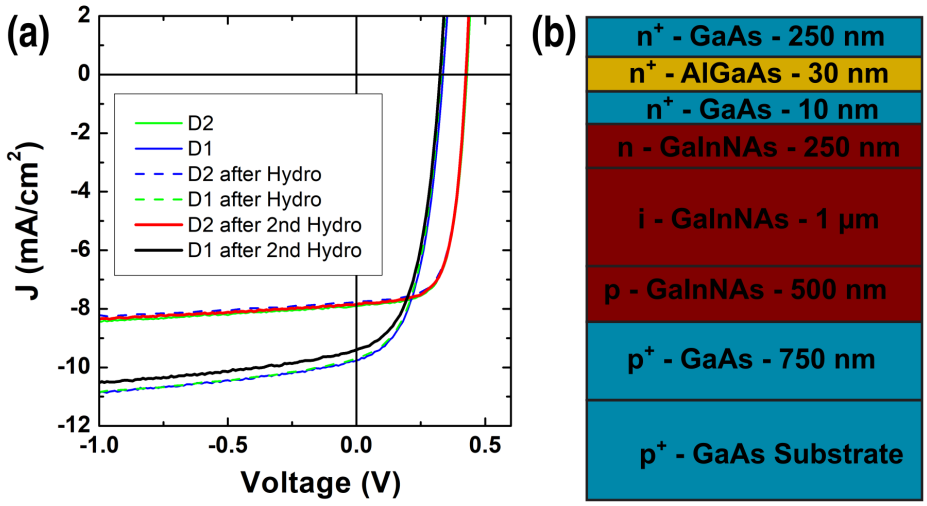

Figure 3.13: (a) Light J-V data for the devices studied in this section before and after hydrogenation. (b) Sample structure of the devices studied here.

It should be noted that some tests of UV-activated hydrogenation, as outlined earlier in this chapter, were performed on the devices (D1 and D2) studied in this section. However, little to no effect upon hydrogenation was observed, according to light J-V measurements taken at room temperature (see Figure 3.13 (a)). Unlike previous studies [92], the sample studied here was processed into a solar cell device *before* hydrogenation, which appears to have lessened the efficacy of the process. These initial results are unfortunate, as it was hoped that the UV-activated hydrogenation step could be integrated into the final contact annealing. More research needs to be performed to determine the mechanism that prevented any observed hydrogenation effects in these devices. The irradiation tests here were performed on device D1, of which the initial J-V characteristic is shown in Figure 3.13 (a).

3.4.1 Experimental Details

The sample investigated here was grown by MBE and processed at Sharp Laboratories of Europe Ltd., with the sample schematic shown in Figure 3.13 (b). To probe the stability of this material system in space radiation conditions, this sample was irradiated with 1.5 MeV protons to a fluence level of 1×10^{11} H/cm^2, using Amethyst Research Inc. Van de Graff accelerator facilities. Temperature dependent J-V and EQE measurements were performed before and after irradiation, to illuminate any changes. Only one device was irradiated (D1), and as the beam size of the high energy proton beam is $\sim$5 mm, it is assumed that the second device (D2, placed more than 15 mm away) received little radiation exposure.

3.4.2 Experimental Results and Discussions

To probe the effect of the proton irradiation on this dilute nitride solar cell structure, temperature dependent PL measurements were performed (see Figure 3.14 (a and b)). PL taken of the second device, placed some distance away (and therefore unexposed) from the irradiation beam, represents the pre-irradiated behavior of the main device tested. Both temperature dependent PL spectra show a shift from a lower energy peak (P3) to a higher energy peak (P1) around 100 K, clearly seen in the energy dependence shown in Figure 3.14 (c). As previously outlined in this chapter, P3 is related to carrier localization due to alloy fluctuations and/or isoelectronic centers, while P1 is emission from the band gap. Figure 3.14 (a) also shows a shoulder labeled P2 that appears to be related to the bulk dilute nitride material.

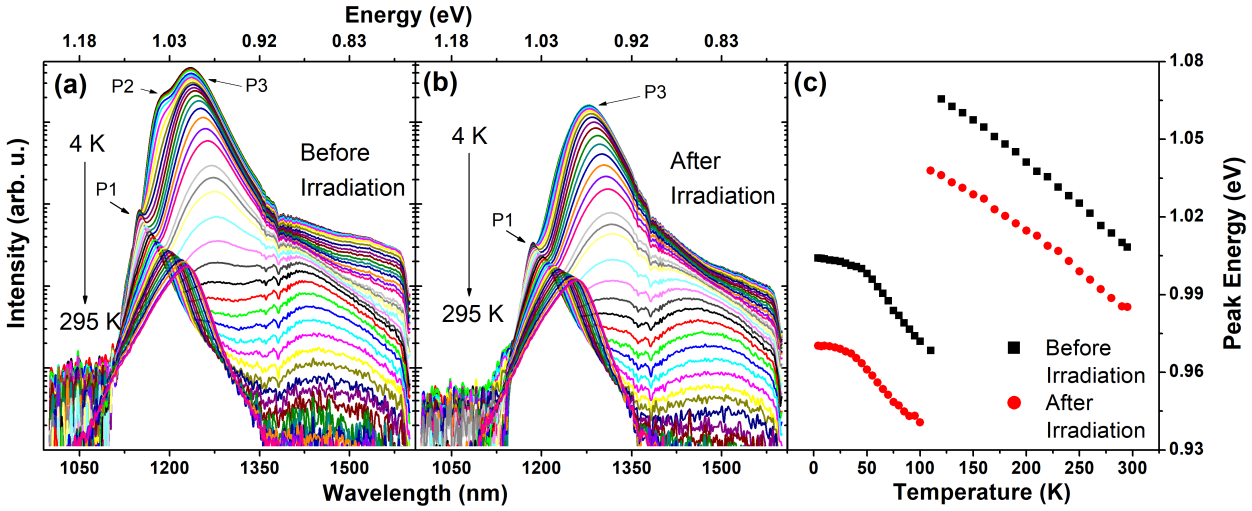

Figure 3.14: Temperature dependent PL spectra for the (a) reference device (D2) and the (b) irradiated device (D1). (c) Peak energy of the PL spectra as a function of temperature.

In comparing the before and after cases, a clear shift to lower energies of the entire spectra is observed, as is evident in Figure 3.14 (c). The overall shift in energy appears to reflect a relaxation of strain upon proton irradiation, that presumably occurred during growth of the dilute nitride layers, and/or subtle differences between the doped and undoped dilute nitride layers present in this device (see Figure 3.13 (b)). The shoulder feature (P2 in Figure 3.14 (a)) is significantly affected by irradiation, being either pushed into, or becoming degenerate with the continuum. This appears to reflect a change in the band structure due to changing strain conditions, which are known to considerably affect the bands in InGaAs systems [123].

Here, however, the observed effects are likely two-fold, one part due to the relaxation of strain and/or material inhomogeneities, and another part due to differences between the two devices measured here (D1 and D2). In Figure 3.13 (a), the J-V curves of devices D1 and D2 are plotted, where it is observed that D1 has a lower V_{oc} and higher J_{sc} as compared to D2, reflecting a lower band gap in D1. This may be due to different annealing conditions performed on these devices when processed at Sharp or differences in material composition across the wafer after growth. Thus, while this other device may not have had significant radiation exposure, it does display a shift in the gap from previous experiments, which makes the comparison here non-trivial.

To further illuminate these changes, EQE measurements of the device were performed before and after irradiation at various temperatures, which are plotted in Figure 3.15 (a and b). There is reduction in the EQE observed over the whole collection area of the device. This is expected, as high energy particles will bombard the material and introduce vacancy and interstitial defects throughout the structure which will serve to increase recombination losses. There is a slight increase in the EQE at energies greater than 2.25 eV, though this is

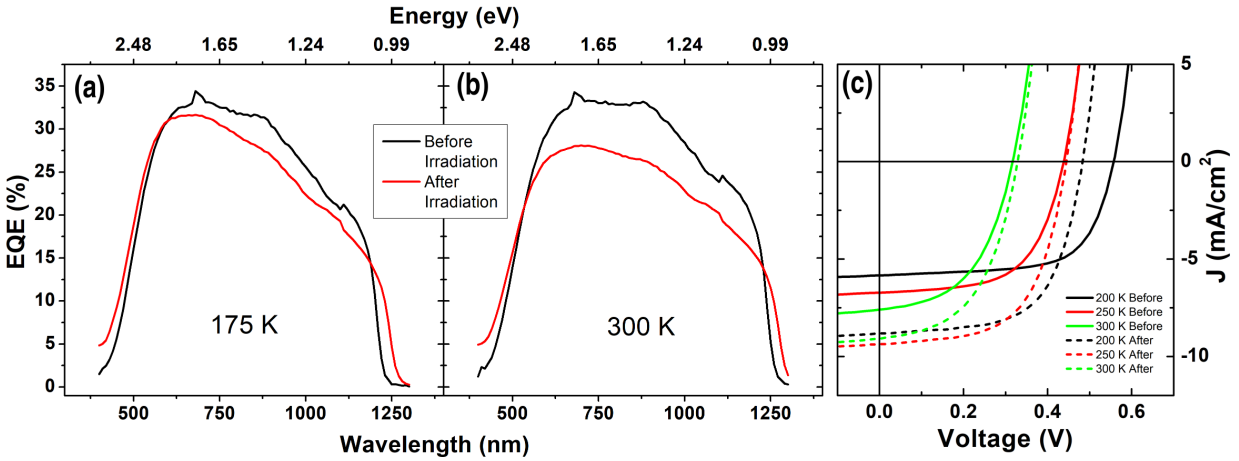

Figure 3.15: (a,b) EQE of the irradiated device (D2) acquired before and after irradiation, for 175 K and for 300 K, respectively. (c) J-V data taken before and after irradiation for selected temperatures.

likely within the error of the measurement. At all temperatures investigated, there is also a noticeable shift to lower energies in the absorption edge of the EQE. This is consistent with results observed in the PL, indicating a relaxation of strain after irradiation. This relaxation of strain upon irradiation has been observed in some preliminary studies by our group on GaAs based quantum dot solar cells [124], and the exact mechanisms are currently under investigation.

J-V data taken before and after irradiation is plotted in Figure 3.15 (c) for a few select temperatures. An increase in J_{sc} is observed for all temperatures here, which is consistent with the decrease in band gap, though absolute differences must be considered with care as this does not match the magnitude of the reduction as observed in the EQE. Additionally, the lowered band gap does not result in a loss in V_{oc} at higher temperatures, as is expected.

As such, these effects are likely more related to systematic effects, and further measurements are necessary to confirm this hypothesis.

3.5 Conclusion

In this chapter, dilute nitride optical samples and solar cells are studied to determine effectiveness as an additional junction for epitaxially grown multijunction solar cells. Material quality issues in GaInNAs have prevented its commercial use thus far, and careful hydrogenation has been suggested as a possible defect passivation process. Previous studies by our group showed improvement in the EQE and J-V characteristics with this UV-activated hydrogenation process [92].

To further understand the effect of the hydrogen on the GaInNAs material and defects, optical samples were studied via temperature and power dependent PL. Two levels of hydrogenation were performed on the samples, of which the reference and highest hydrogenated sample are compared. Temperature dependent PL spectra show a dominant peak associated with carrier localization at low temperature, and as the temperature increases, emission from the band gap becomes the dominant emission mechanism. This results in the 's-shape' energy dependence typically seen in these systems. In the hydrogenated sample, the contribution of emission due to carrier localization is reduced, resulting in the removal of this 's-shape' at higher incident powers. This emission is not completely removed, indicating a higher concentration of hydrogen is needed to fully passivate the defects responsible for this feature.

Power dependent PL measurements give more information about the emission mechanism of each feature, and illuminate a lower energy feature E_D related to defects, which appears

unaffected by hydrogenation. A slight blueshift with energy is observed with power in the carrier localization peak, indicating state filling of local potential minima. These minima have been understood to be due to alloy fluctuations driven by indium segregation, though DFT studies have shown indium to be relatively unaffected by hydrogen [114]. Studies in GaInNAs quantum wells assigned these alloy fluctuations to be related to nitrogen [115], which is more consistent with the results presented here.

DFT calculations were performed to investigate the effect of increasing hydrogen concentration on the GaInNAs band structure. Introducing nitrogen to the InGaAs material results in a local maxima in the density of states close to the bottom of the conduction band, resulting in a lowering of the conduction band, and is consistent with the band anticrossing model suggested for these systems [68]. Producing N-H complexes by bonding a hydrogen to the nitrogen in the system results in a slight shift of this local maxima to higher energies. In addition, the Fermi level is shifted upward, indicating that the N-H complex is acting as a donor in this material. Further hydrogenation results in the local maxima being pushed into the continuum, and a return to the band gap of the InGaAs.

A set of p- and n-type optical samples were subjected to hydrogenation to better determine the effect upon the doping and possible changes in the electrical behavior of the solar cells. Temperature dependent PL measurements showed a large change in the spectra of the p-type sample, while the n-type sample showed only marginal changes. This is attributed to the passivation of electron traps by hydrogenation in both samples, with depletion of remaining electron traps by the holes in the p-type sample, having a more significant effect allowing band-to band emission to dominate.

Finally, to understand the robustness of this material with respect to radiation that will be encountered in space, a GaInNAs based solar cell was subjected to 1.5 MeV proton irradiation to a fluence level of 1×10^{11} H/cm^2. A shift in the PL energy and the absorption edge in the EQE to lower energies is observed, indicating a change in the band gap as a result of relaxation of strain in the device. A reduction in the EQE is also observed, consistent with the introduction of defects and recombination centers as a result of the irradiation.

Chapter 4

Flexible Cu(In,Ga)Se_2 Solar Cells: Effects of Annealing, Low-Intensity-Low-Temperature Conditions, and High-Fluence Irradiation

Cu(In,Ga)Se_2 (CIGS) solar cells are a thin film solar cell material that has been a topic of research almost as long as silicon PV, showing record power conversion efficiencies (PCE) up to 23.4% [8]. These high efficiencies, along with low productions costs, low weight and compatibility with flexible substrates mean that CIGS photovoltaics offer a compelling alternative to standard photovoltaic technologies, particularly in certain niche applications [47], [125]–[128]. Commercially available CIGS modules have been available for a number of years, though the reduced cost of silicon panels, and certain complexities of the CIGS system continue to limit the market share of CIGS photovoltaics.

This chalcopyrite quaternary system can be complex, which manifests itself in a number of material issues, including phase segregation, non-stoichiometric composition [129], [130], the formation of grain boundaries and/or defect complexes [131], [132]. As such, it is somewhat remarkable that devices based on these materials with so many non-idealities can achieve high PCE. Many of the subtleties of CIGS devices are apparent under different measurement technique conditions, changing their behavior, for example the J-V response after exposure to different light conditions, high temperatures and/or applied biases [133]–[139]. This *metastable* behavior has been attributed to the presence of a divalent V_{Cu}-V_{Se} defect center, which can change charge states from a shallow donor to various acceptor states [134]. The change from one charge state to another is mediated by carrier capture, and is metastable in either state

under a certain temperature (160 - 200 K). This model has explained many of the phenomena observed in CIGS devices, though there is still much discussion in the community, as certain observed behaviors could be explained by other interfaces and defects [140]. Regardless, the effect of these changing conditions results in increased acceptor concentration in the absorber, which can lead to increased recombination losses in the absorber and at the CdS (window layer)/CIGS interface [135], [141].

In comparison to the study of this material system for terrestrial power applications, CIGS have been relatively unexplored for space applications, especially newer devices grown on lighter flexible substrates rather than soda lime glass. The lighter weight of thin film solar cells means a higher specific power compared to thicker materials, and flexible substrates suggest deployable solar cells with large packing volumes might be possible in smaller spacecraft. Most research on CIGS for space applications has focused on the radiation tolerance of the material [11], [142]–[144], which has shown substantial resilience in comparison to traditional space photovoltaics [22], [145]. This impressive radiation tolerance makes this material system attractive for certain outer planetary missions, particularly those around Jupiter, as discussed in Chapter 1.

As little research has been performed on this system under the conditions of these outer planets, and since these LILT conditions expose features and performance issues not present at room temperature, it is important to investigate CIGS under these specific conditions to assess their feasibility for such missions. Of particular interest is the effect of the metastability under such extreme conditions, and any barriers which would become more prevalent at low temperature. Here, commercially available flexible CIGS solar cells are investigated under a

number of extreme conditions, including annealing studies, the LILT conditions described in Chapters 1 and 2, and irradiation by high energy protons.

This chapter is partially based on Brown et al.'s paper published in *IEEE Journal of Photovoltaics*, vol. 9, no. 2, pp. 552-558, Mar. 2019.

4.1 Experimental Details

The CIGS solar cell structure studied in this chapter were produced in a production-scale roll-coater tool, where sputter deposition is used to define all layers in the stack sequentially as a 50-µm thick stainless steel substrate travels through the tool [146]. Sheets of this material were shipped to the University of Oklahoma, where small samples were cut out of the larger sections. Aluminum metal grid and annular contacts were patterned on the stack using standard photolithographic methods. When not in use, the samples and precursor material were kept inside a nitrogen-filled dry box, to slow moisture and oxygen degradation of the aluminum doped ZnO (AZO) transparent conducting oxide (TCO) top contact.

Samples included in the radiation study were patterned with a metal grid, and sent to Amethyst Research, Inc. for proton irradiation. An RF plasma source produced the protons, which were accelerated by the 2.5 MW Van de Graff accelerator facilities, and an analyzing magnet (charge-to-mass ratio separator) was used to select $^{1}H^{+}$. The samples where irradiated with 1.5 MeV protons ($^{1}H^{+}$), with fluences ranging from 1×10^{14} to 5×10^{16} H/cm^{2}. Sample heating was minimized by limiting beam current to below 1 A.

PL, J-V (dark, light and LILT), EQE measurements, and J-V fitting were performed as outlined in Chapter 2. To better understand the nature of the metastability in CIGS,

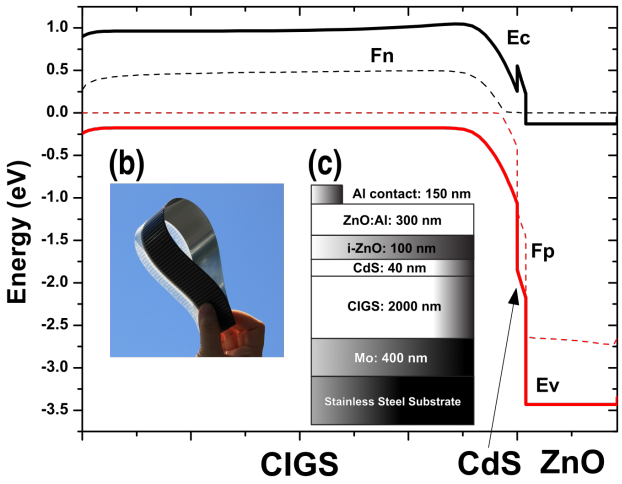

Figure 4.1: (a) Band structure of a CIGS solar cell as simulated by SCAPS-1D [147]. (b) Photograph of a flexible CIGS solar cell, courtesy of MiaSolé Hi-Tech Corp. (c) Schematic of the samples studied here.

and its effect under LILT conditions, the samples were prepared in one of two states before measurement. The as-grown, or relaxed state (R), was achieved by heating the sample to 330 K for 1 h in the dark. The metastable, or light-soaked state (LS), was achieved by light soaking the sample at room temperature (295 K) for 1 h, as is outlined by Igalson *et al.* [136].

4.2 Experimental Results and Discussions

4.2.1 Photoluminescence spectroscopy of CIGS absorber and solar cells

Initial investigation of the CIGS material began with a study of the material quality of the absorber by photoluminescence spectroscopy. Temperature dependent PL spectra for a bare absorber and for the full solar cell stack are shown in Figure 4.2 (a) and (c), respectively. From the comparison, it is clear that the emission from the full solar cell stack, despite the upper layers, is largely related to the absorber. An additional low energy feature is

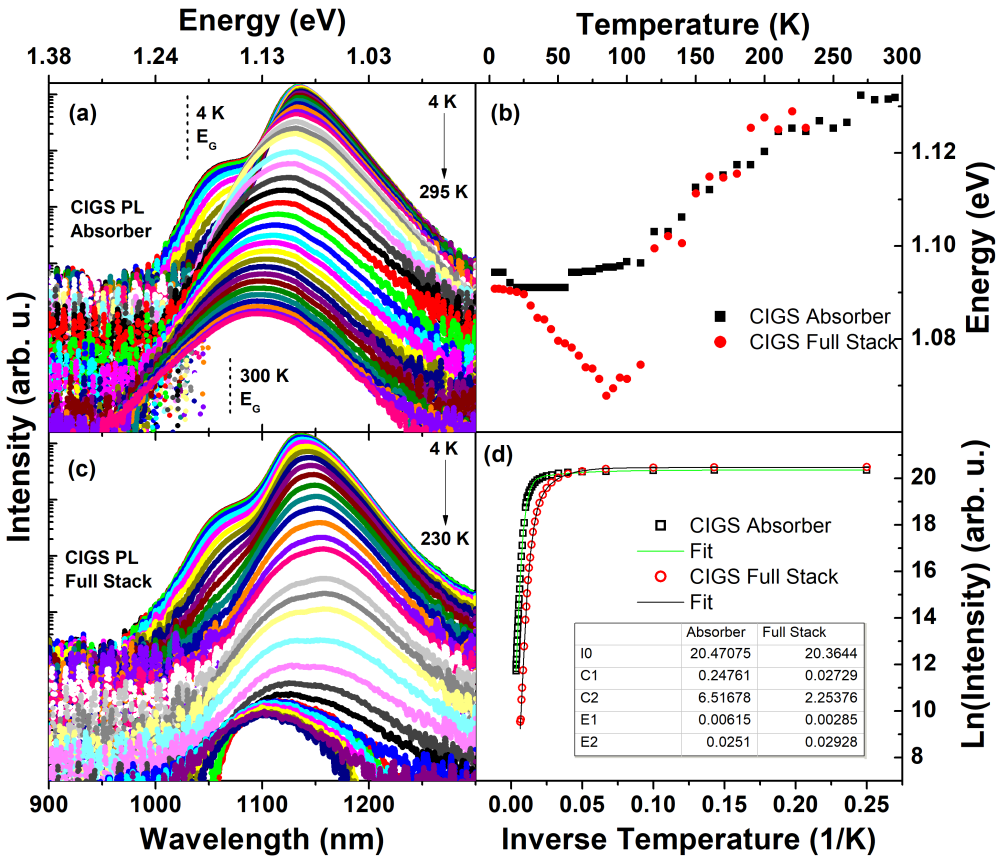

Figure 4.2: Temperature dependent PL spectra of (a) a bare CIGS absorber and (c) a full CIGS solar cell. (b) Peak position of the energy as a function of temperature. (d) Arrhenius plot of integrated intensity of the PL for the extraction of activation energies.

observed in the full stack PL, adjusting the energy dependence from 25 K to 100 K, which may indicate a separate defect center that serves to further localize carriers. This is also supported by the more complete quenching of the full stack PL around 230 K, vs 300 K for the absorber only. Additionally, it can be seen in both samples that several processes contribute to the photoluminescence, resulting in a broad PL spectrum encompassing several convoluted transitions. These features have been observed extensively in the literature [148]–

[156] and attributed to various defect and impurity related complexes associated with defects, non-idealities, and free to bound and donor-acceptor pair transitions. This is supported by the rapid quenching of the PL up to 80 K, reflected in the smaller of the two activation energies (3 - 6 meV) extracted in the Arrhenius plot in Figure 4.2 (d).

Further evidence for the defect nature of the PL is seen in the obvious redistribution of carriers through the various localized states, and the unusual energy dependence of the main peak, which does not reflect the traditional Varshni band gap dependence expected from the thermal expansion of a III-V semiconductor [25]. This unusual increase in energy with temperature may due to the redistribution of localized carriers as thermal energy increases, similar to the 's-shape' seen in the PL energy in Chapter 3. Here, such localization appears much stronger and spread over many competing centers, resulting in only the beginning of the 's-shape' which implies localization effects persist up to 300 K in CIGS systems. The dominance of localized or excitonic type recombination in the PL is also supported by comparing the PL energy at 4.2 K and 300 K with the band gap extracted from EQE (absorption) measurements, which is shown by the dotted lines in Figure 4.2 (a,c). Clearly, the band-to-band emission is screened by emission from defect and impurity related transitions. However, many of the inherent defects in this system are shallow, and so transitions related to those defects are in the region of the bulk CIGS band gap [132], and should not significantly affect the performance of the devices under terrestrial conditions. In addition to the common defects in this system, CIGS grown on stainless steel have been seen to have defects due to Fe incorporation [157], [158], which can significantly degrade the performance [157]. However, due to the inclusion of an optimized molybdenum layer at the bottom of the structures studied here, Fe diffusion is unlikely here.

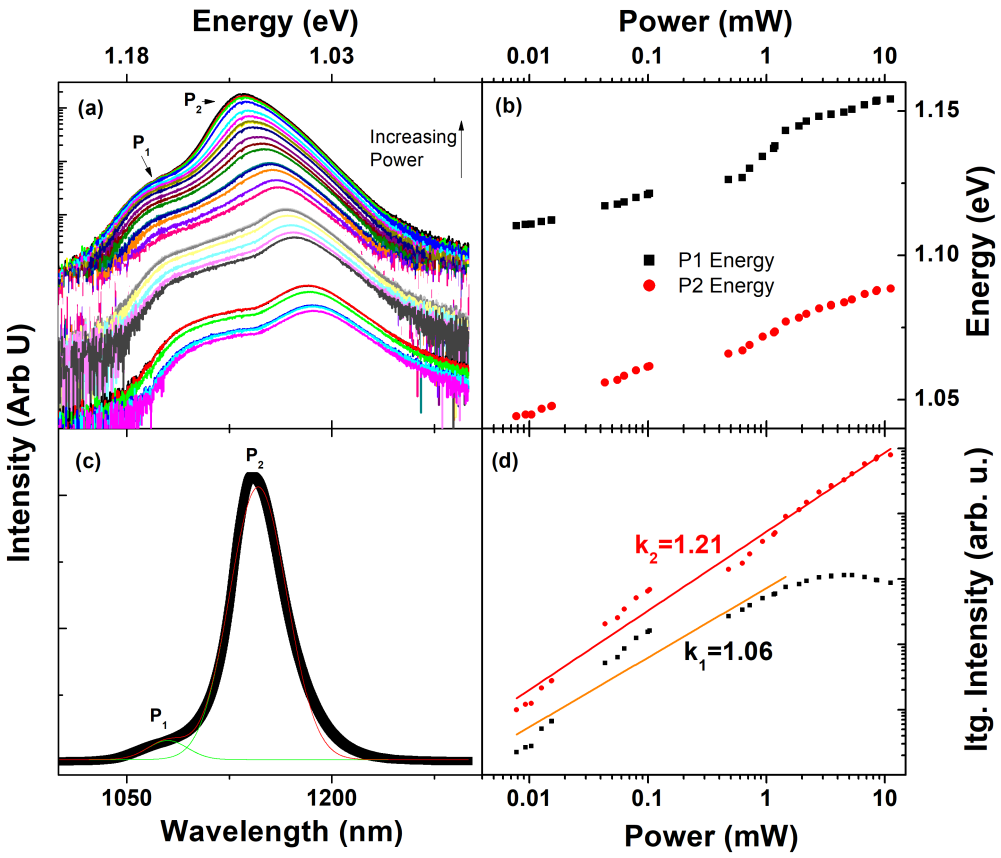

Figure 4.3: (a) Power dependent PL spectra at 4.2 K. (b) Energy of the labeled peaks as a function of power. (c) An example spectra showing the Gaussian fitting of P_1 and P_2. (d) Integrated intensity of the labeled peaks as a function of power with associated fits to a power function.

Figure 4.3 (a) shows the power dependent PL at 4.2 K. With increasing power the dominant peak shows a clear blueshift, which is commonly observed in systems that have a varying potential due to alloy fluctuations [117], [138], and may indicate compositional variations of the group-III species in the CIGS investigation here, which is consistent with the graded Ga/(In+Ga) ratio of the absorber region incorporated in the device investigated here. The power dependent PL is fit with two Gaussians, for the shoulder, and the main peak,

labeled as P_1 and P_2, respectively. The peak energy and integrated intensity extracted from these fitted Gaussians are plotted in Figure 4.3 (b,d). The power dependence of the integrated intensity is fitted to a power law $k(I \propto P^k)$, where the parameter k is indicative of either defect-related emission ($k < 1$) or excitonic related recombination ($1 < k < 2$), as described in Chapter 2. Both k_1 and k_2 (within error) lie in the range which indicate band-to-band or excitonic emission, though the anomalous energy dependence with temperature suggests excitonic behavior from carriers that are localized at defects, particularly P_1, which saturates at higher powers. Indeed, in Chapter 3, we observed a similar k value of 0.95 from a feature attributed to carrier localization.

4.2.2 Rapid Thermal Annealing Study

To investigate the effect of extreme temperatures on the CIGS solar cell material, a set of 6 samples were defined, and subjected to a range of annealing temperatures for 60 s (300 °C, 350 °C, 400 °C, 450 °C, and 500 °C) using a rapid thermal annealer, with forming gas as the environment. A reference device was produced at the same time, but not subjected to any annealing process. The J-V response of each device was recorded in dark and under AM1.5G illumination conditions, which are shown in Figure 4.4. Unusual results are observed, where the rectification behavior of the device appears to turn opposite of the initial case. This may be understood as the addition of a Schottky diode or barrier to the system, most likely at some interface, which is opposite to the direction of the main diode. Evidence of this barrier can initially be seen in the cross-over of the light and dark J-V curves of the sample exposed to 300 °C, where no crossover is observed in the reference sample. As the annealing temperature is increasing, the effect of this barrier can additionally be seen as an inflection point in the

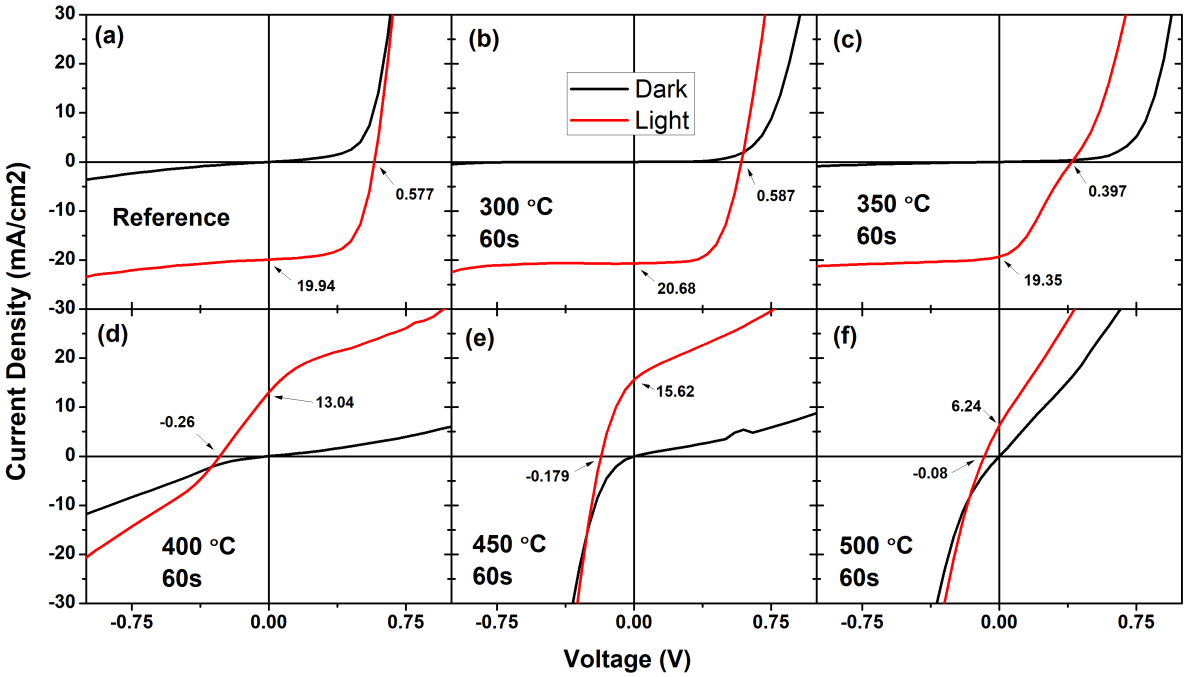

Figure 4.4: Light (red) and dark (black) J-V characteristics of CIGS solar cells taken at standard conditions after exposure to different annealing temperatures for 60 seconds. Extracted parameters of V_{oc} and J_{sc} are displayed with arrows on each plot.

light J-V curve in Figure 4.4 (c), and then a reversal of the device behavior in Figure 4.4 (d,e,f). It is clear that there is competition between the two junctions in the device, and as the annealing temperature increases, the reverse junction increases in strength, eventually becoming the dominant diode in the device. However, at high enough temperatures, the effects induced by the annealing introduces shunting, indicating degradation of the interface which initially created the Schottky diode.

Many groups working in the CIGS system have shown evidence for barriers at various interfaces. To better understand the mechanism behind this unusual behavior, photoluminenscene studies were performed on this set of samples. A comparison of the PL spectra taken

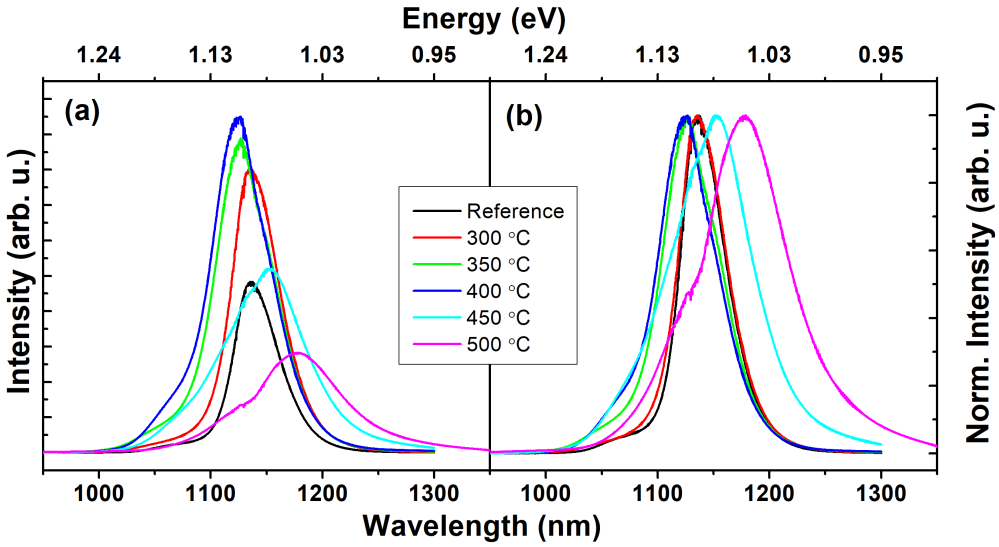

Figure 4.5: (a) PL spectra of CIGS samples after rapid thermal annealing at 5 different temperatures. Panel (b) shows the normalized PL spectra.

at 4.2 K is shown in Figure 4.5. An initial blue shift and increase in intensity is observed up to the sample exposed to 400 °C, followed by a red shift and reduction in intensity for the samples exposed to higher temperatures. As discussed in the previous section, the emission from the CIGS absorber is most likely due to recombination localized at defects or other anomalies. Selenium vacancies (V_{Se}) are a common defect in the CIGS material [156], and we might expect migration of this Group VI element out of the material with increasing annealing temperatures [155], resulting in the PL observed. As annealing temperatures increase, further non-radiative defects can be introduced in the absorber and at interfaces, decreasing the PL intensity. An increase of these and other vacancies may also affect the doping of the CIGS absorber [159], changing the location of the junction.

The back contact molybdenum can form a Schottky barrier under certain conditions, and so steps are taken to optimize this back interface. One option is the formation of a $MoSe_2$

layer at the back contact, which has been seen to be beneficial [160]. The removal of selenium by annealing would then degrade this beneficial layer, and may be the cause of this additional diode observed. Finally, the migration of Ga [161], and introduction of interstitials and other anomalies in the material cannot be discounted, and may also contribute to both the PL and J-V results observed here.

While the initial annealing temperature did improve some of the photovoltaic parameters (see Figure 4.4), this process also resulted in the formation of a non-ideal barrier, as supported by the cross-over of the light and dark J-V. Further research should be performed, though evidence presented here suggests higher temperature annealing performed in forming gas atmosphere should not be used on the CIGS devices studied here.

4.2.3 Temperature Dependent J-V and Thermal Cycling

Though the material complexity and complex defect behavior of CIGS has not been seen to affect terrestrial performance, these same issues should be studied to understand their roll in performance at low temperature, low illumination, and when exposed to strong thermal cycling. To determine the baseline performance with regards to temperature, temperature dependent J-V measurements were taken (initially) at 1-sun AM1.5G, rather than AM0 due to unavailability of the proper filter. While this initial characterization is not ideal, the qualitative behavior of the system should not be affected by the relatively small change in spectrum over the band width of the CIGS absorption. Measurements were taken between temperature extremes of 173 K (−100 °C) and 373 (100 °C), corresponding to extremes that might be encountered in low Earth orbit (LEO), though low temperatures would only be experienced during eclipse (no incident light present) of the satellite. Several temperatures

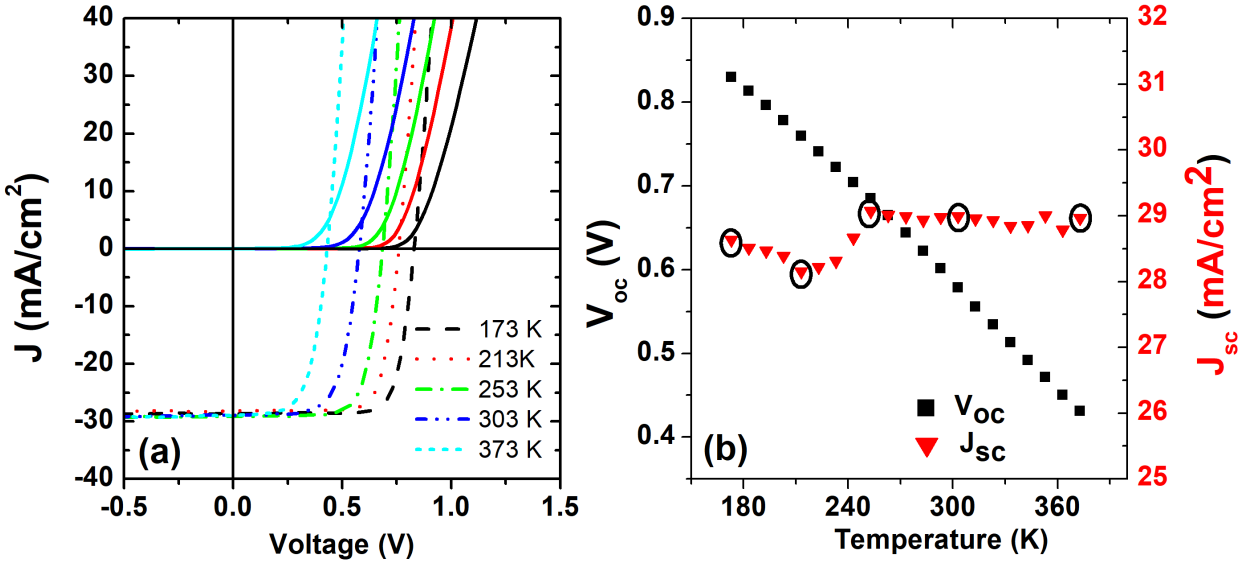

Figure 4.6: (a) Light (dashed) and dark (solid) J-V curves for selected temperatures. (b) Temperature dependent J_{oc} and V_{sc} extracted from light J-V data. The circled points correspond to the light J-V curves plotted in (a).

are recorded in Figure 4.6 (a), which shows the dark and light J-Vs between 173 K and 373 K. From the comparison of the light and dark J-V curves, a small but measurable crossover is observed in the voltages under the two conditions. This behavior, as mentioned above, has been observed by several groups working on CIGS, and is usually attributed to a barrier for minority carrier extraction at interfaces in the device, possibly at the Mo back contact [160].

In addition, this cross-over in the light and dark J-V curves could also indicate the presence of a non-idealities at the CdS-CIGS interfaces and the resulting Fermi-level pinning at these junctions [133]. Interestingly, the difference in cross-over observed at the different temperatures in Figure 4.6 (a) do not change appreciably from lower (173 K) to higher temperature (373 K). However, a marked decrease in the apparent series resistance is observed when comparing dark and light J-V characteristics. The presence of a photosensitive

barrier to carrier transport further implies non-idealities at the CIGS/CdS interface, and also within the CIGS absorber itself. Several recent articles, some on similar samples to the ones discussed here, have discussed the presence of a deep acceptor state at 0.8 eV near this interface, but this remains under debate [162], [163].

The temperature dependent V_{oc} and J_{sc} extracted from the 1-sun measurements between 173 K and 373 K is shown in Figure 4.6 (b). The temperature dependence of the V_{oc} appears typical for that of high-quality CIGS solar cells. In some CIGS systems, a roll-over in the temperature dependence of the V_{oc} at lower temperatures [164], [165] has been observed and attributed to Shockley-Read-Hall processes. While this roll-over is not present, and no roll-over of the light J-V is observed, at the low temperatures investigated here these mechanisms may still be important.

In comparison, J_{sc} does not increase monotonically as expected, instead increasing rapidly around 225 K, and subsequently behaving more conventionally. This change in J_{sc} and the associated activation energy are consistent with "unfreezing" of metastable defect states. Several groups have observed similar results within a 200-250 K window under illumination [135], [166], where this behavior appears consistent with a transition from the relaxed to light-soaked (metastable) state. While still under debate, the result of this transition is to increase the background acceptor concentration in the absorber, reduce the depletion region at the CIGS/CdS interface and to influence carrier transport across this junction. Due to this transition, recombination losses at the interface increase and result in the reduction of FF [162], [163], [167]. Despite evidence of this metastability in the temperature dependent J_{sc}, the relative contribution is quite small (~ 0.8 mA/cm^2) underlying the low

intrinsic inhomogeneities in these *commercial* devices. The effect of this transition at lower temperatures will be discussed further below.

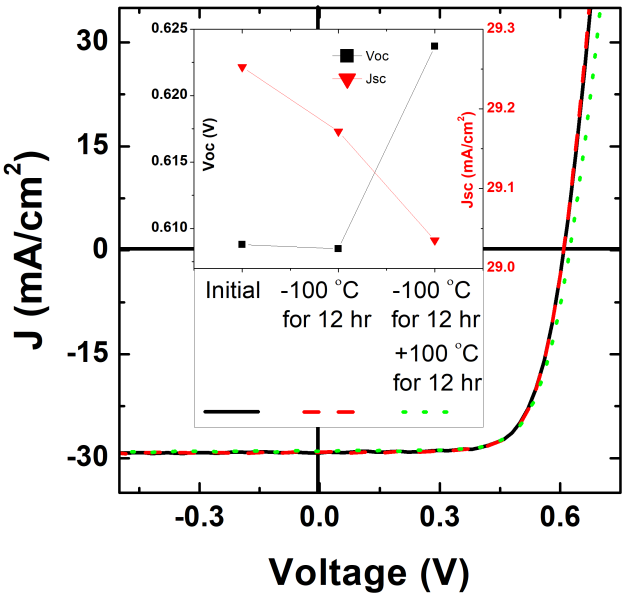

Figure 4.7: Light J-V data initial and after thermal cycling steps. The inset shows the V_{oc} and J_{sc} extracted from the J-V data.

Stability of solar cells in space may be affected by the large temperature changes that occur when transiting from illuminated to dark regions of their orbit. To investigate the stability of CIGS, measurements were performed by cooling the sample to 173 K for 12 hrs, and then heating to 373 K, again for 12 hrs. These conditions were used to approximate extremes that may be encountered in space. The samples were assessed under AM0 illumination at room temperature before and after each temperature change. J-V data is recorded at the initial state (solid black line), after the 12 hour cold stage (dashed red line), and after the 12 hour hot stage (dotted green line), shown in the main panel to Figure 4.7. The effect of thermal cycling appears negligible and is only observed under closer inspection as show in the inset

to Figure 4.7. This inset shows the V_{oc} and J_{sc} extracted from the measurements, with a small increase of ∼15 mV in V_{oc} evident after heating the solar cell for 12 hours at 373 K. Such exposure to prolonged temperatures will effectively anneal the materials and result in a sample that is presumably in the relaxed state. Annealing of this system at slightly elevated temperatures has also previously been shown to improve the V_{oc} of CIGS systems by removing and/or passivating defect centers that contribute to non-radiative losses in the absorber and at the interfaces [162], [168]. The small reduction in the J_{sc} due to long exposure to higher temperatures is again provisionally assigned to a transition from the light-soaked to the relaxed state, though it appears to have little effect under standard conditions. The overall behavior of the (admittedly limited) thermal cycling results support the stability of CIGS under these conditions.

4.2.4 Low-Intensity-Low-Temperature Results

To investigate device performance under the challenging conditions present at the outer planets, J-V and EQE measurements were performed under LILT conditions consistent with Mars, Jupiter and Saturn orbits (Table 2.1). Samples were prepared in the relaxed (R) and light-soaked (LS) states, as mentioned previously, to highlight the effect of this metastability on the J-V characteristic under these various LILT conditions.

A simple single diode model was fit to the J-V data using the methods of Zhang et al., which provided additional quantitative analysis [40]. The fits and the experimental data are shown in Figure 4.8, where (a-c) show the photovoltaic regime, and (d-f) show the forward bias or majority carrier injection region, above turn on of the main diode. The fill factor as observed qualitatively in Figure 4.8 and as extracted in Table 4.2.4 is compared, where it is

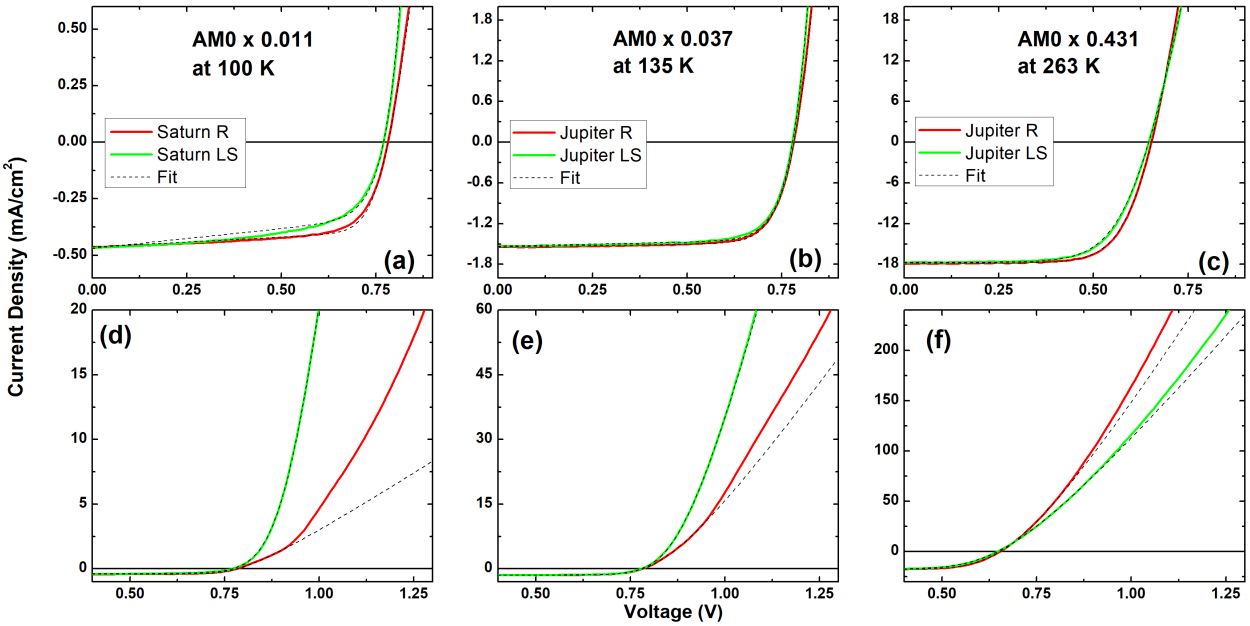

Figure 4.8: J-V results taken under LILT conditions consistent with orbits around (a) Saturn, (b) Jupiter, and (c) Mars, after preparation in either the relaxed (R) or light-soaked (LS) state. (d,e,f) highlight the J-V behavior above V_{oc} for Saturn, Jupiter, and Mars, respectively. Fits to a single diode model are shown in all cases, to highlight the deviation from the fit.

seen that the FF is universally better while in the relaxed state under all three conditions. However, while an acceptable fit is produced for all data within the photovoltaic regime, above V_{oc} the fit is lost for the lower temperature scans (Saturn and Jupiter) taken in the relaxed state. This deviation from the established fit can be seen as an inflection point in the red curves above V_{oc} in Figure 4.8 (d,e), and is evidence of the formation of a barrier to majority current flow in the relaxed state, one that is both temperature and intensity dependent. No inflection point is seen under the higher temperature conditions of the Martian orbit, which further supports the temperature dependence of this barrier. The root cause of

	J_{sc}(mA/cm^2)	J_{mp}(mA/cm^2)	V_{oc}(V)	V_{mp}(V)	FF(%)
Saturn R	0.463	0.381	0.782	0.661	71.1
Saturn LS	0.469	0.360	0.770	0.612	63.7
Jupiter R	1.54	1.42	0.782	0.648	77.2
Jupiter LS	1.53	1.35	0.772	0.66	75.8
Mars R	17.8	16.1	0.654	0.516	71.1
Mars LS	17.7	15.9	0.646	0.490	68.1

Table 4.1: Extracted parameters of J-V curves taken under LILT conditions.

this parasitic barrier is unknown, but may be due to unintentional interface states at the CdS/CIGS, the CIGS/MoO_x as mentioned above, or a combination of the two [140], [163], [164], [169].

As mentioned in Chapter 1, a loss of fill factor due to a flat spot in the J-V response has been seen in both silicon and multijunction solar cells [21], [22]. In CIGS solar cells, several groups have reported evidence of softening of the voltage or an inflection point in forward bias [136], [163], [170]. Since the effect seen here occurs primarily at low temperature, in the relaxed state, and in the forward bias regime, this suggests a barrier present at the CdS/CIGS, where increased deep acceptor states in the relaxed state may form an acceptor rich layer and inhibit carrier transport [136].

EQE measurements were performed under standard short-circuit (0 V) conditions and at the maximum power point voltage (V_{mp}) after preparing the device in the relaxed state, to gain added insight on the mechanism behind the inflection in the J-V response. As expected, carrier extraction is reduced when comparing V_{mp} to 0 V at all temperatures. The uniform reduction under bias points to an increase in resistance to transport throughout the device,

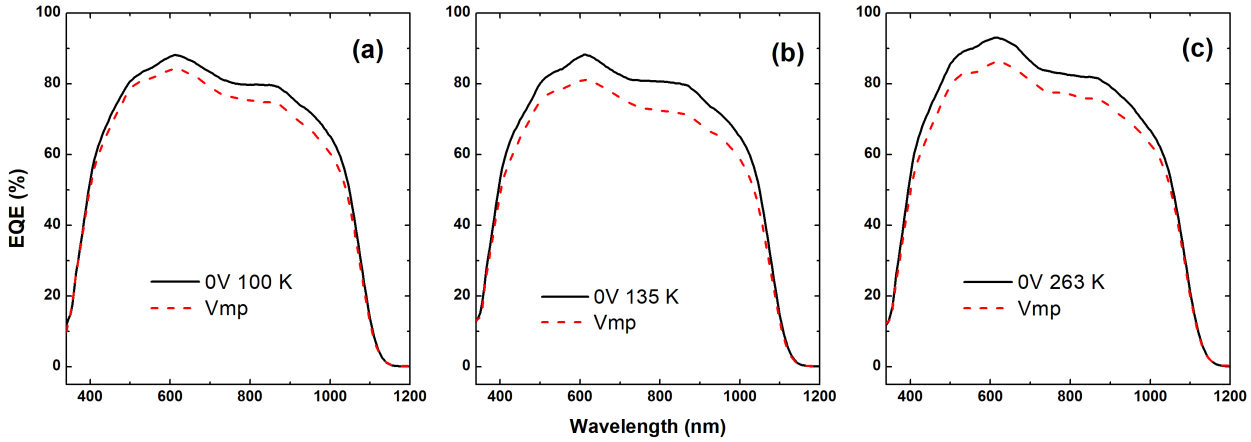

Figure 4.9: EQE data measured at short circuit (0 V) and at the max power point voltage (V_{mp}) for temperatures consistent with orbits around (a) Saturn, (b) Jupiter, and (c) Mars. Reproduced with permission from: C. R. Brown *et al.*, "Flexible Cu(In,Ga)Se_2 solar cells for outer planetary missions: Investigation under low-intensity low-temperature conditions," *IEEE Journal of Photovoltaics*, vol. 9, no. 2, pp. 552–558, Mar. 2019 [171] © 2019 IEEE

and extraction which is bounded by recombination at an interface and/or in the depletion region. In contrast, a non-uniform change in the EQE might indicate non-radiative losses and a reduction in the minority carrier diffusion length, depending on the shape of the reduction observed.

At the higher temperature of the Martian orbit conditions, where no inflection point is observed in the J-V data, a reduction in the EQE is also observed, further suggesting inhibition of minority carrier extraction at a non-ideal interface as the depletion width is insignificant at V_{mp}. Here, the band offset at the CIGS/CdS interface will limit the minority carrier transport.

4.2.5 Radiation and Self-Healing results

To further investigate this system for use in the high-radiation environment around Jupiter, a radiation dependent study was performed on a set of samples, where devices were exposed to 1.5 MeV protons at a number of different fluences (1×10^{14} cm^{-2}, 1×10^{15} cm^{-2}, 1×10^{16} cm^{-2}, and 5×10^{16} cm^{-2}). The dark and light J-V curves taken at standard conditions after exposure are plotted in Figure 4.10, where an increase in dark current, and decrease in photovoltaic performance with increasing exposure compared to a reference is observed. Previous studies of the radiation tolerance of CIGS have been performed with various energies of both electrons and protons, though fluence levels investigated are generally less than studied here [11], [142], [144]. The degradation observed here is consistent with previous 1-MeV electron results, when considering the different damage coefficients of electrons vs protons [172]. When comparing 1-MeV proton results to previous studies [11], [144], only the 1×10^{14} cm^{-2} level can be compared (the highest fluence of previous studies), but appears consistent with those results as well. Above fluence levels of 1×10^{15} cm^{-2}, the devices no longer behave as diodes.

The fluences chosen here represent the maximum levels that might be experienced over a year in certain close orbits of Jupiter [20]. While the degradation observed here is readily apparent, it is consistent with previous results, and it should also be noted that this study was performed on un-encapsulated devices. Commercial photovoltaic arrays in space use additional layers of polymer or glass around the device to provide additional shielding to radiation. Therefore, even thin layers of encapsulation would improve the radiation tolerance of this system. Commercial encapsulated CIGS solar cells are currently under study.

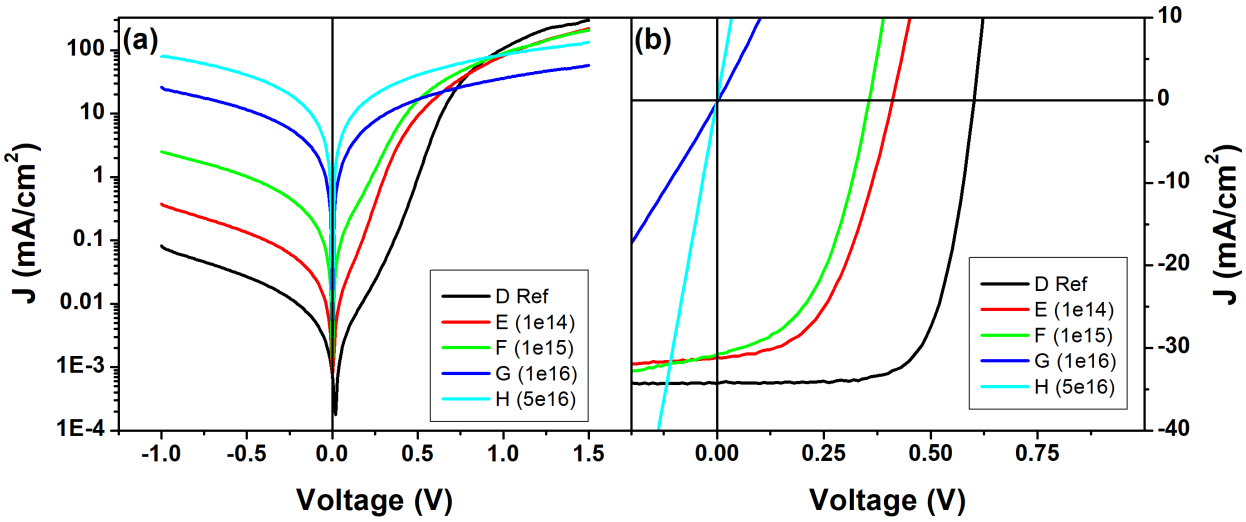

Figure 4.10: Comparison of (a) dark and (b) light J-V scans of CIGS solar cells with regard to proton fluence levels.

In addition to elevated radiation tolerance in comparison to more traditional space photovoltaics, the CIGS system has been observed to self-heal under heating effects from illumination [11], [143], [144], resulting in stabilized performance in LEO. This self-healing behavior was studied on the proton-irradiated samples, where the sample was held at 373 K for 12 h while under 1-sun AM0 illumination. During illumination, samples were held at the maximum power point (V_{mp}) to emulate operating conditions. This self-healing study was performed on all the irradiated samples, though only J-V scans for device F (1×10^{15} cm^{-2}) are shown here. J-V scans were taken initially, and every hour after, which are plotted in Figure 4.11 and obvious improvement is observed with increasing annealing time. While both V_{oc} and J_{sc} improve, V_{oc} is the main improvement observed, consistent with radiation exposure resulting in larger V_{oc} losses compared to J_{sc} (see Figure 4.10 (b)).

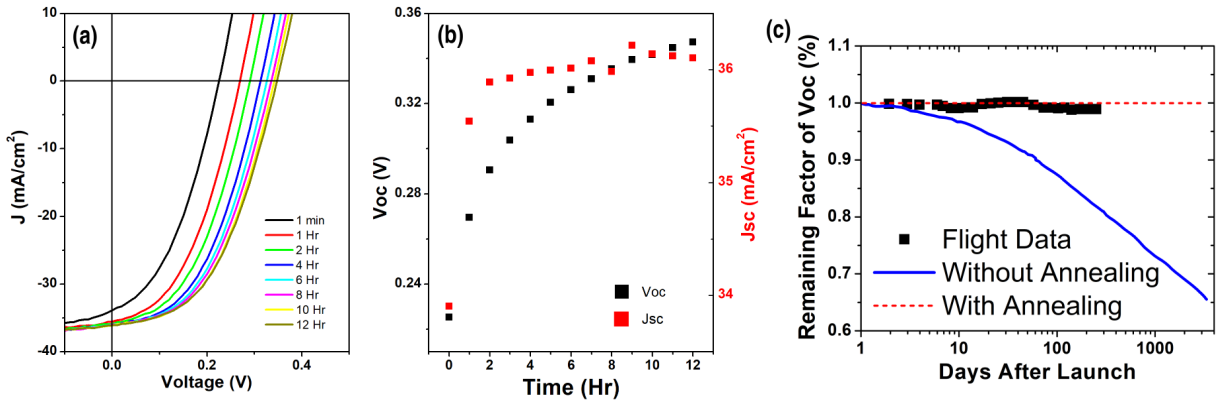

Figure 4.11: (a) J-V scans taken of proton irradiated CIGS solar cell (Sample F) during low thermal annealing under AM0 illumination as a function of time. (b) V_{oc} and J_{sc} extracted from previous J-V scans. (c) An comparison of V_{oc} degradation of a CIGS solar cell with and without annealing effects, and LEO flight data. Panel (c) Reproduced using data from [144]

This increase in the extracted solar cell parameters is highlighted in Figure 4.11 (b), where the J_{sc} stabilizes after an initial jump, and the V_{oc} increases over the time range investigated. This increase in V_{oc} suggests that recombination centers produced during particle bombardment are then passivated by reordering of the material at elevated temperatures. This self-healing behavior offers potential for stabilized performance on orbit (as seen in Figure 4.11 (c)) or recovery of performance during and after transit. Here, a high annealing temperature was selected in order to observe this effect, though it is known that the recovery effect is temperature dependent [143]. Thus, under LILT conditions, this effect will likely be small, though it may prove important to maintain performance during transit.

4.3 Conclusion

Commercial grade flexible CIGS solar cells have been studied for space power generation under LILT conditions. PL results showed evidence of carriers localized at defects, though features suggest defects are shallow and do not appear to significantly alter performance under standard operating conditions. Stability under thermal cycling was observed, though intense heat (>300 °C) will result in formation of barriers at interfaces that will reduce performance. A loss in performance (mainly FF) is observed when comparing the light soaked (LS) state to the relaxed (R) state under LILT conditions, though this effect is relatively small. No LILT effect in the photovoltaic regime was observed, though a similar effect was seen in the forward bias region while in the relaxed state and under orbital conditions of Saturn and Jupiter, suggesting a temperature and intensity dependent barrier to majority current may be present. As will be discussed in the next chapter, barriers like this may be mediated by thermionic emission, and thus limit current flow according to the temperature dependent thermionic emission rate. The mechanism behind this inflection point at forward bias is still under investigation.

Under proton irradiation consistent with maximum 1 year levels at Jupiter, unencapsulated CIGS solar cells exhibit significant degradation, though commercial cells would suffer less degradation in more mission-likely conditions. Finally, self-healing and reduction of recombination centers was observed when annealing proton-irradiated devices at 373 K under illumination, providing a pathway for stabilized on orbit photovoltaic performance.

Chapter 5

High-Stability Perovskite Solar Cells Studied under Low-Intensity-Low-Temperature Conditions

Solar cells based on halide perovskites have seen a rapid increase in photovoltaic power conversion efficiency over a relatively short timespan. This meteoric rise in performance to the current maximum of 25.2% has captured the attention of the photovoltaic community, due to many favorable photovoltaic parameters [8]. These ABX_3 structured materials are composed of Earth-rich elements, and are compatible with solution process manufacturing, promising the potential for low cost fabrication. Perovskite solar cells also have shown strong absorption coefficients, defect tolerance, and long carrier lifetimes [173].

Methylammonium lead iodide based perovskite solar cells (PSC) have been among the earliest and best performing devices, but the flexibility of the perovskite system has meant that many are turning to more complex compositions to solve some of the problems that PSCs face, such as thermal and moisture stability. The perovskite structure allows for alloying of the constituents at each lattice site, thereby adjusting the physical and electrical parameters. The adjustment and alloying of the anion and cation can result in adjustments to the band gap, and increased environmental stability. This adjustment of the band gap can result in a better match to the solar spectrum, or even realization of tandem devices based on PSCs. Triple A-site cation devices where formamidinium (FA), methylammonium (MA), and inorganic caesium (Cs) are alloyed together have provided devices with high efficiencies and *relative* long term stability [174], [175]. This combination will hereafter be refereed to as FAMACs, in reference to the three cations, though this device also had alloying of the anion iodide

with bromide to retain structural stability, with a full composition of $(FA_{0.79}MA_{0.16}Cs_{0.05})_{0.97}$ $Pb(I_{0.84}Br_{0.16})_{2.97}$. With this composition, and adjustment of interfaces and contact layers, Christians *et al.* demonstrated >90% of initial efficiency after 1000 hrs of operation in ambient conditions.

Research into space application of PSCs is now underway, as they have shown to be relatively radiation tolerant, similar to other thin film solar cells [11], [142], [176]–[179]. Their solution processable nature also means compatibility with flexible substrates, which can lead to light weight (high specific power) solar arrays [180], [181]. This radiation tolerance, and the possibility for low-weight low-cost high performance solar arrays mean that PSCs have great potential as options for CubeSat and SmallSat missions [182]–[184]. In this chapter, FAMACs based solar cells are studied under conditions equivalent to those around Mars, Jupiter, and Saturn, and results show potential application under these challenging conditions.

This chapter is based on Brown et al.'s paper published in *ACS Applied Energy Materials*, vol. 2, no. 1, pp. 814-821, 2019.

5.1 Experimental Details

The solar cells under investigation here were produced in the superstrate configuration by Dr. Giles Eperon, and detailed information on the preparation can be found in the supporting information of [185]. An SEM micrograph of one of the devices is shown in Figure 5.1 (a), with the various layers visible. As the solar cell was produced in the superstrate configuration, a sample holder was produced to provide adequate mechanical, thermal and electrical contact to the devices, and is shown in Figure 5.1 (c). Additionally, as described in Chapter 2,

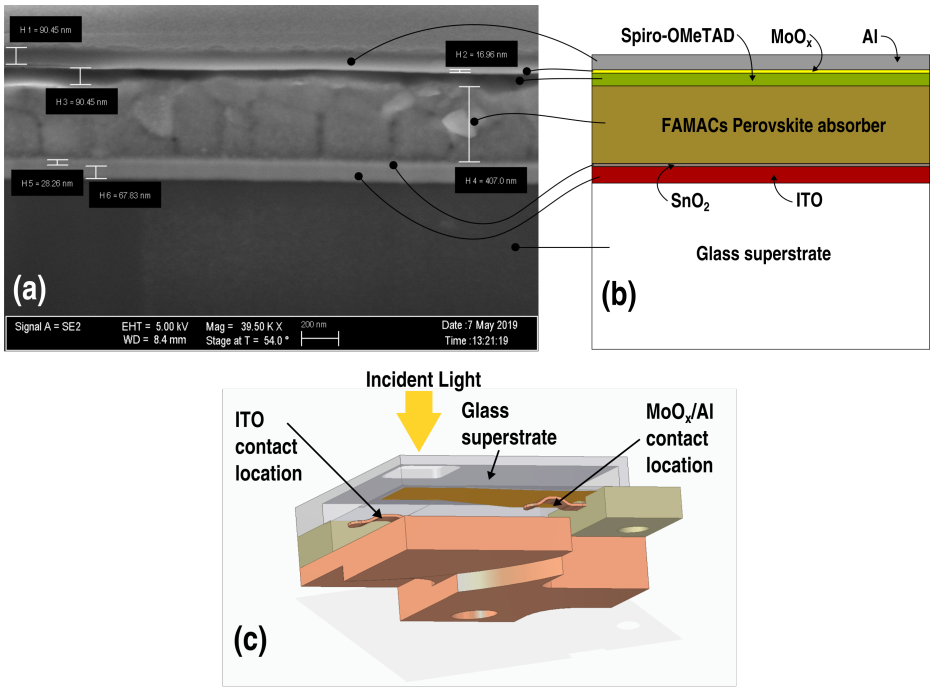

Figure 5.1: (a) SEM cross sectional micrograph of perovskite solar cell with thicknesses of various layers labeled (Acknowledgment: Jesse Aragon De Galvez). (b) Schematic of perovskite solar cell studied in this chapter. (c) Cutaway view of spring contact sample holder used to hold superstrate perovskite solar cells in cryostat.

the cryostat was modified to allow for vacuum pumping. This cryostat was loaded from inside a nitrogen filled glove box, and then the cryostat was transported to the lab while closed, allowing the samples to be kept from exposure to atmosphere. Temperature and bias dependent J-V, EQE and PL were performed according to the setups outlined in Chapter 2. For the photoluminescence experiments detailed in this chapter, the pump laser (632.8 nm HeNe laser) was not focused and allowed to cover the entire device, to both allow for simultaneous PL and J-V experiments, and to prevent degradation that might result from

intense local heating of the perovskite solar cell. Here, J-V scans are taken from both reverse bias to forward bias (forward) and from forward bias to reverse bias (reverse), as an indicator of the quality of the material, as will be discussed below.

5.2 Experimental Results and Discussion

5.2.1 Photoluminescence Spectroscopy

The temperature dependent photoluminescence spectra of one of the FAMACs solar cells, and associated extracted parameters are shown in Figure 5.2. The intensity of the PL is seen to decrease with increasing temperature, with a rapid decrease in PL intensity seen above 175 K. The mechanism behind this rapid decrease in PL intensity is most likely due to the ionization of the exciton binding energy at higher temperatures in the FAMACs, with an additional effect coming from an unintentional barrier to minority electron extraction in these specific structures. To quantitatively assess the mechanism behind the temperature dependent quenching of the PL, the natural log of the integrated intensity is plotted vs. inverse temperature in an Arrhenius plot (Figure 5.2 (c)), and is fit to extract an activation energy. This activation energy can be thought of as the mechanism responsible for quenching of radiative recombination, typically associated with the exciton binding energy. Here, the rather high value of $E_B \sim 33$ meV supports the strong luminescence, which persists to higher temperatures. However, this value is larger than values typically extracted from other common MA and FA based perovskite systems [186]. The temperature dependent PL shows a rapid decrease in intensity around 150 K corresponding to a thermal energy (k_BT) of ~ 15 meV, and the intensity stabilizes between 150 and 300 K. As discussed later

in this chapter, this large exciton binding energy and stabilization of the PL at higher temperatures is linked to an unintentional barrier at the FAMACs/SnO_2 interface. This barrier is temperature and intensity dependent, inhibits minority electron transport, and facilitates radiative recombination under some conditions. Therefore, the true exciton binding energy E_B, as discussed later, is more likely 15-20 meV, consistent with results from other mixed-cation perovskite studies [187], [188].

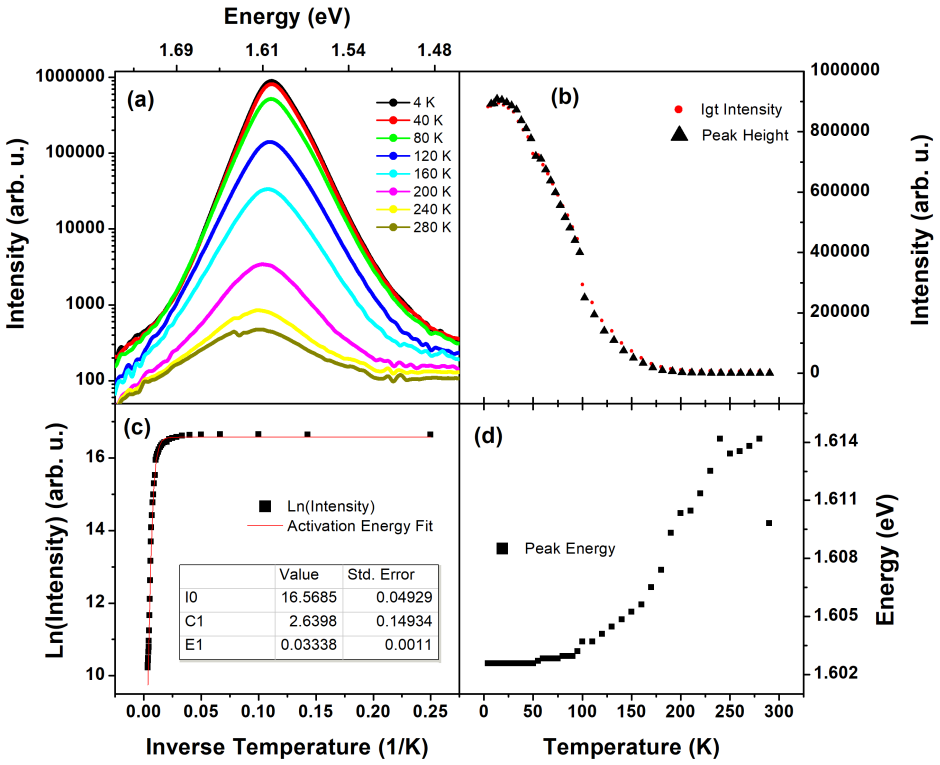

Figure 5.2: (a) Selection of temperature dependent PL spectra of FAMACs based perovskite solar cell. Plotted on a log scale. (b) Integrated intensity and peak height of the PL vs temperature. (c) Arrhenius plot of integrated PL intensity vs inverse temperature with associated fit and extracted parameters. (d) Peak energy of PL vs temperature.

The PL energy vs temperature is shown in Figure 5.2 (d), where an increase in PL energy from $\sim$ 1.60 eV at 4.2 K to $\sim$ 1.65 eV at 300 K is observed. This blue shift in the PL position with increasing temperature is contrary to the behavior of the band gap of traditional semiconductors [25], but is seen in perovskite systems and is understood to be related to the band inversion symmetry (doubly degenerate p-like conduction bands and s-like valence bands), that is typical in these systems [189].

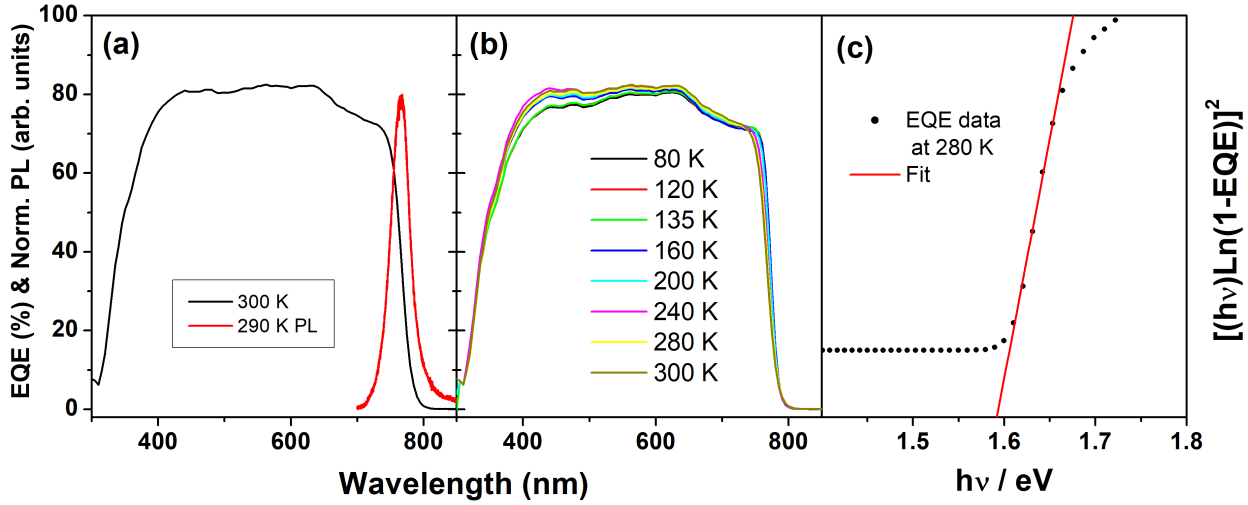

Figure 5.3: (a) Comparison of EQE and PL of a perovskite solar cell. Similar agreement is found at lower temperatures. (b) Temperature dependent EQE of perovskite solar cell. (c) Associated Tauc plot analysis for extraction of band gap energy.

External quantum efficiency of a FAMACs solar cell is taken between 77 K and room temperature, and is plotted in Figure 5.3 (a). A slight reduction in the EQE is seen with decreasing temperature, particularly toward the blue region, corresponding to the front of the device. This reduction in EQE and increasing in PL with decreasing temperature indicates a correlation between the mechanisms responsible for the collection and the emission. Only

a slight shift is seen with temperature in the absorption edge, and this shift is analyzed further with Tauc analysis as seen in Figure 5.3 (b). The energy extracted from this analysis is plotted as stars in Figure 5.4 (a), where close agreement between the EQE and PL is observed. This agreement indicates that the PL from these FAMACs devices originates from band to band transitions, and/or that any excitonic effects fall within the line width of the free carrier recombination observed.

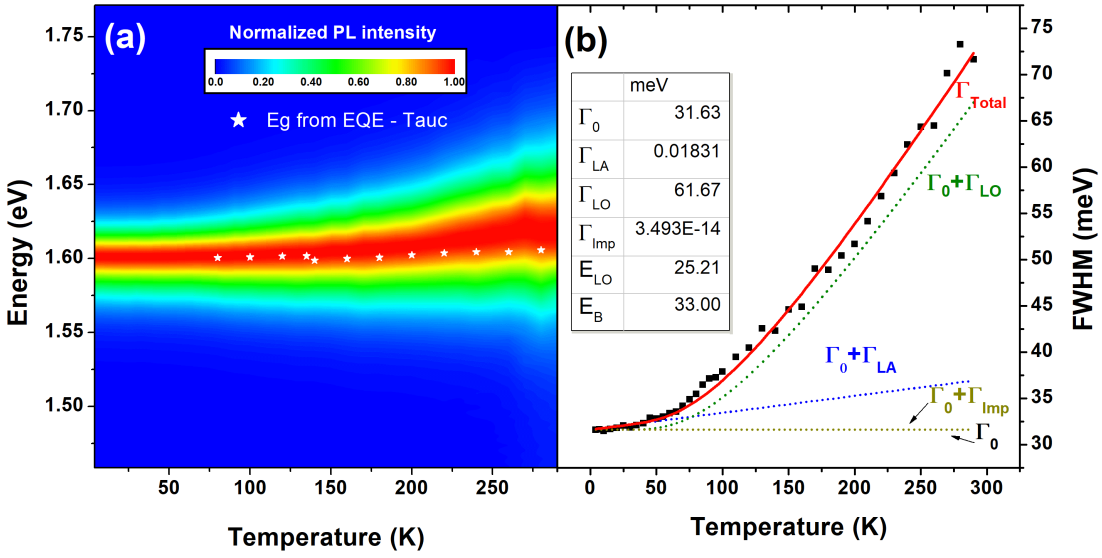

Figure 5.4: (a) Normalized temperature dependent PL energy and intensity plotted vs temperature. Stars represent the band gap energy extracted from the EQE via Tauc analysis. (b) FWHM of the PL plotted vs temperature, with associated line width broadening fits and extracted parameters.

Figure 5.4 (a) shows a 3D plot of PL intensity and energy vs temperature, where a slight blue shift and widening of the spectra is observed. Also clear in figure 5.4 (a) is the absence of any concrete evidence of a structural phase change, which typically manifests as a large shift

in the PL energy, in comparison to evidence observed in $MAPbI_3$ and $FAPbI_3$ perovskites [190], [191]. These structural phase changes result in transitions in the crystal symmetry, for example, $MAPbI_3$ transitions from cubic to tetragonal at $\sim$ 330 K, and from tetragonal to orthorhombic at $\sim$ 160 K [192]. In this study, the FAMACs based perovskite solar cell persists in the cubic phase and remains structurally uniform at all temperatures investigated, supporting the stability of this system. In addition, no evidence of alloy fluctuations in the low temperature PL is observed, as is the case in $MAPbI_3$ [189], [193]. Further evidence for the stability of this system is seen in the unchanging nature after multiple thermal cycling events from the different experiments performed. This thermal stability is an important factor in the potential application of this material for space missions.

While no excitonic features are directly observed in the PL, subtle features related to carrier localization and/or excitons are noticeable in both the 's-shape' in the intensity dependence at low temperature and stable high temperature PL, shown in Figure 5.2 (b). Along with the binding energy extraction outlined earlier, further analysis of the PL was performed to investigate the broadening parameters for the PL collected from this device, and gain more information about the material quality. The width of the PL peak at half-maximum (FWHM) vs temperature is plotted in Figure 5.4 (b) as the black squares, and is fit with the following equation:

$$\Gamma_{tot} = \Gamma_0 + \Gamma_{imp} + \Gamma_{acoustic} + \Gamma_{optical} \tag{5.1}$$

Γ_0 is the temperature independent inhomogeneous line width, $\Gamma_{imp} = \gamma_{imp} e^{(-E_a)/k_B T}$ is related to extrinsic or Urbach mechanisms due to non-idealities in the system such as impurities, alloy fluctuations, and/or defect related transitions. The $\Gamma_{acoustic} = \gamma_{acoustic} T$ term is linked to carrier interactions with acoustic phonons, while $\Gamma_{optical} = \frac{\gamma_{optical}}{e^{(-E_a)/k_B T} - 1}$ is related to optical

phonons mediated by Fröhlich interactions, which dominate in polar semiconductors at elevated temperatures[194].

The dotted lines in Figure 5.4 (b) show the temperature dependences of the different broadening mechanisms, and the solid red line shows the combination of those mechanisms resulting in the fit. At low temperature, longitudinal acoustic (LA) phonons and other mechanisms dominate the broadening. Above 50-70 K, the longitudinal optical (LO) phonon processes become the dominant broadening mechanism, which is expected because of the strongly polar nature of this semiconductor, and has been shown to monopolize spectral broadening in several perovskite systems [189], [195].

The Γ_0 term at 4.2 K gives $\sim$ 31 meV, which is considered essentially the PL line width at 0 K, and is related to inherent nonidealities and compositional disorder in the system. Contributions from the Γ_{imp} term are close to zero, illustrating that broadening due impurities, defects, or other nonidealities and the effects thereof are inconsequential in this case. Thus phonon-moderated processes command the majority of the PL broadening [189], and electron-LO phonon interactions dominate at the temperatures ($>$ 50 K) important to this study. This is consistent with other more mature and well studied systems perovskite systems such as $MAPbI_3$ and $FAPbI_3$.

5.2.2 Current-Density Voltage results

The photovoltaic region of the J-V characteristic is shown in Figure 5.5 for (a) 300 K under 1 sun AM0 and for (b) LILT conditions at Mars (263 K under 0.43 $\times$ AM0). These J-V curves exhibit hysteresis between the forward and reverse J-V scans, which is a well known phenomena in PSCs, and has been attributed to ionic motion of different species in the

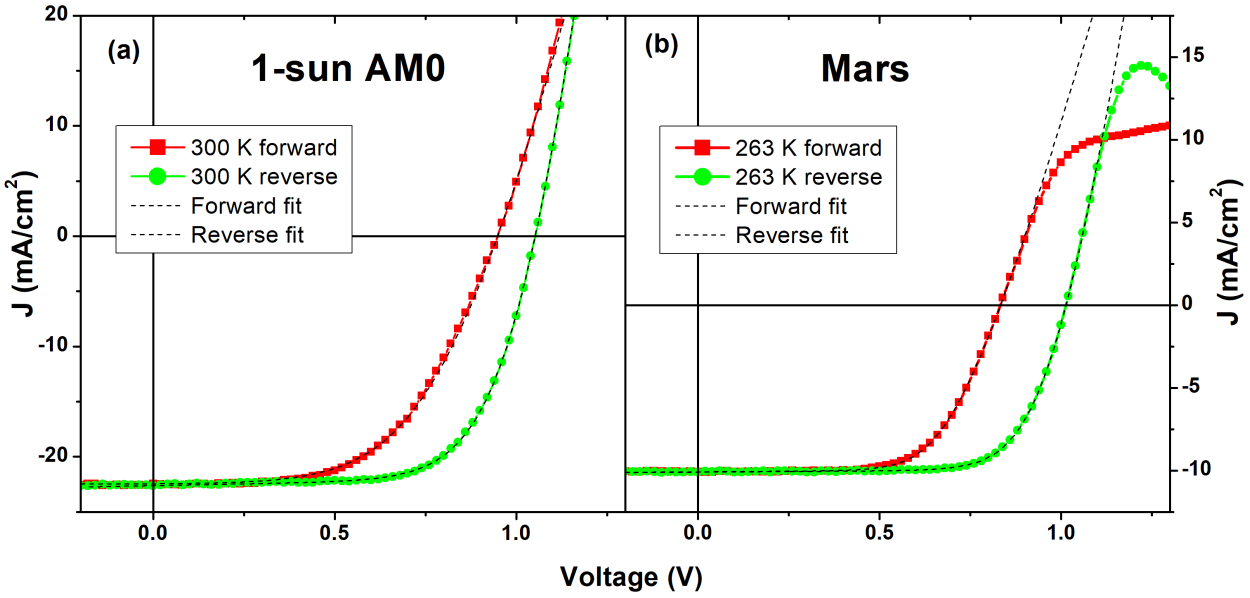

Figure 5.5: Forward and Reverse J-V characteristics of FAMACs absorber solar cell at (a) 300 K at 1 sun AM0 and (b) 263 K at 0.43 × AM0, respectively.

absorber, lithium diffusion from the spiro-OMeTAD, and/or charging and discharging of certain interfaces in the solar cell structure [196]–[198]. Degradation during storage and transit [199] between the partner laboratories is the likely reason behind the size of the hysteresis and the relatively low ($\sim 10 \pm 2\%$) PCE of the devices described here.

Measurements prior to shipment (from Golden, CO to Norman, OK) showed little hysteresis and better PCE ($\sim 15.3 \pm 0.9\%$), thus partial breakdown of the absorber and increase in defect population during transit may have been responsible for the increase in hysteresis [200]. After this initial degradation during transit, the samples remained relatively stable during measurement in the cryostat and storage in the nitrogen filled glovebox. While this loss in performance was inadvertent, we consider this deterioration an interesting method

to assess unavoidable degradation comparable to that which might occur while in transit through space to the mission location [199].

J-V data taken under LILT conditions equivalent to Martian orbit are shown in Figure 5.5 (b), which also (like 300 K under AM0) show hysteresis between the forward and reverse scans. Additionally, evidence of a barrier to majority current flow is observed in the forward bias regime ($V > V_{oc}$) of both J-V scans. The extreme roll-over behavior of the reverse scan (green circles) also indicates negative differential resistance and tunneling effects in the higher forward bias regime. These data suggest that majority current flow is likely limited by thermionic emission across the *unintentional* barrier discussed above, and the rate of this emission is dependent on the thermal energy ($k_B T$) of the carriers and the barrier height. While evidence of this barrier is observed, radiative recombination is still prevalent in the system as seen in the PL, indicating good material quality.

As the temperature and intensity conditions are adjusted to be representative of Jupiter (Figure 5.6 (a)) and Saturn orbits (Figure 5.6 (c)), hysteresis is removed and the forward and reverse scans are comparable. At these lower temperatures, the motion of ionic species in the absorber and other layers appear to "freeze out", as observed by others in PSCs [186], [191], [201]. This increased stability at lower temperatures, along with the stable cubic phase seen in the PL results, highlights the potential of these systems for use in LILT environments. With regard to the photovoltaic performance under these LILT conditions, a reduction in J_{sc} and V_{oc} is observed. This is consistent with the reduced light intensity at the specified conditions (Jupiter - 3.7% of AM0, Saturn - 1.1% of AM0), rather than effects of parasitic or nonradiative processes. Despite this reduction in V_{oc}, the extracted PCE ($\sim 11.1 \pm 0.05\%$) when adjusting for the reduced light intensity is similar to that achieved under standard

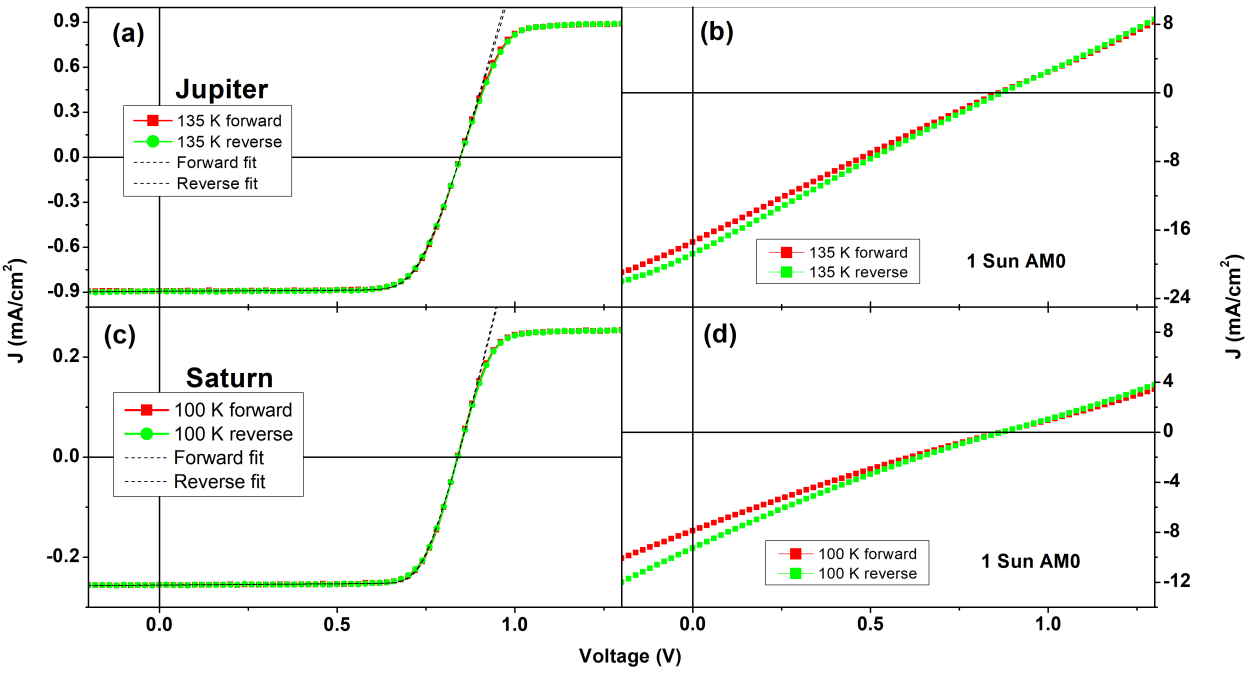

Figure 5.6: J-V scans for conditions representative of (a) Jupiter and (c) Saturn orbits, respectively. J-V scans taken under 1-sun AM0 illumination at temperatures consistent with (b) Jupiter (135 K) and (d) Saturn (100 K).

conditions at room temperatures ($\sim$ 11%). This retention of the PCE with the drop in V_{oc} is due to the increase in fill factor as compared to the room temperature measurements. A simple single diode model [40] is fit to the reverse J-V data to extract the fill factor, which gives $\sim$ 66% at 300 K under 1-sun AM0, $\sim$ 72% for Martian orbit conditions, $\sim$ 75% for Jupiter orbit conditions, and $\sim$ 77% for Saturn orbit conditions, respectively. Despite the initial degradation seen in these devices due to transit, the preservation of the PCE under LILT conditions appears promising, and implies that any damage to the solar cell structure that might occur while traveling to the mission location may be inconsequential once under LILT conditions.

Similar to the J-V characteristic taken under Martian orbit conditions, the J-V scans shown in Figure 5.6 (a and c) also show an increased barrier to majority current transport at forward bias, consistent with an increased effective barrier due to the low thermal energy ($k_{\mathrm{B}}T$ ~12 meV) of the photogenerated carriers. In comparison, a large reduction in fill factor is evident in the J-V scans in Figure 5.6 (b and d), taken under 1-sun AM0 illumination at 135 K, and 100 K, respectively. This reduction in fill factor also suggests the presence of an intensity and temperature dependent barrier, which obstructs high current flow (large photocurrent at high intensity, or at forward bias) at low temperatures. As discussed above in relation to the PL measurements, at lower temperatures both the current saturation at forward bias and the loss in fill factor under 1-sun AM0 illumination observed here is attributed to a parasitic barrier at the FAMACs/SnO_2 interface. While other interfaces, such at perovskite/spiro-OMeTAD [202], [203] and spiro-OMeTAD/MoO_x/Al [204], have shown similar nonideal contributions to early devices, here the reduction in the blue region of the EQE with temperature (Figure 5.3 (b)) and the behavior of the bias dependent EQE and PL (as discussed below) point to a barrier (likely the FAMACs/SnO_2 interface) at the top of the device.

A qualitative discussion of this behavior is pictorially represented in Figure 5.7, where the band structure for the ideal case (a), for the case including a parasitic Schottky barrier at the aforementioned interface at 0V (b), and including the same barrier at forward bias (c) are shown, respectively. With the addition of this barrier, at open-circuit conditions (Figure 5.7 (b)) the carriers that pass this barrier do so by thermionic emission. Therefore, at higher temperatures ($T > 263$ K), the effect of this barrier is minimal. However, at lower temperatures, the thermionic emission rate is reduced, and the thermal energy ($k_{\mathrm{B}}T$) of the

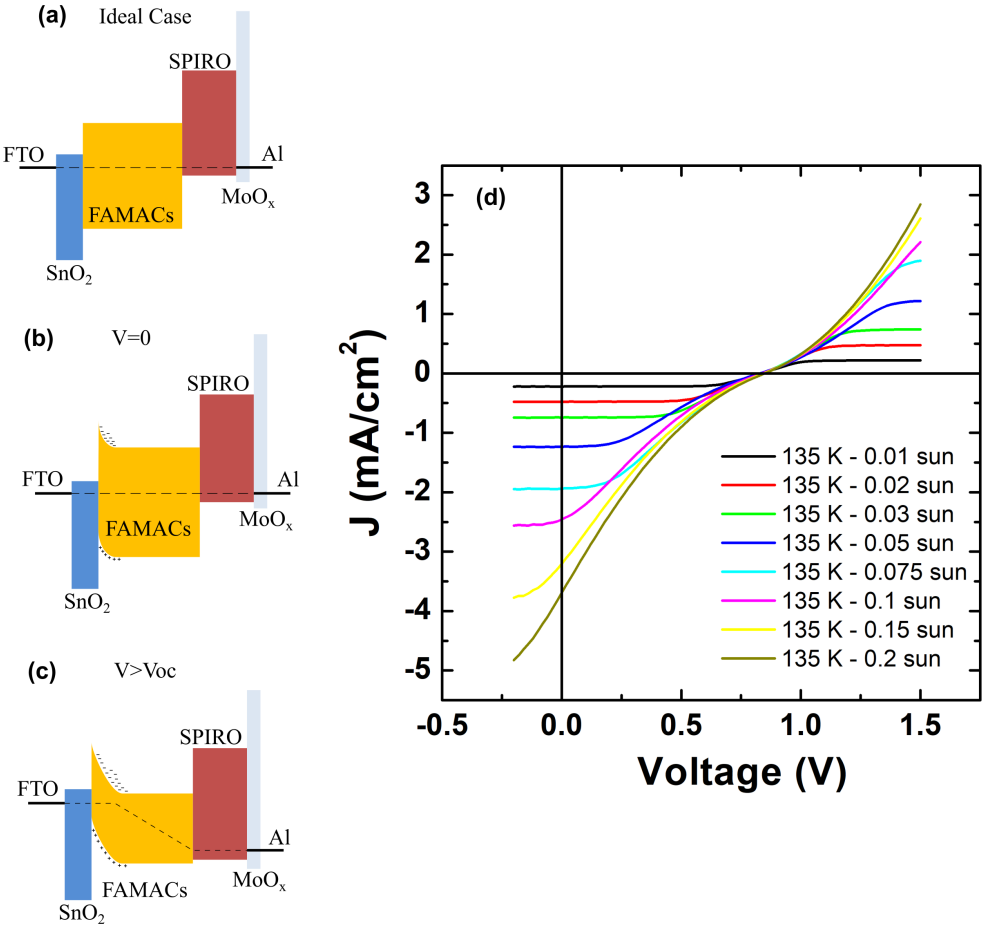

Figure 5.7: Schematic of band offsets of the device in the (a) ideal case, (b) at zero bias, and (c) at forward bias conditions. (d) Intensity dependent reverse J-V scans of a FAMACs perovskite solar cell. As intensity, and thus photocurrent, increases, the generated current cannot pass the barrier easily, and resistance increases.

carriers is diminished, which results in a more effective barrier to carrier transport. This parasitic barrier increases under forward bias conditions, as the Schottky barrier acts as a diode opposite in orientation to the main diode, and thus is essentially reverse biased. This

results in inhibited majority current flow at forward bias, and thus current saturation, as observed in Figure 5.6 (a and c).

This model of a Schottky barrier at the FAMACs/SnO_2 interface can also be used to understand the device behavior under illumination at different intensities. In addition to limiting the majority current flow, this barrier will also serve to limit the current flow that comes from the extraction of the photo generated (minority) electrons. At low temperature where the thermionic emission process is inefficient and the effective barrier height is largest, large photo generated current extraction is limited. If the photocurrent produced in the absorber exceeds the thermionic emission rate, minority electrons will see a large effective resistance at the interface of interest. This large resistance results in the reduction of fill factor in the light J-V curves at low temperature and 1-sun AM0 intensity, as seen in Figure 5.6 (b and d).

If the photogeneration rate (G_{r}) is lower than the thermionic emission rate (TE_{r}) for that temperature, for example at the low intensities in Figure 5.6 (a and c), then this large resistance is not observed and the fill factor recovers. Thus, advantageously for the current devices, much greater carrier extraction efficiency is achieved under low intensity at low temperature, as would be encountered on missions to Jupiter and Saturn. Indeed, the shift from $G_{\mathrm{r}} < TE_{\mathrm{r}}$ to $G_{\mathrm{r}} > TE_{\mathrm{r}}$, and associated increased resistance and loss in fill factor is seen in the intensity dependent J-V data taken at 135 K, shown in Figure 5.7 (d).

5.2.3 Bias Dependent EQE and PL

As described above, the applied bias can effectively modulate the size of this parasitic barrier at the SnO_2/FAMACs interface. Thus, bias dependent EQE and PL measurements were

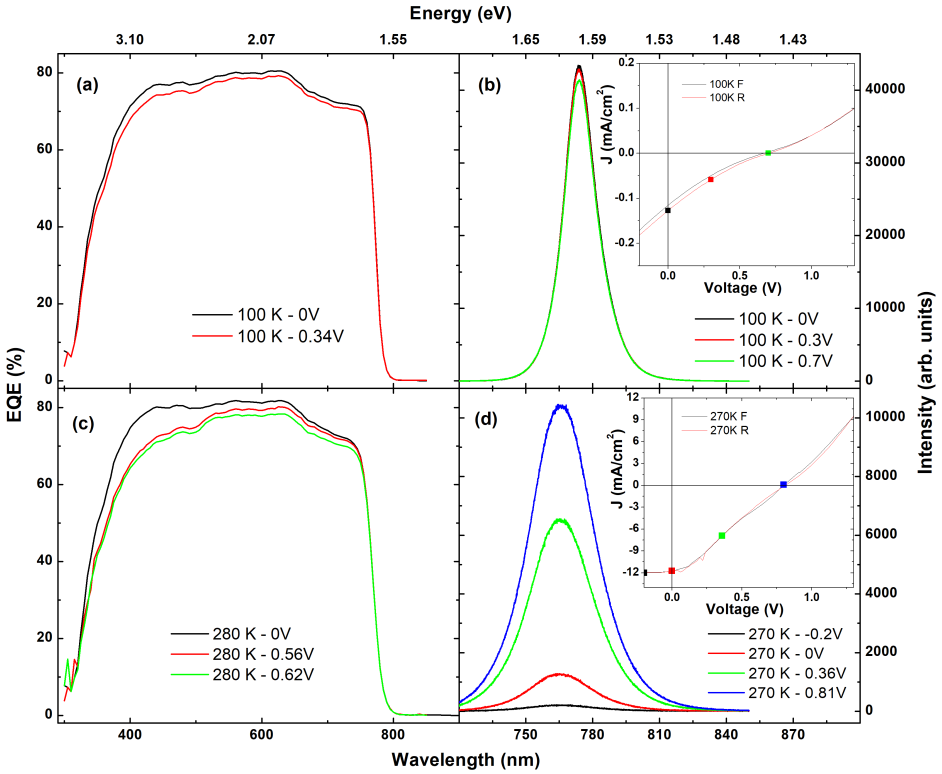

Figure 5.8: (a,c) EQE taken at short circuit and maximum power conditions, for 100 K and 280 K, respectively. (b,d) Bias dependent PL spectra acquired at 100 K and 270 K, respectively. The insets show the J-V characteristic taken under the monochromatic illumination conditions, and points plot the same biases as the relevant PL spectra. Reprinted (adapted) with permission from C. R. Brown *et al.*, "Potential of high-stability perovskite solar cells for low-intensity-low-temperature (LILT) outer planetary space missions," *ACS Applied Energy Materials*, vol. 2, no. 1, pp. 814–821, 2019. [Online]. Available: `https://doi.org/10.1021/acsaem.8b01882`. Copyright 2019 American Chemical Society

performed in order to further investigate this barrier on carrier collection and radiative recombination. The EQE at 100 K is shown in Figure 5.8 (a), at zero bias (J_{sc}) and at the max power bias for 1-sun AM0 illumination ($V_{mp} = 0.34$V). The predominant loss mechanism in the EQE appears to be reflectance due to the absence of an anti reflective coating (ARC). At the maximum power point, a slight reduction in the blue region of the device is observed, consistent with the location and postulated behavior of the FAMACs/SnO2 interface under forward bias. The increased barrier under forward bias serves to increase carrier recombination losses in the absorber, resulting in lower EQE.

Further evidence of this barrier and its role in increasing recombination is observed in the bias dependent radiative recombination (PL) at 100 K shown in Figure 5.8 (b). At this low temperature, the effective barrier is large, and the change in radiative efficiency observed with applied bias is small, reflecting the robust barrier to separation of charge carriers under these conditions. This barrier is also seen in the reduced fill factor of the J-V curve measured under the monochromatic excitation of the laser in the inset of Figure 5.8 (b).

As the temperature increases, the increased thermal energy and higher thermionic emission rate allow more electrons to bypass the barrier at the FAMACs/SnO_2 interface. Therefore, applied biases at higher temperatures should have a greater influence on the barrier height and the carrier transport. The EQE and *PL* at 270 K shown in Figure 5.8 (c and d) both show greater variability of signal with applied bias compared to the 100 K measurement. Indeed, at forward bias, a large reduction in the blue portion of the EQE indicates possible loss due to recombination, and the large increase in PL indicates that this recombination is likely radiative, and influenced by the increased carrier confinement of the barrier rather than the degradation of the perovskite absorber. While this barrier is problematic and introduces

losses for devices at AM0, the strong radiative recombination indicates the absorber retains quality, and under LILT conditions (especially Jupiter and Saturn orbits), FAMACs based solar cells appear to retain their high room temperature PCE.

5.3 Conclusion

FAMACs absorber based perovskite solar cells were studied under conditions relevant for deep space missions. The stability of this system was supported by absence of a clear phase transition in the temperature dependent PL and retention of crystalline cubic structure throughout the temperature range measured. Absence of hysteresis under LILT conditions gave further credence to the stability of this system under these extreme conditions. Strong photoluminescence was observed from 4.2 K to room temperature, with temperature quenching giving an exciton binding energy of $\sim$ 15-30 meV. A fit to the temperature dependent line width indicated that electron-LO phonon processes dominate the thermal broadening of the system. Evidence of an unintentional and parasitic barrier is observed in bias dependent measurements of PL and EQE, as well as in temperature dependent EQE and J-V measurements, suggesting that some portion of the binding energy may be due to carrier localization at an unintentional barrier at the FAMACs/SnO_2 interface. while this barrier limits photovoltaic performance under 1-sun AM0 conditions at high and low temperatures, it appears to have little effect under low temperature *and* low intensity conditions (LILT). This is likely due to the decreased minority carrier generation rate which is less than the thermionic emission rate that determines carrier extraction over the barrier. Along with their stability as evidenced by the PL, these devices retain high performance under LILT conditions, despite degradation during transit

and unintentional barrier formation. Despite these promising results, increased recombination losses undoubtedly limit the V_{oc} and assessment of pristine devices under LILT conditions is require to determine the optimum performance in these challenging environments. Such measurements are currently underway, along with proton irradiation of devices under LILT environments.

Chapter 6

Study of type-II InP/InAlAs Quantum Well Solar Cells

Similar to other studies here, InP based solar cells have shown advantages in weight savings and in radiation tolerance compared to silicon and GaAs photovoltaics [205]. Additionally, some studies have shown increased radiation tolerance when including quantum confinement structures like quantum dots or quantum wells [124], [206]–[208]. type-II InP/InAlAs Quantum Well (QW) solar cell devices are investigated here using J-V, EQE, PL and PR. This system was chosen for it simplicity, and to also investigate hot carrier effects in type-II QW systems, which have shown remarkable effects in various studies [105], [209]–[212]. In the scope of this work, the hot carrier effects will not be covered, due to a number of factors.

6.1 Experimental Methods

Two sample structures were investigated here (plotted in Figure 6.1), one with a single quantum well, and one with five quantum wells. The structures grown were by metal-organic vapor phase epitaxy (MOVPE) at NanoPower Research Labs in a NIP device structure to provide an electric field to help extract photogenerated minority carriers. InAlAs layers were grown at a composition lattice matched to the InP. The n and p layers were doped at 8.4×10^{17} cm^{-3} and 9.6×10^{17} cm^{-3}, respectively. The layer beneath the quantum well was adjusted so that both structures have the same amount of i-InAlAs in the active layer. An InP capping layer was used to prevent oxidation of the InAlAs layers in atmosphere. The majority of the initial studies presented here are limited to the single quantum well structure, due to the relative simplicity of this device.

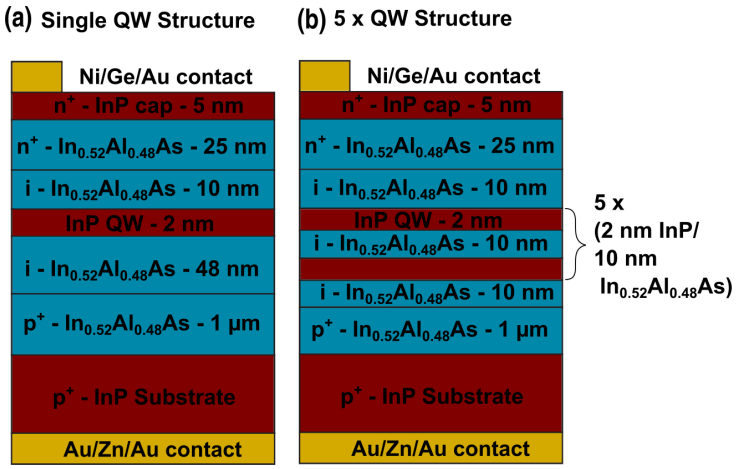

Figure 6.1: Sample schematic for the QW solar cell devices studied here. (a) Single QW structure. (b) 5 QW structure.

In cases where the InP cap was removed to investigate deeper layers, an etch selective to InP over InAlAs was used. The etch formula used was a 1:1:2:10 mixture of hydrochloric acid, phosphoric acid, acetic acid, and water, respectively.

PL, J-V, EQE, and PR measurements were performed as described in Chapter 2, where the excitation wavelength used for PL and PR was 632.8 nm.

6.2 Experimental Results and Discussion

6.2.1 Temperature Dependent Photoluminescence

Figure 6.2 (a) shows the spectra acquired from the single QW sample at various temperatures. These spectra display numerous features, which shift and broaden with temperature. The highest energy feature corresponds to the InAlAs barriers (P1), which initially shifts to higher energy indicating some localization, followed by a conventional redshift behavior at higher

temperature [25]. Other lower energy features (P2 and P3) are related to the InP QW and/or interfaces between the InP and the InAlAs, and will be discussed further below. Assignment of these features is non-trivial since the main peak lies below the expected band gap energy of bulk (direct) InP, as can be seen when comparing the peak position to the dotted line corresponding to InP. Moreover, quantum confinement in the InP QW should lead to states that increase the emission energy, as shown by the E1 and E2 states that were calculated for this QW structure.

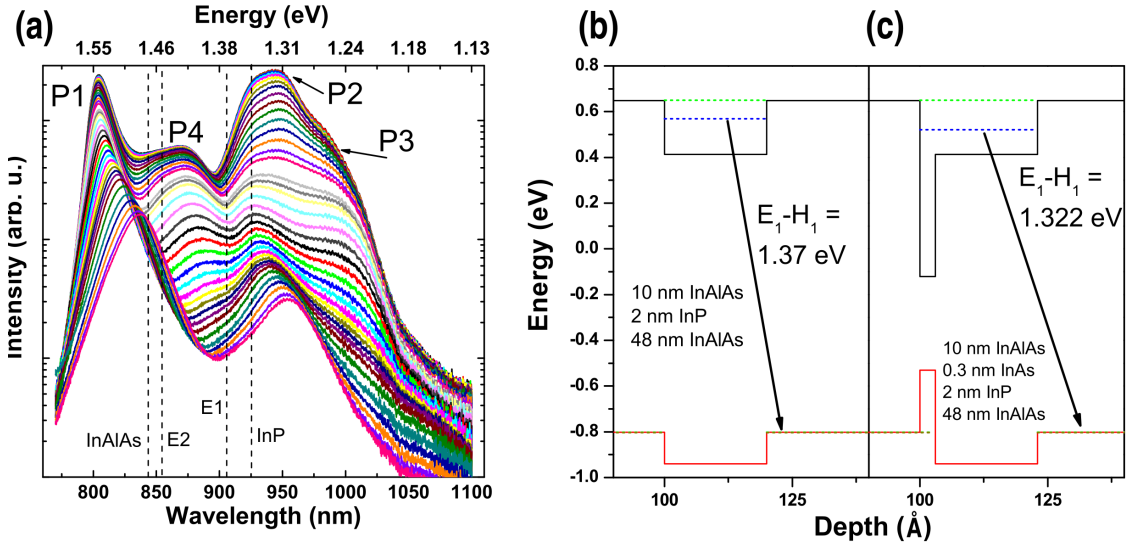

Figure 6.2: (a) Temperature dependent PL spectra from 4.2 K to 295 K of a single QW sample with the InP cap removed. Dotted lines show approximate transition energies at 295 K for InAlAs, InP, and the first two transitions of an InP/InAlAs QW calculated by NRL Multibands [213], corresponding to (b). (b) Band diagram and calculated energies of an InP/InAlAs QW. (c) Band diagram and calculated energies of an InP/InAlAs QW, with an additional 0.3 nm InAs layer at one of the interfaces.

This discrepancy is most likely resolved when accounting for additional layers that unavoidably form at the InP/InAlAs interfaces in the material [214]–[217]. As InP and InAlAs do not share cation or anion, (even at a perfect interface) an unintentional layer of InAlP and/or InAs will form, which depends upon the growth direction [217]. Modeling of the QW structure at 300 K was performed with $k \cdot p$ calculation using NRL Multibands [213], which shows in Figure 6.2 (b) that even a thin layer of InAs significantly affects the QW transition energies. As the QW thickness used in this structure is small (2 nm), even a single monolayer of InAs has an appreciable relative thickness in comparison, and provides additional confinement for both holes and electrons in this structure [217]. More evidence for this additional (type-I) offset is provided in the temperature dependence of the PL. Most type-II systems have limited luminescence at higher temperatures, since carriers are spatially separated, and thus the recombination efficiency is poor. In these samples, significant luminescence is present even at room temperature, indicating structures that contribute to carrier localization even at higher temperatures. Therefore, the lowest energy feature (P3), a shoulder or additional peak in the temperature dependence PL, is likely related to the type-II InP/InAlAs interfaces. As the cap, well, and substrate are InP, and the barrier material is InAlAs, these interfaces are *not only* located at the QW, but are throughout the entire device, and likely contribute to the radiative recombination. A feature in between the two main peaks is also visible (P4), though this feature does not appear in other measurements, and is not focused on here.

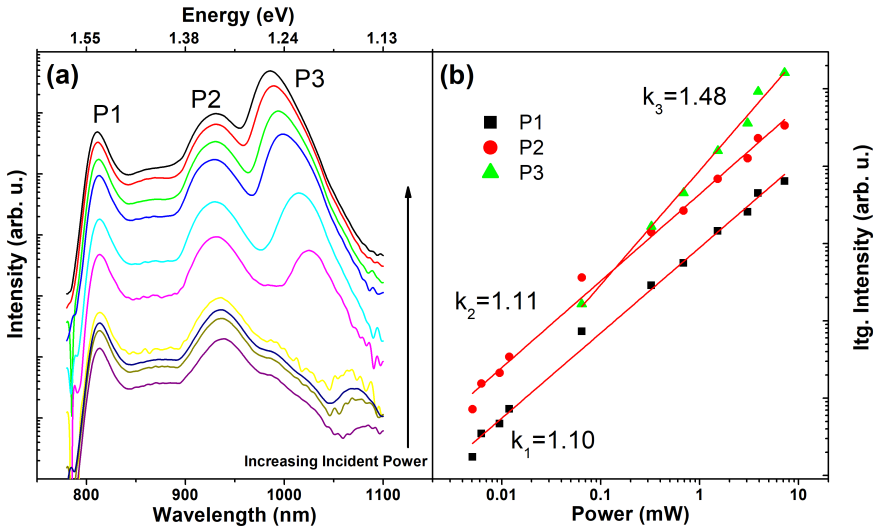

Figure 6.3: (a) Excitation power dependent PL spectra of a single InP/InAlAs QW sample, with the InP cap removed. Features are labeled as P1, P2, and P3, with P3 showing a significant blueshift with increasing power. (b) Integrated intensity of the Gaussians fitted to each feature plotted with respect to incident power on a log-log plot. Linear fits to the intensity dependence give the extracted k parameters displayed in the table.

6.2.2 Excitation Power Dependent Photoluminescence

Excitation power dependence measurements (plotted in Figure 6.3 (a)) were performed on a sample which had the InP cap removed, in order to better understand the nature of the features observed in the PL. The lowest energy feature (P3) shows a significant shift in energy with increasing power, as well as an increase in relative intensity as compared to the other features/transitions. The PL spectra is fitted with multiple Gaussians to assess the behavior of. The integrated intensity extracted is plotted in a log-log plot in Figure 6.3 (b). Each feature is fitted to a power law, as outlined in Chapter 2, where the extracted k-parameter is

indicative of the recombination mechanism. For all three peaks, the extracted parameter is greater than one, indicating either excitonic or band-to-band recombination, rather than any defect related recombination. P1 and P2 both display very similar behavior to each other (k = 1.103 and k = 1.122, respectively), while P3 has a larger slope (k = 1.476), suggesting a difference in the recombination for this process. Additionally, only the lowest energy peak shows a significant shift in energy with power.

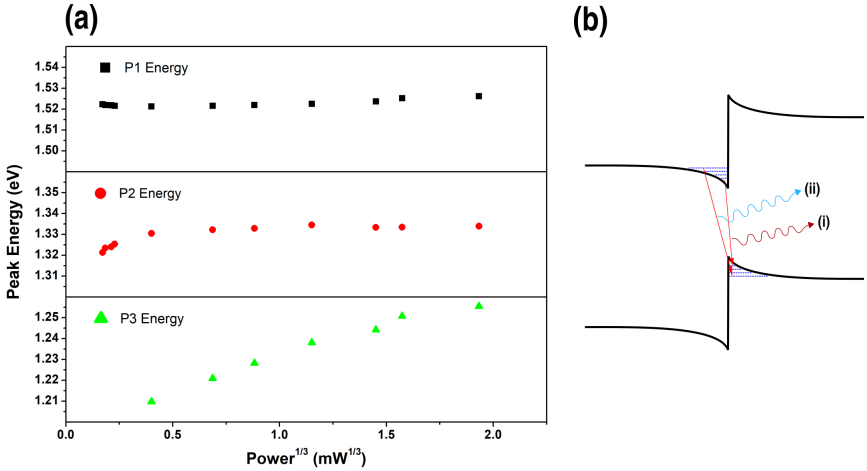

Figure 6.4: (a) Peak energy position of each Gaussian fitted to the features in Figure 6.3 (a), plotted with respect to incident power. All three panels are plotted over the same range (60 meV), showing a significant shift in the energy of Peak 3. (b) Schematic illustration of the triangular wells that form due to the band bending at type-II interfaces. Increasing excitation power results in state filling in these wells, and a resulting blueshift in the energy of the PL.

The peak energy position of each Gaussian is plotted with respect to power$^{1/3}$ in Figure 6.4 (a). Here, each panel is plotted over the same range (60 meV), where the lowest energy peak shows a considerable shift, and the first two peaks show little change in com-

parison. In addition, when this shift is plotted with respect to power$^{1/3}$, a linear behavior is observed, which has been associated with type-II recombination [218], [219]. The generally accepted mechanism behind this blueshift with power is schematically illustrated in the inset (Figure 6.4 (b)), where band bending at bulk interfaces produces triangular wells for carriers. As incident power increases, the photogenerated carriers begin to fill the lower states in these wells, and the emission shifts to higher energy. A slight decrease in energy at the lowest powers is also evident for the second peak. These data confirm P1 and P2 are direct recombination mechanisms, while P3 is related to a type-II transition at InAlAs/InP interfaces in this structure where quantum confinement does not exist to raise the energy.

6.2.3 Temperature Dependent Photoreflectance

To further investigate the various transitions in these samples, temperature dependent photoreflectance was performed on both the single quantum well, and the 5 quantum well sample. Waterfall plots of the photoreflectance for the single quantum well and the 5 quantum well sample are shown in Figure 6.5 (b) and (c) respectively. A comparison of the PL and PR of the single QW sample at 77 K is shown in Figure 6.5 (c), where good correlation between features from the different measurements is observed. Photoreflectance is a useful tool here, as we are able to probe the band structure of the material without direct interference from defect states and other non-idealities that show emission in the PL. This therefore helps to determine more fully the transitions contributing to the PL spectra.

The highest energy feature in the PR, visible in both the single and 5 quantum well samples, matches well with the first peak in the PL spectra and is due to the InAlAs barrier material (P1 in previous section). This first feature shows a traditional red shift with temperature,

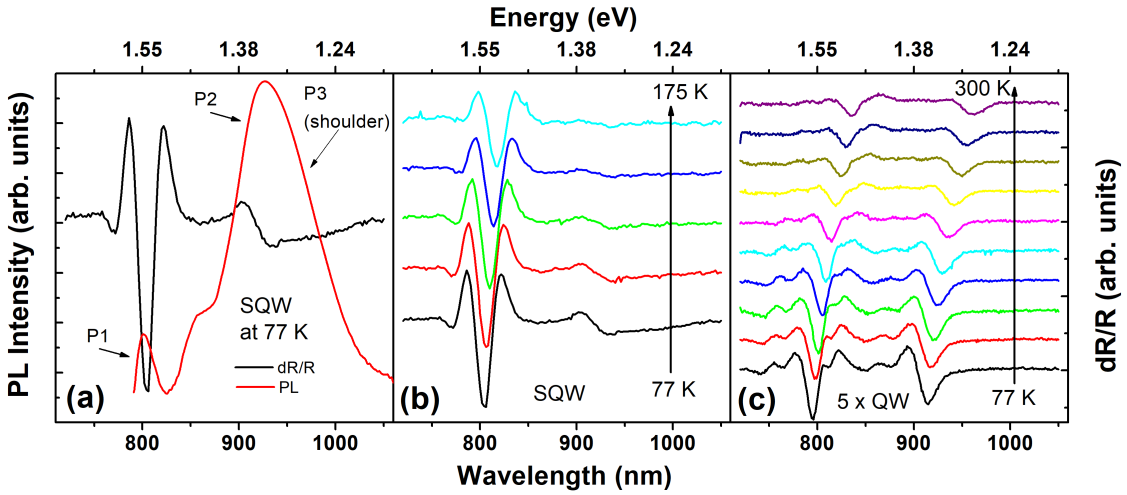

Figure 6.5: (a) Comparison of the PR and PL spectra obtained from the single QW sample at 77 K. (b,c) Waterfall plots of temperature dependent PR for the single QW sample and the 5 QW sample, respectively. Temperature dependent measurements of the single QW sample were only taken up to 175 K, as the feature of interest (lowest energy feature) disappeared at that temperature.

which is consistent with the expansion of the crystal lattice [25]. The lower energy feature, visible in both samples at low temperature, are related to the QW states (P2 in previous section). In the single QW sample, this feature washes out quickly with temperature, due to the limited absorption of the single 2 nm thick QW absorber. Interestingly, no feature is immediately apparent that corresponds to the P3 peak in the previous section, likely due to the low absorption of this type-II transition. In the PR taken of 5 quantum well sample (see Figure 6.5 (c)), this lower energy feature is visible up to room temperature, and also follows typical temperature dependence of III-V semiconductors. There are additional features at low temperature in the 5 quantum well PR spectra, which may be additional states from the

quantum well, interface states, or Franz-Keldysh oscillations. Further fitting of this data is ongoing, to better understand these features.

6.2.4 Electrical Transport Measurements

Upon completion of spectroscopy measurements, the samples were processed into solar cells using standard III-V fabrication techniques. Temperature dependent J-V and EQE measurements were performed to illuminate details about the carrier collection and absorption of this structure. EQE measurements are plotted in Figure 6.6 (a), along with the PL spectra of the single QW sample taken at 77 K. In comparing the EQE (olive green curve) and PL at 77 K, good agreement is observed between the location of the InAlAs peak, and the main absorption edge, located around 800 nm. Emission from the QW is observed around 950 nm, which corresponds to a slight increase in absorption in this region. This limited absorption is expected, as there is only a single 2 nm quantum well present, though higher carrier collection is expected from the thicker layers of the InAlAs. This may indicate insufficient window etching of the InP cap. The low EQE observed along with the presence of strong luminescence at all temperatures indicates large recombination losses, and limited carrier extraction. This suggests carrier localization is dominant in the current structure.

The temperature dependence of the EQE shows an increase in the InAlAs and the InP QW regions as the temperature is reduced, with the majority of the increase occurring in the InAlAs region. Further evidence of this temperature dependent behavior is observed in the J-V measurements taken under AM0 illumination and in the dark, shown in Figure 6.6 (b and c), respectively. A clear increase of V_{oc} and J_{sc} is observed as the temperature is reduced, matching well with the EQE results. The dark J-V characteristics show a reduction

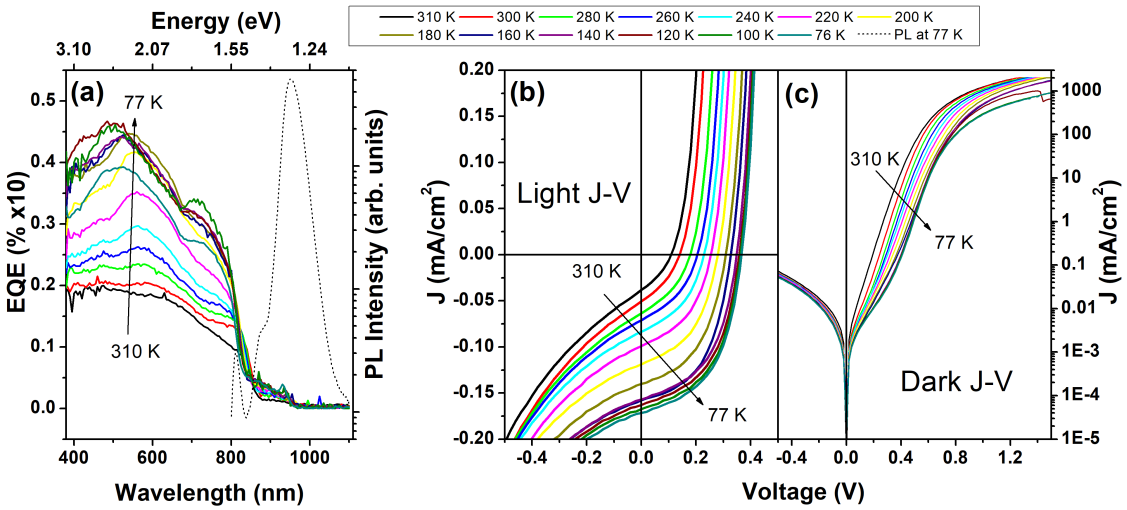

Figure 6.6: (a) Comparison of EQE and PL data from the single QW sample, showing good agreement between peaks in the PL and absorption edges in the EQE. The PL shown here was acquired at 77 K. (b) Light and (c) Dark J-V measurements of a single QW device, showing an increase in V_{oc}, J_{sc}, FF, and a reduction in dark current with decreasing temperature.

in dark current as temperature is decreased. In these samples, the quantum well is placed in an NIP structure to provide an electric field to sweep photogenerated carriers. In this case, the well is thin and shallow, and therefore thermally generated carriers in the influence of the internal field are able to easily pass the well at higher temperatures, producing higher dark current and smaller shunt resistance. As the temperature and thermal energy of the carriers is decreased, the well becomes more effective at confining carriers which increases the luminescence, but also decreases the dark current by limiting shunting, and increases the collection efficiency. Further evidence to support this analysis is the increased carrier leakage at higher reverse bias indicating larger direct tunneling under these conditions.

6.3 Conclusion

In summary, an InP/InAlAs QW structure was investigated using PL, PR, EQE and J-V measurements. A number of different features were observed in the PL spectra, which were determined to be related to the InAlAs barrier material, and the InP quantum well. PL emission energies were observed to be lower than expected, which may be due to additional unintentional InAs and/or InAlP layers. Power dependent PL measurements gave evidence for a type-II transition, related to the QW and/or other interfaces in this structure.

PR measurements show features related to the barrier material and the QW, but no evidence of the type-II transition observed in the power dependent PL. Absorption edges of the QW and barrier material correspond well to the associated peaks in the PL spectra. Finally, J-V measurements show photovoltaic behavior, though this is restricted by the limited absorption of the single thin QW absorber and large shunt currents across the active region. This results in better photovoltaic performance at lower temperature, where transit across the well is more limited by the thermal energy of the carriers. Further investigation of this system with high power monochromatic illumination and with high energy particle irradiation will help determine this system's effectiveness in space applications.

Chapter 7

Summary and Future Work

In this dissertation, several different photovoltaic technologies have been investigated for use in space, where radiation and extreme conditions can pose problems for solar power. While one study presented here focused on improving traditional multijunction solar cells, others have focused on thin film technologies, which have the potential to be less expensive, light weight, and flexible, though are less efficient. These attributes may allow for deployable photovoltaic arrays compatible with the smaller CubeSat and SmallSat form factors. With the rapidly changing technological landscape of the day, the satellite market is turning to cheaper short-life satellites that can be replaced more often. The studies here have focused not only on applications around Earth, but also for missions to Mars, Jupiter and Saturn.

In addition to the standard photovoltaic testing methods, the studies presented here have also subjected devices to high energy radiation and investigated performance under low intensity and low temperature. High energy particle bombardment is common to all space missions and is particularly intense in the belts around planets with magnetic fields, like our own Earth and to a greater extent, Jupiter. The damage accumulated from radiation exposure results in loss of power conversion efficiency over the lifetime of the solar array. However, some materials and even structures, show different susceptibilities to this damage, which is why the devices studied here undergo this testing. Further, the outer planets extreme distance from the sun results in low incident light received, and thus low temperatures are experienced. These low intensity and low temperature conditions can illuminate barriers and other non-idealities not experienced under standard conditions, requiring testing.

In Chapter 3, a UV-activated hydrogenation process is investigated for use in improving the material quality in GaInNAs solar cells. This 1 eV band gap material has been under study for a number of years as an additional junction in epitaxially grown multijunction solar cells destined for space. Previous studies of this process showed improvement in GaInNAs based solar cells, though some non-ideal features in the PL remained. Here, optical samples were studied via photoluminescence spectroscopy, to better understand the effect of hydrogen on this system. Temperature dependent measurements after hydrogenation showed the complete removal of the characteristic 's-shape' in the peak energy dependence. This 's-shape' is common in the GaInNAs system and reflects emission at lower energy than the band gap, usually related to carrier localization by alloy fluctuations, isoelectronic centers, and/or other defects. Here, it is believed that the carrier localization feature is the result of alloy fluctuations driven by nitrogen, as a recent DFT study showed indium to be relatively unaffected by hydrogen. Though this lower energy emission in the hydrogenated sample was reduced, it was not eliminated, illustrating the need for a higher hydrogen dose. Density functional theory calculations were performed, highlighting additional states forming as a result of nitrogen introduction, and movement of these states upon the formation of N-H clusters with hydrogenation. These N-H clusters also moved the fermi level closer to the conduction band, indicating donor effects.

Further studies into the effect of the hydrogenation on the doping were performed on n- and p-type optical GaInNAs samples. Significant changes in the PL spectra of the p-type sample were observed upon hydrogenation, while relatively little change was seen in the n-type sample. This is attributed to the donor nature of the N-H complexes formed, and the

effect of the p-type dopants in depleting electron traps. Further measurements on Hall and Schottky diode samples are underway in order to confirm these findings.

An initial radiation study on a GaInNAs solar cell was then performed. PL and EQE measurements after irradiation show evidence of a shift in the band gap, likely due to the relaxation of strain in the material by the high energy particle bombardment. A loss in EQE was observed, though J-V characteristics showed little change, and even improvement. These unusual effects are believed to be systematic in nature, and further investigation are underway in order to confirm these suspicions. Additional experiments are also planned to further probe the radiation tolerance of this system, and to determine the area of relaxation in the device.

Chapter 4 details the investigation of commercial Cu(In,Ga)Se_2 solar cells on a flexible stainless steel substrate for use in deep space missions. Initial studies began with PL studies on absorber and solar cell material, which showed evidence of shallow defects in the region of the bulk CIGS band gap, though these defects appear to not significantly affect solar cell performance. Studies of rapid thermal annealing of CIGS solar cells with different temperatures showed a complete reversal of the diode characteristic. This unusual behavior is assigned with the formation of a barrier or reverse diode, possibly close to the molybdenum back contact. These initial studies suggested that higher temperature annealing in forming gas is not beneficial for these devices, though further investigation is needed to determine the mechanism behind the unusual J-V characteristics.

Pristine CIGS devices were then subjected to temperature dependent J-V measurements, where a cross-over in the light and dark J-V curves gave evidence of some barrier in the device, and unusual temperature dependence of the J_{sc} is associated with unfreezing of metastable

defect states. A thermal cycling experiment was performed, which showed no obvious sign of problems with the thermal stress. Performance of these devices under LILT conditions consistent with orbits of Mars, Jupiter and Saturn were reported, for devices in the as grown or relaxed configuration and in the light-soaked configuration. An inflection point in the forward bias regime past V_{oc} was shown, and is associated with a photo-activated barrier, perhaps at the CdS/CIGS interface or the back contact. Finally, CIGS devices were irradiated with high energy protons, where degradation was observed, consistent with previous results. Self-healing of the irradiated devices under elevated operating temperatures was reported. Further investigation of the effect of the metastable behavior in CIGS on LILT performance is underway, with experiments in intensity dependence, electroluminescence and irradiation energy dependence.

Chapter 5 reports the investigation of high-stability triple cation (Formamidinium, Methylammonium and Cesium, known as FAMACs) based perovskite solar cells for use in deep space missions. PL measurements of the FAMACs layer were reported, which showed no clear signs of phase changes at low temperature, indicating good stability. The broadening behavior of this PL was investigated, and the majority of the broadening was associated with LO-phonon processes, consistent with the polar nature of the FAMACs perovskite. Temperature dependent J-V measurements were reported, and poor performance was observed at low temperature. Additionally, hysteresis was observed only at higher temperatures, and it was postulated that the mechanism was frozen out at low temperatures. Interestingly, devices measured under both low intensity *and* low temperature had performance comparable to room temperature. This behavior was associated with a temperature and intensity dependent barrier, unintentional to this system and likely at the SnO_2/FAMACs interface. Further bias

dependent PL and EQE measurements were put forth, which gave evidence for this barrier to be mediated by thermionic emission. Thus, this barrier, which is large compared to the thermal energy of the carriers at low temperature, can only pass small amounts of current without creating large resistances. While this barrier was unintentional, the recovery of the PCE under LILT conditions showed the potential of these systems in deep space conditions, and its ability to weather unavoidable degradation. Higher performance perovskite devices are under investigation now, with plans for irradiation studies. Investigations are also underway on different iterations of the device structure, and encapsulation methods.

In Chapter 6, an initial investigation of InP/InAlAs QW solar cells is described. PL spectra were shown, where a number of features were observed, and assigned to the InAlAs barrier material, the InP QW, and type-II interfaces at the QW and/or other interfaces in this structure. Modeling of the QW transitions was done in NRL Multibands, and showed higher energies than were observed in the PL spectra. This discrepancy was theorized to be due to unavoidable thin InAs or InAlP layers at the InP/InAlAs interfaces of the QW. Signs of limited absorption and large dark currents were observed in the J-V and EQE measurements, both of which were assigned to the thin, shallow nature of the QW in the device investigated. Radiation studies of this system are planned to compare the radiation tolerance with other more established systems.

References

[1] R. L. Easton and M. J. Votaw, "Vanguard I IGY satellite (1958 beta)," *Review of Scientific Instruments*, vol. 30, no. 2, pp. 70–75, 1959. [Online]. Available: https://doi.org/10.1063/1.1716492.

[2] D. R. Williams. (Sep. 2019). Vangaurd 1. (accessed Sep 12, 2019), National Aeronautics and Space Administration, [Online]. Available: https://nssdc.gsfc.nasa.gov/nmc/spacecraft/display.action?id=1958-002B.

[3] *Atomic Power in Space II: A History of Space Nuclear Power and Propulsion in the United States*. Idaho National Laboratory, 2015. [Online]. Available: https://inl.gov/research-program/space-power-systems/.

[4] E. Piazza. (Sep. 2019). Radioisotope power systems: Missions. (accessed Sep 5, 2019), NASA's Jet Propulsion Laboratory, [Online]. Available: https://rps.nasa.gov/missions/?page=0&per_page=40&order=date+desc&search=.

[5] R. M. Wham. (Dec. 2015). ORNL achieves milestone with plutonium-238 sample. (accessed Sep 13, 2019), Oak Ridge National Laboratory, [Online]. Available: https://www.ornl.gov/news/ornl-achieves-milestone-plutonium-238-sample.

[6] M. A. Gibson, S. R. Oleson, D. I. Poston, and P. McClure, "NASA's kilopower reactor development and the path to higher power missions," in *2017 IEEE Aerospace Conference*, Mar. 2017, pp. 1–14.

[7] T. Kerslake and E. Gustafson, "On-orbit performance degradation of the International Space Station P6 photovoltaic arrays," in *1st International Energy Conversion En-*

gineering Conference (IECEC), 2003. [Online]. Available: https://arc.aiaa.org/doi/abs/10.2514/6.2003-5999.

[8] *Nrel's "best research-cell efficiencies" chart*, (accessed Sep 11, 2019), Sep. 2019. [Online]. Available: https://www.nrel.gov/pv/cell-efficiency.html.

[9] A. Duda, S. Ward, and M. Young, "Inverted metamorphic multijunction (IMM) cell processing instructions," Feb. 2012.

[10] C.-W. Cheng, K.-T. Shiu, N. Li, S.-J. Han, L. Shi, and D. K. Sadana, "Epitaxial lift-off process for gallium arsenide substrate reuse and flexible electronics," *Nature Communications*, vol. 4, p. 1577, 2013. [Online]. Available: https://doi.org/10.1038/ncomms2583.

[11] A. Jasenek, U. Rau, K. Weinert, H. W. Schock, and J. H. Werner, "Radiation response of Cu(In,Ga)Se_2 solar cells," in *3rd World Conference on Photovoltaic Energy Conversion*, vol. 1, IEEE Xplore, 2003, pp. 593–598. [Online]. Available: http://ieeexplore.ieee.org/abstract/document/1305352/.

[12] K. A. Horowitz, T. W. Remo, B. Smith, and A. J. Ptak, "A techno-economic analysis and cost reduction roadmap for III-V solar cells," Nov. 2018.

[13] C. Henry. (Apr. 2019). Amazon planning 3,236-satellite constellation for internet connectivity. (accessed Sep 19, 2019), Future US, Inc., [Online]. Available: https://www.space.com/amazon-plans-3236-satellite-constellation-for-internet.html.

[14] D. J. Hoffman, T. W. Kerslake, A. F. Hepp, and R. P. Raffaelle, "Thin-Film Solar Array Earth Orbit Mission Applicability Assessment," in *17th Space Photovoltaic Research and Technology Conference*, Oct. 2002, pp. 74–83.

[15] Chetvorno. (Mar. 2017). File:solid state electronic band structure.svg, [Online]. Available: `https://commons.wikimedia.org/wiki/File:Solid_state_electronic_band_structure.svg`.

[16] W. Shockley and H. J. Queisser, "Detailed balance limit of efficiency of p-n junction solar cells," *Journal of Applied Physics*, vol. 32, no. 3, pp. 510–519, 1961. [Online]. Available: `https://doi.org/10.1063/1.1736034`.

[17] L. C. Hirst and N. J. Ekins-Daukes, "Fundamental losses in solar cells," *Progress in Photovoltaics: Research and Applications*, vol. 19, no. 3, pp. 286–293, 2011. [Online]. Available: `https://onlinelibrary.wiley.com/doi/abs/10.1002/pip.1024`.

[18] A. Luque and A. Martí, "Increasing the efficiency of ideal solar cells by photon induced transitions at intermediate levels," *Phys. Rev. Lett.*, vol. 78, pp. 5014–5017, 26 Jun. 1997. [Online]. Available: `https://link.aps.org/doi/10.1103/PhysRevLett.78.5014`.

[19] R. T. Ross and A. J. Nozik, "Efficiency of hot-carrier solar energy converters," *Journal of Applied Physics*, vol. 53, no. 5, pp. 3813–3818, 1982. [Online]. Available: `https://doi.org/10.1063/1.331124`.

[20] G. A. Landis and J. Fincannon, "Study of power options for Jupiter and outer planet missions," in *2015 IEEE 42nd Photovoltaic Specialist Conference (PVSC)*, 2015, pp. 1–5.

[21] V. G. Weizer and J. D. Broder, "On the cause of the flat-spot phenomenon observed in silicon solar cells at low temperatures and low intensities," *Journal of Applied Physics*, vol. 53, no. 8, pp. 5926–5930, 1982. [Online]. Available: http://aip.scitation.org/doi/abs/10.1063/1.331435.

[22] D. A. Scheiman and D. B. Snyder, "Low intensity low temperature (LILT) measurements of state-of-the-art triple junction solar cells for space missions," in *2008 33rd IEEE Photovoltaic Specialists Conference*, 2008, pp. 1–6.

[23] N. S. Fatemi, S. Sharma, O. Buitrago, J. Crisman, P. R. Sharps, R. Blok, M. Kroon, C. Jalink, R. Harris, P. Stella, and S. Distefano, "Performance of high-efficiency advanced triple-junction solar panels for the LILT mission Dawn," in *Conference Record of the Thirty-first IEEE Photovoltaic Specialists Conference, 2005.*, Jan. 2005, pp. 618–621.

[24] N. Miller, "SolAero solar cell development and characterization in extreme environments," in *Proceedings of the 25th Space Photovoltaic Research and Technology Conference*, 2018, p. 18. [Online]. Available: https://www.grc.nasa.gov/WWW/SPRAT/Abstract%20BOOK%20SPRATXXV.pdf.

[25] Y. P. Varshni, "Temperature dependence of the energy gap in semiconductors," *Physica*, vol. 34, no. 1, pp. 149–154, 1967. [Online]. Available: http://www.sciencedirect.com/science/article/pii/0031891467900626.

[26] A. D. Sheikh, R. Munir, M. A. Haque, A. Bera, W. Hu, P. Shaikh, A. Amassian, and T. Wu, "Effects of high temperature and thermal cycling on the performance of perovskite solar cells: Acceleration of charge recombination and deterioration of charge

extraction," *ACS Applied Materials & Interfaces*, vol. 9, no. 40, pp. 35 018–35 029, 2017, PMID: 28921949. [Online]. Available: https://doi.org/10.1021/acsami.7b11250.

[27] M. G. Flammini, N. Debernardi, M. Le Ster, B. Dunne, J. Bosman, and M. Theelen, "The influence of heating time and temperature on the properties of CIGSSe solar cells," *International Journal of Photoenergy*, vol. 2016, p. 7, 2016. [Online]. Available: http://dx.doi.org/10.1155/2016/4089369.

[28] W. Hohmann, *Die Erreichbarkeit der Himmelskörper: Untersuchungen über das Raumfahrtproblem*. Oldenbourg, 1994. [Online]. Available: https://archive.org/details/nasa_techdoc_19980230631/page/n35.

[29] V. Rauschenbakh, M. Ovchinnikov, and S. McKenna-Lawlor, "Essential spaceflight dynamics and magnetospherics," in, ser. Space Technology Library. Springer Netherlands, 2006, ch. 12, pp. 146–147. [Online]. Available: https://books.google.com/books?id=pQ0GCAAAQBAJ.

[30] M. Vasile and P. D. Pascale, "Preliminary Design of Multiple Gravity-Assist Trajectories," *Journal of Spacecraft and Rockets*, vol. 43, no. 4, pp. 794–805, Jul. 2006.

[31] A. E. Petropoulos, J. M. Longuski, and E. P. Bonfiglio, "Trajectories to jupiter via gravity assists from venus, earth, and mars," *Journal of Spacecraft and Rockets*, vol. 37, no. 6, pp. 776–783, 2000. [Online]. Available: https://doi.org/10.2514/2.3650.

[32] M. S. Rund, "Interplanetary transfer trajectories using the invariant manifolds of halo orbits," Master's thesis, California Polytechnic State University, San Luis Obispo, 2018.

[33] G. Dakermanji, J. Jenkins, and C. J. Ercol, "The messenger spacecraft solar array design and early mission performance," in *2006 IEEE 4th World Conference on Photovoltaic Energy Conference*, vol. 2, May 2006, pp. 1919–1922.

[34] U. Feldman, U. Schuhle, K. G. Widing, and J. M. Laming, "Coronal composition above the solar equator and the north pole as determined from spectra acquired by the SUMER instrument on SOHO," *The Astrophysical Journal*, vol. 505, no. 2, pp. 999–1006, Oct. 1998. [Online]. Available: https://doi.org/10.1086%2F306195.

[35] C. Claeys and E. Simoen, "Basic radiation damage mechanisms in semiconductor materials and devices," in *Radiation Effects in Advanced Semiconductor Materials and Devices*. Berlin, Heidelberg: Springer Berlin Heidelberg, 2002, pp. 9–52. [Online]. Available: https://doi.org/10.1007/978-3-662-04974-7_2.

[36] S. N. Vernov, E. V. Gorchakov, P. I. Shavrin, and K. N. Sharvina, "Radiation belts in the region of the south-atlantic magnetic anomaly," *Space Science Reviews*, vol. 7, no. 4, pp. 490–533, Nov. 1967. [Online]. Available: https://doi.org/10.1007/BF00182684.

[37] S. J. Bolton, R. M. Thorne, S. Bourdarie, I. de Pater, and B. Mauk, "Jupiter's inner radiation belts," in *Jupiter. The Planet, Satellites and Magnetosphere*, F. Bagenal, T. E. Dowling, and W. B. McKinnon, Eds. 2004, pp. 671–688.

[38] R. S. Grammier, "An overview of the Juno mission to Jupiter," in *International Symposium on Space Technology and Science*, Jun. 2006, pp. 1567–1575.

[39] F. A. Lindholm, J. G. Fossum, and E. L. Burgess, "Application of the superposition principle to solar-cell analysis," *IEEE Transactions on Electron Devices*, vol. 26, no. 3, pp. 165–171, Mar. 1979.

[40] C. Zhang, J. Zhang, Y. Hao, Z. Lin, and C. Zhu, "A simple and efficient solar cell parameter extraction method from a single current-voltage curve," *Journal of Applied Physics*, vol. 110, no. 6, p. 064 504, 2011. [Online]. Available: https://aip.scitation.org/doi/abs/10.1063/1.3632971.

[41] *G173-03(2012) standard tables for reference solar spectral irradiances: Direct normal and hemispherical on 37° tilted surface*, ASTM International, West Conshohocken, PA: ASTM International, 2012.

[42] J. S. McNatt, D. S. Wolford, and M. G. Myers, *U.S. high altitude PV measurement for primary calibration standard certification*, NASA Technical Reports Server, Dec. 2012.

[43] D. B. Snyder and D. S. Wolford, "A low cost weather balloon borne solar cell calibration payload," in *2012 38th IEEE Photovoltaic Specialists Conference*, IEEE, 2012, pp. 001 512–001 516.

[44] K. M. Edmondson, A. Howard, P. Hausgen, P. Jenkins, D. Bhusari, S. Wierman, S. Mesropian, D. C. Law, R. Bardfield, R. R. King, *et al.*, "Initial on-orbit performance analysis of inverted metamorphic (IMM3J) solar cells on MISSE-7," in *2011 37th IEEE Photovoltaic Specialists Conference*, IEEE, 2011, pp. 003 719–003 723.

[45] D. R. Williams, *Planetary fact sheet - metric*, Web Page, (accessed Jun 15,2017), Jun. 2017. [Online]. Available: https://nssdc.gsfc.nasa.gov/planetary/factsheet/.

[46] B. Uma, M. Sankaran, and S. E. Puthanveettil, "Multijunction solar cell performance in mars orbiter mission (MOM) conditions," *E3S Web Conf.*, vol. 16, p. 04 001, 2017. [Online]. Available: https://doi.org/10.1051/e3sconf/20171604001.

[47] M. Gloeckler, "Device physics of copper(indium,gallium)selenide(2) thin-film solar cells," Thesis, Colorado State University, 2005.

[48] P. K. Paul, J. Bailey, G. Zapalac, and A. R. Arehart, "Fast C-V method to mitigate effects of deep levels in CIGS doping profiles," in *2017 IEEE 44th Photovoltaic Specialist Conference (PVSC)*, Jun. 2017, pp. 2414–2418.

[49] M. Grundmann, *The Physics of Semiconductors: An Introduction Including Nanophysics and Applications*, ser. Graduate Texts in Physics. Springer Berlin Heidelberg, 2010. [Online]. Available: https://books.google.com/books?id=ECI4EccXltUC.

[50] J. Pankove, *Optical Processes in Semiconductors*, ser. Dover books explaining science and mathematics. Dover, 1975. [Online]. Available: https://books.google.com/books?id=HHM9Vo0DYZAC.

[51] M. D. Sturge, E. Cohen, and K. F. Rodgers, "Thermal quenching processes in the low temperature photoluminescence of excitons bound to nitrogen pairs in GaP," *Phys. Rev. B*, vol. 15, pp. 3169–3179, 6 Mar. 1977. [Online]. Available: https://link.aps.org/doi/10.1103/PhysRevB.15.3169.

[52] K. Matsuda, S. V. Nair, H. E. Ruda, Y. Sugimoto, T. Saiki, and K. Yamaguchi, "Two-exciton state in GaSb/GaAs type II quantum dots studied using near-field photoluminescence spectroscopy," *Applied Physics Letters*, vol. 90, no. 1, 013101, p. 013 101, 2007. [Online]. Available: http://scitation.aip.org/content/aip/journal/apl/90/1/10.1063/1.2425039.

[53] L. C. Hirst, M. P. Lumb, J. Abell, C. T. Ellis, J. G. Tischler, I. Vurgaftman, J. R. Meyer, R. J. Walters, and M. González, "Spatially indirect radiative recombination

in InAlAsSb grown lattice-matched to InP by molecular beam epitaxy," *Journal of Applied Physics*, vol. 117, no. 21, 215704, p. 215 704, 2015. [Online]. Available: http://scitation.aip.org/content/aip/journal/jap/117/21/10.1063/1.4921883.

[54] J. Misiewicz, P. Sitarek, G. Sęk, and R. Kudrawiec, "Semiconductor heterostructures and device structures investigated by photoreflectance spectroscopy," *Materials Science Poland*, vol. 21, no. 3, pp. 263–320, 2003.

[55] R. E. Nahory and J. L. Shay, "Reflectance modulation by the surface field in GaAs," *Phys. Rev. Lett.*, vol. 21, pp. 1569–1571, 23 Dec. 1968. [Online]. Available: https://link.aps.org/doi/10.1103/PhysRevLett.21.1569.

[56] B. V. Shanabrook, O. J. Glembocki, and W. T. Beard, "Photoreflectance modulation mechanisms in GaAs-$Al_xGa_{1-x}As$ multiple quantum wells," *Phys. Rev. B*, vol. 35, pp. 2540–2543, 5 Feb. 1987. [Online]. Available: https://link.aps.org/doi/10.1103/PhysRevB.35.2540.

[57] R. Enderlein, D. Jiang, and Y. Tang, "On the mechanisms of photoreflectance in multiple quantum wells," *physica status solidi (b)*, vol. 145, no. 1, pp. 167–180, 1988. [Online]. Available: https://onlinelibrary.wiley.com/doi/abs/10.1002/pssb.2221450114.

[58] B. O. Seraphin and N. Bottka, "Band-structure analysis from electro-reflectance studies," *Phys. Rev.*, vol. 145, pp. 628–636, 2 May 1966. [Online]. Available: https://link.aps.org/doi/10.1103/PhysRev.145.628.

[59] D. Aspnes, "Third-derivative modulation spectroscopy with low-field electroreflectance," *Surface Science*, vol. 37, pp. 418 –442, 1973. [Online]. Available: http://www.sciencedirect.com/science/article/pii/0039602873903373.

[60] D. A. B. Miller, D. S. Chemla, T. C. Damen, A. C. Gossard, W. Wiegmann, T. H. Wood, and C. A. Burrus, "Band-edge electroabsorption in quantum well structures: The quantum-confined stark effect," *Phys. Rev. Lett.*, vol. 53, pp. 2173–2176, 22 Nov. 1984. [Online]. Available: https://link.aps.org/doi/10.1103/PhysRevLett.53.2173.

[61] R. Kudrawiec, A. Khachapuridze, G. Cywinski, T. Suski, and J. Misiewicz, "Fast measurements of photoreflectance spectra by using multi-channel detector," *physica status solidi (a)*, vol. 206, no. 5, pp. 847–850, 2009. [Online]. Available: https://onlinelibrary.wiley.com/doi/abs/10.1002/pssa.200881410.

[62] S. R. Kurtz, D. Myers, and J. M. Olson, "Projected performance of three- and four-junction devices using GaAs and GaInP," in *Conference Record of the Twenty Sixth IEEE Photovoltaic Specialists Conference - 1997*, Sep. 1997, pp. 875–878.

[63] J. F. Geisz and D. J. Friedman, "III-N-V semiconductors for solar photovoltaic applications," *Semiconductor Science and Technology*, vol. 17, no. 8, pp. 769–777, 2002.

[64] P. Colter, B. Hagar, and S. Bedair, "Tunnel junctions for III-V multijunction solar cells review," *Crystals*, vol. 8, no. 12, 2018. [Online]. Available: https://www.mdpi.com/2073-4352/8/12/445.

[65] D. J. Aiken, "InGaP/GaAs/Ge multi-junction solar cell efficiency improvements using epitaxial germanium," *Conference Record of the Twenty-Eighth IEEE Photovoltaic Specialists Conference - 2000 (Cat. No.00CH37036)*, pp. 994–997, 2000.

[66] R. Garrison and R. Kleiman, "Higher efficiency tandem solar cells through composite-cell current matching," *Opt. Express*, vol. 27, no. 8, A543–A571, Apr. 2019. [Online]. Available: `http://www.opticsexpress.org/abstract.cfm?URI=oe-27-8-A543`.

[67] (Apr. 2018). IMM-α preliminary datasheet. (accessed Sep 12, 2019), SolAero Technologies, [Online]. Available: `https://solaerotech.com/wp-content/uploads/2018/04/IMM-alpha-Preliminary-Datasheet-April-2018-v.1.pdf`.

[68] W. Shan, W. Walukiewicz, J. W. Ager, E. E. Haller, J. F. Geisz, D. J. Friedman, J. M. Olson, and S. R. Kurtz, "Band anticrossing in GaInNAs alloys," *Physical Review Letters*, vol. 82, pp. 1221–1224, 6 Feb. 1999. [Online]. Available: `http://link.aps.org/doi/10.1103/PhysRevLett.82.1221`.

[69] M. Kondow, T. Kitatani, S. Nakatsuka, M. C. Larson, K. Nakahara, Y. Yazawa, M. Okai, and K. Uomi, "GaInNAs: a novel material for long-wavelength semiconductor lasers," *IEEE Journal of Selected Topics in Quantum Electronics*, vol. 3, no. 3, pp. 719–730, Jun. 1997.

[70] J. F. Geisz, D. J. Friedman, J. M. Olson, C. Kramer, A. Kibbler, and S. R. Kurtz, "New materials for future generations of III-V solar cells," in *American Institute of Physics Conference Series*, ser. American Institute of Physics Conference Series, vol. 462, Mar. 1999, pp. 372–377.

[71] D. Friedman, J. Geisz, S. Kurtz, and J. Olson, "1-eV solar cells with GaInNAs active layer," *Journal of Crystal Growth*, vol. 195, no. 1-4, pp. 409 –415, 1998. [Online]. Available: http://www.sciencedirect.com/science/article/pii/S0022024898005612.

[72] D. Derkacs, R. Jones-Albertus, F. Suarez, and O. Fidaner, "Lattice-matched multi-junction solar cells employing a 1 eV GaInNAsSb bottom cell," *J. Photon. Energy*, vol. 2, p. 021 805, 2012.

[73] X. Yang, J. B. Héroux, L. F. Mei, and W. I. Wang, "InGaAsNSb/GaAs quantum wells for 1.55 μm lasers grown by molecular-beam epitaxy," *Applied Physics Letters*, vol. 78, no. 26, pp. 4068–4070, 2001.

[74] H. Shimizu, K. Kumada, S. Uchiyama, and A. Kasukawa, "1.2 μm range GaInAs SQW lasers using Sb as surfactant," *Electronics Letters*, vol. 36, no. 16, pp. 1379–1381, Aug. 2000.

[75] W. Ha, V. Gambin, S. Bank, M. Wistey, J. S. Harris, and Seongsin Kim, "Long wavelength GaInNAs(Sb) lasers on GaAs," in *Summaries of Papers Presented at the Lasers and Electro-Optics. CLEO '02. Technical Digest*, May 2002, 269–270 vol.1.

[76] S. Bank, W. Ha, V. Gambin, M. Wistey, H. Yuen, L. Goddard, S. Kim, and J. S. Harris, "1.5 μm GaInNAs(Sb) lasers grown on GaAs by MBE," *Journal of Crystal Growth*, vol. 251, no. 1, pp. 367 –371, 2003, Proceedings of the Twelfth International Conference on Molecular Beam Epitaxy. [Online]. Available: http://www.sciencedirect.com/science/article/pii/S0022024802024466.

[77] V. Polojarvi, A. Aho, A. Tukiainen, M. Raappana, T. Aho, A. Schramm, and M. Guina, "Influence of As/group-III flux ratio on defects formation and photovoltaic performance of GaInNAs solar cells," *Solar Energy Materials and Solar Cells*, vol. 149, pp. 213 –220, 2016. [Online]. Available: http://www.sciencedirect.com/science/article/pii/S0927024816000374.

[78] E.-M. Pavelescu, J. Wagner, H.-P. Komsa, T. T. Rantala, M. Dumitrescu, and M. Pessa, "Nitrogen incorporation into GaInNAs lattice-matched to GaAs: the effects of growth temperature and thermal annealing," *Journal of Applied Physics*, vol. 98, no. 8, 083524, p. 083 524, 2005. [Online]. Available: http://scitation.aip.org/content/aip/journal/jap/98/8/10.1063/1.2112173;jsessionid=gOPjtAOLB3lYIsKkQIwPwB3K.x-aip-live-02.

[79] I hsiu Ho and G. Stringfellow, "Solubility of nitrogen in binary III-V systems," *Journal of Crystal Growth*, vol. 178, no. 1, pp. 1 –7, 1997. [Online]. Available: http://www.sciencedirect.com/science/article/pii/S002202489700078X.

[80] X. J. Wang, Y. Puttisong, C. W. Tu, A. J. Ptak, V. K. Kalevich, A. Y. Egorov, L. Geelhaar, H. Riechert, W. M. Chen, and I. A. Buyanova, "Dominant recombination centers in Ga(In)NAs alloys: Ga interstitials," *Applied Physics Letters*, vol. 95, no. 24, 241904, p. 241 904, 2009. [Online]. Available: http://scitation.aip.org/content/aip/journal/apl/95/24/10.1063/1.3275703.

[81] A. M. Mintairov, K Sun, J. L. Merz, H Yuen, S Bank, M Wistey, J. S. Harris, G Peake, A Egorov, V Ustinov, R Kudrawiec, and J Misiewicz, "Atomic arrangement and emission properties of GaAs(In, Sb)N quantum wells," *Semiconductor Science and Technology*,

vol. 24, no. 7, p. 075 013, 2009. [Online]. Available: http://stacks.iop.org/0268-1242/24/i=7/a=075013.

[82] R. Kudrawiec, M. Latkowska, M. Baranowski, J. Misiewicz, L. H. Li, and J. C. Harmand, "Photoreflectance, photoluminescence, and microphotoluminescence study of optical transitions between delocalized and localized states in $GaN_{0.02}As_{0.98}$, $Ga_{0.95}In_{0.05}$ - $N_{0.02}As_{0.98}$, and $GaN_{0.02}As_{0.90}Sb_{0.08}$ layers," *Physical Review B*, vol. 88, p. 125 201, 12 Sep. 2013. [Online]. Available: http://link.aps.org/doi/10.1103/PhysRevB.88.125201.

[83] R. Kudrawiec, M. Syperek, M. Latkowska, J. Misiewicz, V.-M. Korpijärvi, P. Laukkanen, J. Pakarinen, M. Dumitrescu, M. Guina, and M. Pessa, "Influence of non-radiative recombination on photoluminescence decay time in GaInNAs quantum wells with Ga- and In-rich environments of nitrogen atoms," *Journal of Applied Physics*, vol. 111, no. 6, p. 063 514, 2012. [Online]. Available: http://dx.doi.org/10.1063/1.3695457.

[84] M. Baranowski, R. Kudrawiec, M. Syperek, J. Misiewicz, T. Sarmiento, and J. S. Harris, "Time-resolved photoluminescence studies of annealed 1.3-μm GaInNAsSb quantum wells," *Nanoscale Research Letters*, vol. 9, no. 1, p. 81, 2014. [Online]. Available: http://dx.doi.org/10.1186/1556-276X-9-81.

[85] I. R. Sellers, W.-S. Tan, K. Smith, S. Hooper, S. Day, and M. Kauer, "Wide depletion width of 1 eV GaInNAs solar cells by thermal annealing," *Applied Physics Letters*, vol. 99, no. 15, 151111, p. 151 111, 2011. [Online]. Available: http://scitation.aip.org/content/aip/journal/apl/99/15/10.1063/1.3648110.

[86] S. G. Spruytte, C. W. Coldren, J. S. Harris, W. Wampler, P. Krispin, K. Ploog, and M. C. Larson, "Incorporation of nitrogen in nitride-arsenides: Origin of improved luminescence efficiency after anneal," *Journal of Applied Physics*, vol. 89, no. 8, pp. 4401–4406, 2001. [Online]. Available: http://scitation.aip.org/content/aip/journal/jap/89/8/10.1063/1.1352675.

[87] W. Li, M. Pessa, T. Ahlgren, and J. Decker, "Origin of improved luminescence efficiency after annealing of Ga(In)NAs materials grown by molecular-beam epitaxy," *Applied Physics Letters*, vol. 79, no. 8, pp. 1094–1096, 2001. [Online]. Available: http://scitation.aip.org/content/aip/journal/apl/79/8/10.1063/1.1396316.

[88] J. Toivonen, T. Hakkarainen, M. Sopanen, and H. Lipsanen, "Effect of post-growth laser treatment on optical properties of Ga(In)NAs quantum wells," *IEE Proceedings - Optoelectronics*, vol. 150, no. 1, pp. 68–71, Feb. 2003.

[89] X. Liu, M. Pistol, L. Samuelson, S. Schwetlick, and W. Seifert, "Nitrogen pair luminescence in GaAs," *Applied Physics Letters*, vol. 56, no. 15, pp. 1451–1453, 1990. [Online]. Available: http://scitation.aip.org/content/aip/journal/apl/56/15/10.1063/1.102495.

[90] B. A. Weinstein, S. R. Stambach, T. M. Ritter, J. O. Maclean, and D. J. Wallis, "Evidence for selective delocalization of N-pair states in dilute $GaAs_{1-x}N_x$," *Phys. Rev. B*, vol. 68, p. 035 336, 3 Jul. 2003. [Online]. Available: http://link.aps.org/doi/10.1103/PhysRevB.68.035336.

[91] M. Bissiri, G. Baldassarri Höger von Högersthal, A. Polimeni, V. Gaspari, F. Ranalli, M. Capizzi, A. A. Bonapasta, F. Jiang, M. Stavola, D. Gollub, M. Fischer, M. Reinhardt,

and A. Forchel, "Hydrogen-induced passivation of nitrogen in $GaAs_{1-y}N_y$," *Phys. Rev. B*, vol. 65, p. 235 210, 23 Jun. 2002. [Online]. Available: http://link.aps.org/doi/10.1103/PhysRevB.65.235210.

[92] M. Fukuda, V. R. Whiteside, J. C. Keay, A. Meleco, I. R. Sellers, K. Hossain, T. D. Golding, M. Leroux, and M. Al Khalfioui, "Improved performance in GaInNAs solar cells by hydrogen passivation," *Applied Physics Letters*, vol. 106, no. 14, 141904, p. 141 904, 2015. [Online]. Available: http://scitation.aip.org/content/aip/journal/apl/106/14/10.1063/1.4916668.

[93] A Polimeni, G. B. H. von Hogersthal, M Bissiri, M Capizzi, A Frova, M Fischer, M Reinhardt, and A Forchel, "Role of hydrogen in III-N-V compound semiconductors," *Semiconductor Science and Technology*, vol. 17, no. 8, p. 797, 2002. [Online]. Available: http://stacks.iop.org/0268-1242/17/i=8/a=308.

[94] R. Kudrawiec, M. Latkowska, M. Welna, J. Misiewicz, M. Shafi, R. H. Mari, M. Henini, and W. Walukiewicz, "Correlations between the band structure, activation energies of electron traps, and photoluminescence in n-type GaNAs layers," *Applied Physics Letters*, vol. 101, no. 8, p. 082 109, 2012. [Online]. Available: http://dx.doi.org/10.1063/1.4747504.

[95] D. B. Jackrel, S. R. Bank, H. B. Yuen, M. A. Wistey, J. S. Harris, A. J. Ptak, S. W. Johnston, D. J. Friedman, and S. R. Kurtz, "Dilute nitride GaInNAs and GaInNAsSb solar cells by molecular beam epitaxy," *Journal of Applied Physics*, vol. 101, no. 11, 114916, p. 114 916, 2007. [Online]. Available: http://scitation.aip.org/content/aip/journal/jap/101/11/10.1063/1.2744490.

[96] A. Janotti, S. B. Zhang, S.-H. Wei, and C. G. Van de Walle, "Effects of hydrogen on the electronic properties of dilute GaAsN alloys," *Phys. Rev. Lett.*, vol. 89, p. 086 403, 8 Aug. 2002. [Online]. Available: http://link.aps.org/doi/10.1103/PhysRevLett.89.086403.

[97] A. Janotti, S.-H. Wei, S. B. Zhang, S. Kurtz, and C. G. Van de Walle, "Interactions between nitrogen, hydrogen, and gallium vacancies in $GaAs_{1-x}N_x$ alloys," *Phys. Rev. B*, vol. 67, p. 161 201, 16 Apr. 2003. [Online]. Available: http://link.aps.org/doi/10.1103/PhysRevB.67.161201.

[98] S. Kurtz, J. F. Geisz, D. J. Friedman, W. K. Metzger, R. R. King, and N. H. Karam, "Annealing-induced-type conversion of GaInNAs," *Journal of Applied Physics*, vol. 95, no. 5, pp. 2505–2508, 2004. [Online]. Available: http://scitation.aip.org/content/aip/journal/jap/95/5/10.1063/1.1643775.

[99] A Polimeni and A Capizzi, "Role of hydrogen in dilute nitrides," in *Physics and Applications of Dilute Nitrides*, ser. Optoelectronic Properties of Semiconductors and Superlattice, I. Buyanova and W. Chen, Eds., Taylor & Francis, 2004, ch. 6, p. 166. [Online]. Available: https://books.google.com/books?id=7YL6gB_GKu0C.

[100] M. Fukuda, V. R. Whiteside, J. C. Keay, M. A. Khalfioui, M. Leroux, K. Hossain, T. D. Golding, and I. R. Sellers, "Improved performance of GaInNAs solar cell after UV-activated hydrogenation," in *Photovoltaic Specialist Conference (PVSC), 2015 IEEE 42nd*, Jun. 2015, pp. 1–3.

[101] S. R. Bank, H. B. Yuen, H. Bae, M. A. Wistey, and J. S. Harris, "Overannealing effects in GaInNAs(Sb) alloys and their importance to laser applications," *Applied*

Physics Letters, vol. 88, no. 22, 221115, p. 221 115, 2006. [Online]. Available: http://scitation.aip.org/content/aip/journal/apl/88/22/10.1063/1.2208375.

[102] O. W. Holland, R. J. Cottier, T. D. Golding, K. Hossain, and R. P. Hellmer, "Photolytic process of materials with hydrogen," *U.S. patent 9,196,497*, 24 November 2015.

[103] S. Mazzucato, R. Potter, A. Erol, N. Balkan, P. Chalker, T. Joyce, T. Bullough, X. Marie, H. Carrère, E. Bedel, G. Lacoste, A. Arnoult, and C. Fontaine, "S-shaped behaviour of the temperature-dependent energy band gap in dilute nitrides," *Physica E: Low-dimensional Systems and Nanostructures*, vol. 17, pp. 242 –244, 2003, Proceedings of the International Conference on Superlattices, Nano-structures and Nano-devices {ICSNN} 2002 o-structures and Nano-devices {ICSNN} 2002. [Online]. Available: http://www.sciencedirect.com/science/article/pii/S138694770200783X.

[104] T. Nuytten, M. Hayne, B. Bansal, H. Y. Liu, M. Hopkinson, and V. V. Moshchalkov, "Charge separation and temperature-induced carrier migration in $Ga_{1-x}In_xN_yAs_{1-y}$ multiple quantum wells," *Phys. Rev. B*, vol. 84, p. 045 302, 4 Jul. 2011. [Online]. Available: http://link.aps.org/doi/10.1103/PhysRevB.84.045302.

[105] J. Tang, V. R. Whiteside, H. Esmaielpour, S. Vijeyaragunathan, T. D. Mishima, M. B. Santos, and I. R. Sellers, "Effects of localization on hot carriers in $InAs/AlAs_xSb_{1-x}$ quantum wells," *Applied Physics Letters*, vol. 106, no. 6, 061902, p. 061 902, 2015, Errata: **107**, 049902, (2015). [Online]. Available: http://scitation.aip.org/content/aip/journal/apl/106/6/10.1063/1.4907630.

[106] C. Weisbuch and B. Vinter, *Quantum Semiconductor Structures: Fundamentals and Applications*. Academic Press, 1991. [Online]. Available: https://books.google.com/books?id=iCgWvw5ZpRQC.

[107] Y. Cheng, M. Fukuda, V. R. Whiteside, M. C. Debnath, P. J. Vallely, T. D. Mishima, M. B. Santos, K. Hossain, S. Hatch, H. Y. Liu, and I. R. Sellers, "Investigation of InAs/$GaAs_{1-x}Sb_x$ quantum dots for applications in intermediate band solar cells," *Solar Energy Materials and Solar Cells*, vol. 147, pp. 94 –100, 2016. [Online]. Available: http://www.sciencedirect.com/science/article/pii/S092702481500639X.

[108] P. R. C. Kent and A. Zunger, "Failure of nitrogen cluster states to emerge into the bandgap of GaAsN with application of pressure," *Applied Physics Letters*, vol. 82, no. 4, pp. 559–561, 2003. [Online]. Available: http://dx.doi.org/10.1063/1.1539543.

[109] A. Lindsay and E. P. O'Reilly, "Unification of the band anticrossing and cluster-state models of dilute nitride semiconductor alloys," *Phys. Rev. Lett.*, vol. 93, p. 196 402, 19 Nov. 2004. [Online]. Available: http://link.aps.org/doi/10.1103/PhysRevLett.93.196402.

[110] Y. Tsai, B. Barman, T. Scrace, M. Fukuda, V. R. Whiteside, I. R. Sellers, M. Leroux, M. A. Khalfioui, and A. Petrou, "Photoluminescence study of Be-acceptors in GaInNAs epilayers," *Journal of Applied Physics*, vol. 117, no. 4, 045705, p. 045 705, 2015.

[111] F. Willmann, W. Dreybrodt, M. Bettini, E. Bauser, and D. Bimberg, "GaAs luminescence transitions to acceptors in magnetic fields," *physica status solidi (b)*, vol. 60, no. 2, pp. 751–759, 1973. [Online]. Available: http://dx.doi.org/10.1002/pssb.2220600231.

[112] S. Shirakata, M. Kondow, and T. Kitatani, "Raman studies of lattice and local vibrational modes of GaInNAs prepared by molecular beam epitaxy," *Journal of Physics and Chemistry of Solids*, vol. 66, no. 11, pp. 2119 –2122, 2005, The 14th International Conference on Ternary and Multinary Compounds. [Online]. Available: http://www.sciencedirect.com/science/article/pii/S0022369705003914.

[113] A. Pusch, M. Yoshida, N. P. Hylton, A. Mellor, C. C. Phillips, O. Hess, and N. J. Ekins-Daukes, "Limiting efficiencies for intermediate band solar cells with partial absorptivity: The case for a quantum ratchet," *Progress in Photovoltaics: Research and Applications*, vol. 24, no. 5, pp. 656–662, 2016, pip.2751. [Online]. Available: http://dx.doi.org/10.1002/pip.2751.

[114] T. Mou, S. Li, C. R. Brown, V. R. Whiteside, K. Hossain, M. Al Khalfioui, M. Leroux, I. R. Sellers, and B. Wang, "Role of In in hydrogenation of N-related complexes in GaInNAs," *ACS Applied Electronic Materials*, vol. 1, no. 4, pp. 461–466, 2019. [Online]. Available: https://doi.org/10.1021/acsaelm.9b00041.

[115] M. Hugues, B. Damilano, J.-Y. Duboz, and J. Massies, "Exciton dissociation and hole escape in the thermal photoluminescence quenching of $(Ga, In)(N, As)$ quantum wells," *Phys. Rev. B*, vol. 75, p. 115 337, 11 Mar. 2007. [Online]. Available: https://link.aps.org/doi/10.1103/PhysRevB.75.115337.

[116] J. Allen, V. Sabnis, M. Wiemer, and H. Yuen, "44%-efficiency triple-junction solar cells," in *Proceedings of 9th International Conference on Concentrator Photovoltaic Systems*, Apr. 2013.

[117] C. R. Brown, N. J. Estes, V. R. Whiteside, B. Wang, K. Hossain, T. D. Golding, M. Leroux, M. Al Khalfioui, J. G. Tischler, C. T. Ellis, E. R. Glaser, and I. R. Sellers, "The effect and nature of N-H complexes in the control of the dominant photoluminescence transitions in UV-hydrogenated GaInNAs," *RSC Advances*, vol. 7, no. 41, pp. 25 353–25 361, 2017. [Online]. Available: http://dx.doi.org/10.1039/C7RA02900D.

[118] G. Sun, J. Kürti, P. Rajczy, M. Kertesz, J. Hafner, and G. Kresse, "Performance of the vienna ab initio simulation package (VASP) in chemical applications," *Journal of Molecular Structure: {THEOCHEM}*, vol. 624, no. 1â€"3, pp. 37 –45, 2003. [Online]. Available: http://www.sciencedirect.com/science/article/pii/S0166128002007339.

[119] J. Heyd, G. E. Scuseria, and M. Ernzerhof, "Hybrid functionals based on a screened coulomb potential," *The Journal of Chemical Physics*, vol. 118, no. 18, pp. 8207–8215, 2003, Errata: **124**, 219906, (2006). [Online]. Available: http://scitation.aip.org/content/aip/journal/jcp/118/18/10.1063/1.1564060.

[120] S. Kurtz, R. King, D. Law, A. Ptak, J. Geisz, and N. Karam, "Effects of in situ annealing on GaInNAs solar cells," in *2013 IEEE 39th Photovoltaic Specialists Conference (PVSC)*, Jun. 2013, pp. 2095–2099.

[121] M. Latkowska, R. Kudrawiec, G. Sęk, J. Misiewicz, J. Ibáñez, M. Henini, and M. Hopkinson, "Thermal quenching of single localized excitons in GaInNAs layers," *Applied Physics Letters*, vol. 98, no. 13, p. 131 903, 2011. [Online]. Available: https://doi.org/10.1063/1.3571287.

[122] Y. Tsai, B. Barman, T. Scrace, G. Lindberg, M. Fukuda, V. R. Whiteside, J. C. Keay, M. B. Johnson, I. R. Sellers, M. Al Khalfioui, M. Leroux, B. A. Weinstein, and A. Petrou, "Probing the nature of carrier localization in GaInNAs epilayers by optical methods," *Applied Physics Letters*, vol. 103, no. 1, p. 012 104, 2013. [Online]. Available: https://doi.org/10.1063/1.4813388.

[123] A Stampfl, G Kemister, R. C. G. Leckey, J. D. Riley, P. J. Orders, B Usher, F. U. Hillebrecht, and L Ley, "Effect of strain on the band structure of InGaAs," *Physica Scripta*, vol. 41, no. 4, pp. 617–620, Apr. 1990. [Online]. Available: https://doi.org/10.1088%2F0031-8949%2F41%2F4%2F053.

[124] H. Afshari, B. K. Durant, D. Y. Kim, S. Chan, J. McNatt, H. Liu, and I. R. Sellers, "An irradiation and LILT effect study on InAs/GaAsSb quantum dot solar cells," *In Preparation*, 2019.

[125] P. Jackson, D. Hariskos, E. Lotter, S. Paetel, R. Wuerz, R. Menner, W. Wischmann, and M. Powalla, "New world record efficiency for Cu(In,Ga)Se_2 thin-film solar cells beyond 20%," *Progress in Photovoltaics: Research and Applications*, vol. 19, no. 7, pp. 894–897, 2011. [Online]. Available: https://doi.org/10.1002/pip.1078.

[126] P. Jackson, R. Wuerz, D. Hariskos, E. Lotter, W. Witte, and M. Powalla, "Effects of heavy alkali elements in Cu(In,Ga)Se_2 solar cells with efficiencies up to 22.6%," *physica status solidi (RRL) – Rapid Research Letters*, vol. 10, no. 8, pp. 583–586, 2016. [Online]. Available: http://dx.doi.org/10.1002/pssr.201600199.

[127] R. Scheer and H.-W. Schock, "Thin film heterostructures," in *Chalcogenide Photovoltaics*. Wiley-VCH Verlag GmbH & Co. KGaA, 2011, pp. 9–127. [Online]. Available: http://dx.doi.org/10.1002/9783527633708.ch2.

[128] T. Feurer, P. Reinhard, E. Avancini, B. Bissig, J. Löckinger, P. Fuchs, R. Carron, T. P. Weiss, J. Perrenoud, S. Stutterheim, S. Buecheler, and A. N. Tiwari, "Progress in thin film cigs photovoltaics - research and development, manufacturing, and applications," *Progress in Photovoltaics: Research and Applications*, vol. 25, no. 7, pp. 645–667, 2017. [Online]. Available: http://dx.doi.org/10.1002/pip.2811.

[129] U. Rau and H. Schock, "Electronic properties of Cu(In,Ga)Se_2 heterojunction solar cells - recent achievements, current understanding, and future challenges," *Applied Physics A*, vol. 69, no. 2, pp. 131–147, 1999. [Online]. Available: https://doi.org/10.1007/s003390050984.

[130] K. Ramanathan, M. A. Contreras, C. L. Perkins, S. Asher, F. S. Hasoon, J. Keane, D. Young, M. Romero, W. Metzger, R. Noufi, J. Ward, and A. Duda, "Properties of 19.2% efficiency ZnO/CdS/CuInGaSe_2 thin-film solar cells," *Progress in Photovoltaics: Research and Applications*, vol. 11, no. 4, pp. 225–230, 2003. [Online]. Available: http://dx.doi.org/10.1002/pip.494.

[131] S. Lany and A. Zunger, "Intrinsic DX centers in ternary chalcopyrite semiconductors," *Physical Review Letters*, vol. 100, no. 1, p. 016 401, 2008. [Online]. Available: https://link.aps.org/doi/10.1103/PhysRevLett.100.016401.

[132] S. B. Zhang, S.-H. Wei, A. Zunger, and H. Katayama-Yoshida, "Defect physics of the $CuInSe_2$ chalcopyrite semiconductor," *Physical Review B*, vol. 57, no. 16, pp. 9642–9656, 1998. [Online]. Available: http://link.aps.org/doi/10.1103/PhysRevB.57.9642.

[133] M. Köntges, R. Reineke-Koch, P. Nollet, J. Beier, R. Schäffler, and J. Parisi, "Light induced changes in the electrical behavior of CdTe and $Cu(In,Ga)Se_2$ solar cells," *Thin Solid Films*, vol. 403-404, no. Supplement C, pp. 280–286, 2002. [Online]. Available: http://www.sciencedirect.com/science/article/pii/S0040609001015073.

[134] S. Lany and A. Zunger, "Light- and bias-induced metastabilities in $Cu(In,Ga)Se_2$ based solar cells caused by the (V_{Se}-V_{Cu}) vacancy complex," *Journal of Applied Physics*, vol. 100, no. 11, p. 113 725, 2006. [Online]. Available: http://aip.scitation.org/doi/abs/10.1063/1.2388256.

[135] M. Igalson, M. Cwil, and M. Edoff, "Metastabilities in the electrical characteristics of CIGS devices: Experimental results vs theoretical predictions," *Thin Solid Films*, vol. 515, no. 15, pp. 6142–6146, 2007. [Online]. Available: http://www.sciencedirect.com/science/article/pii/S0040609006015690.

[136] M. Igalson, P. Zabierowski, D. Prządo, A. Urbaniak, M. Edoff, and W. N. Shafarman, "Understanding defect-related issues limiting efficiency of CIGS solar cells," *Solar Energy Materials and Solar Cells*, vol. 93, no. 8, pp. 1290–1295, 2009. [Online]. Available: http://www.sciencedirect.com/science/article/pii/S0927024809000403.

[137] A. Urbaniak and M. Igalson, "Creation and relaxation of light- and bias-induced metastabilities in $Cu(In,Ga)Se_2$," *Journal of Applied Physics*, vol. 106, no. 6, p. 063 720, 2009. [Online]. Available: https://doi.org/10.1063/1.3213339.

[138] M. Igalson, M. Pawłowski, and D. Prządo, "Influence of electric field on photoluminescence of Cu(In,Ga)Se_2-based solar cells," *Opto-Electronics Review*, vol. 19, no. 4, p. 435, 2011. [Online]. Available: https://doi.org/10.2478/s11772-011-0037-z.

[139] R. Farshchi, B. Hickey, G. Zapalac, J. Bailey, D. Spaulding, and D. Poplavskyy, "Mechanisms for light-soaking induced carrier concentration changes in the absorber layer of Cu(In,Ga)Se_2 solar cells," in *2016 IEEE 43rd Photovoltaic Specialists Conference (PVSC)*, 2016, pp. 2157–2160.

[140] T. Eisenbarth, T. Unold, R. Caballero, C. A. Kaufmann, and H.-W. Schock, "Interpretation of admittance, capacitance-voltage, and current-voltage signatures in Cu(In,Ga)Se_2 thin film solar cells," *Journal of Applied Physics*, vol. 107, no. 3, p. 034 509, 2010. [Online]. Available: https://doi.org/10.1063/1.3277043.

[141] A. Niemegeers, M. Burgelman, R. Herberholz, U. Rau, D. Hariskos, and H.-W. Schock, "Model for electronic transport in Cu(In,Ga)Se_2 solar cells," *Progress in Photovoltaics: Research and Applications*, vol. 6, no. 6, pp. 407–421, 1998.

[142] A. Jasenek, U. Rau, K. Weinert, I. Kötschau, G. Hanna, G. Voorwinden, M. Powalla, H. Schock, and J. Werner, "Radiation resistance of Cu(In,Ga)Se_2 solar cells under 1-MeV electron irradiation," *Thin Solid Films*, vol. 387, no. 1, pp. 228 –230, 2001, Proceeedings of Symposium N on Thin Film Photovoltaicmaterials of the E-MRS Spring Conference. [Online]. Available: http://www.sciencedirect.com/science/article/pii/S0040609000018472.

[143] S. Kawakita, M. Imaizumi, M. Yamaguchi, K. Kushiya, T. Ohshima, H. Itoh, and S. Matsuda, "Annealing enhancement effect by light illumination on proton irradiated

Cu(In,Ga)Se_2 thin-film solar cells," *Japanese Journal of Applied Physics*, vol. 41, no. 7A, p. L797, 2002. [Online]. Available: http://stacks.iop.org/1347-4065/41/i=7A/a=L797.

[144] S. Kawakita, M. Imaizumi, T. Sumita, K. Kushiya, T. Ohshima, M. Yamaguchi, S. Matsuda, S. Yoda, and T. Kamiya, "Super radiation tolerance of CIGS solar cells demonstrated in space by MDS-1 satellite," in *3rd World Conference on Photovoltaic Energy Conversion, 2003. Proceedings of*, vol. 1, 2003, 693–696 Vol.1. [Online]. Available: https://ieeexplore.ieee.org/document/1305376/.

[145] L. C. Hirst, M. K. Yakes, J. H. Warner, M. F. Bennett, K. J. Schmieder, R. J. Walters, and P. P. Jenkins, "Intrinsic radiation tolerance of ultra-thin GaAs solar cells," *Applied Physics Letters*, vol. 109, no. 3, p. 033 908, 2016. [Online]. Available: http://aip.scitation.org/doi/abs/10.1063/1.4959784.

[146] N. Mackie, R. Tas, J. Corson, and A. Bayman, "A different approach: CIGS using all PVD," in *28th European Photovoltaic Solar Energy Conference and Exhibition*, 2013.

[147] M Burgelman, P Nollet, and S Degrave, "Modelling polycrystalline semiconductor solar cells," *Thin Solid Films*, vol. 361-362, pp. 527 –532, 2000. [Online]. Available: http://www.sciencedirect.com/science/article/pii/S0040609099008251.

[148] S. A. Jensen, S. Glynn, A. Kanevce, P. Dippo, J. V. Li, D. H. Levi, and D. Kuciauskas, "Beneficial effect of post-deposition treatment in high-efficiency Cu(In,Ga)Se_2 solar cells through reduced potential fluctuations," *Journal of Applied Physics*, vol. 120, no. 6, p. 063 106, 2016. [Online]. Available: https://doi.org/10.1063/1.4960344.

[149] S. A. Jensen, P. Dippo, L. M. Mansfield, S. Glynn, and D. Kuciauskas, "Defect states in copper indium gallium selenide solar cells from two-wavelength excitation photoluminescence spectroscopy," in *2016 IEEE 43rd Photovoltaic Specialists Conference (PVSC)*, 2016, pp. 3556–3558.

[150] M. J. Romero, H. Du, G. Teeter, Y. Yan, and M. M. Al-Jassim, "Comparative study of the luminescence and intrinsic point defects in the kesterite Cu_2ZnSnS_4 and chalcopyrite Cu(In,Ga)Se_2 thin films used in photovoltaic applications," *Physical Review B*, vol. 84, no. 16, p. 165 324, 2011. [Online]. Available: https://link.aps.org/doi/10.1103/PhysRevB.84.165324.

[151] J. P. Teixeira, R. A. Sousa, M. G. Sousa, A. F. da Cunha, P. A. Fernandes, P. M. P. Salomé, and J. P. Leitão, "Radiative transitions in highly doped and compensated chalcopyrites and kesterites: The case of Cu_2ZnSnS_4," *Physical Review B*, vol. 90, no. 23, p. 235 202, 2014. [Online]. Available: https://link.aps.org/doi/10.1103/PhysRevB.90.235202.

[152] A. Hultqvist, J. V. Li, D. Kuciauskas, P. Dippo, M. A. Contreras, D. H. Levi, and S. F. Bent, "Reducing interface recombination for Cu(In,Ga)Se_2 by atomic layer deposited buffer layers," *Applied Physics Letters*, vol. 107, no. 3, p. 033 906, 2015. [Online]. Available: http://aip.scitation.org/doi/abs/10.1063/1.4927096.

[153] T. Sakurai, K. Taguchi, M. M. Islam, S. Ishizuka, A. Yamada, K. Matsubara, S. Niki, and K. Akimoto, "Time-resolved microphotoluminescence study of Cu(In,Ga)Se_2," *Japanese Journal of Applied Physics*, vol. 50, no. 5S2, 05FC01, 2011. [Online]. Available: http://stacks.iop.org/1347-4065/50/i=5S2/a=05FC01.

[154] F. Luckert, M. V. Yakushev, C. Faugeras, A. V. Karotki, A. V. Mudryi, and R. W. Martin, "Excitation power and temperature dependence of excitons in $CuInSe_2$," *Journal of Applied Physics*, vol. 111, no. 9, p. 093 507, 2012. [Online]. Available: https://doi.org/10.1063/1.4709448.

[155] H. Lee, Y. Jang, S.-W. Nam, C. Jung, P.-P. Choi, J. Gwak, J. H. Yun, K. Kim, and B. Shin, "Passivation of deep-level defects by cesium fluoride post-deposition treatment for improved device performance of $Cu(In,Ga)Se_2$ solar cells," *ACS Applied Materials & Interfaces*, vol. 11, no. 39, pp. 35 653–35 660, 2019, PMID: 31525944. [Online]. Available: https://doi.org/10.1021/acsami.9b08316.

[156] J. Yang, H. W. Du, Y. Li, M. Gao, Y. Z. Wan, F. Xu, and Z. Q. Ma, "Structural defects and recombination behavior of excited carriers in $Cu(In,Ga)Se_2$ solar cells," *AIP Advances*, vol. 6, no. 8, p. 085 215, 2016. [Online]. Available: https://doi.org/10.1063/1.4961701.

[157] J. Chantana, D. Hironiwa, T. Watanabe, S. Teraji, and T. Minemoto, "Flexible $Cu(In,Ga)Se_2$ solar cell on stainless steel substrate deposited by multi-layer precursor method: Its photovoltaic performance and deep-level defects," *Progress in Photovoltaics: Research and Applications*, vol. 24, no. 7, pp. 990–1000, 2016. [Online]. Available: https://onlinelibrary.wiley.com/doi/abs/10.1002/pip.2748.

[158] T. Eisenbarth, R. Caballero, C. A. Kaufmann, A. Eicke, and T. Unold, "Influence of iron on defect concentrations and device performance for $Cu(In,Ga)Se_2$ solar cells on stainless steel substrates," *Progress in Photovoltaics: Research and Applications*,

vol. 20, no. 5, pp. 568–574, 2012. [Online]. Available: https://onlinelibrary.wiley.com/doi/abs/10.1002/pip.2260.

[159] J. Yang, D. Chen, F. Xu, and Z. Ma, "Photoluminescence study of the defect-induced recombination in Cu(In,Ga)Se_2 solar cell," *Solar Energy*, vol. 98, pp. 415 –421, 2013. [Online]. Available: http://www.sciencedirect.com/science/article/pii/S0038092X13003897.

[160] K.-J. Hsiao, J.-D. Liu, H.-H. Hsieh, and T.-S. Jiang, "Electrical impact of $MoSe_2$ on CIGS thin-film solar cells," *Phys. Chem. Chem. Phys.*, vol. 15, pp. 18 174–18 178, 41 2013. [Online]. Available: http://dx.doi.org/10.1039/C3CP53310G.

[161] A. Bauknecht, S. Siebentritt, J. Albert, and M. C. Lux-Steiner, "Radiative recombination via intrinsic defects in CuxGaySe2," *Journal of Applied Physics*, vol. 89, no. 8, pp. 4391–4400, 2001. [Online]. Available: https://doi.org/10.1063/1.1357786.

[162] R. Farshchi, B. Hickey, and D. Poplavskyy, "Light-soak and dark-heat induced changes in Cu(In,Ga)Se_2 solar cells: A macroscopic to microscopic study," in *2017 IEEE 44th Photovoltaic Specialists Conference (PVSC)*, 2017.

[163] R. Farshchi and D. Poplavskyy, "Impact of growth temperature and selenization on dark heat stability in Cu(In,Ga)Se_2 solar cells," in *2018 IEEE 45th Photovoltaic Specialists Conference (PVSC)*, 2018.

[164] G. Sozzi, S. D. Napoli, R. Menozzi, F. Werner, S. Siebentritt, P. Jackson, and W. Witte, "Influence of conduction band offsets at window/buffer and buffer/absorber interfaces on the roll-over of J-V curves of CIGS solar cells," in *2018 IEEE 45th Photovoltaic Specialists Conference (PVSC)*, 2018.

[165] C. P. Thompson, S. Hegedus, W. Shafarman, and D. Desai, "Temperature dependence of Voc in CdTe and Cu(In,Ga)Se_2-based solar cells," in *2008 33rd IEEE Photovoltaic Specialists Conference*, 2008, pp. 1–6.

[166] M. Maciaszek and P. Zabierowski, "Influence of relaxation processes on the evaluation of the metastable defect density in Cu(In,Ga)Se_2," *Journal of Applied Physics*, vol. 119, no. 21, p. 215 103, 2016. [Online]. Available: `https://doi.org/10.1063/1.4953145`.

[167] S. Lany and A. Zunger, "Limitation of the open-circuit voltage due to metastable intrinsic defects in Cu(In,Ga)Se_2 and strategies to avoid these defects," in *2008 33rd IEEE Photovoltaic Specialists Conference*, 2008, pp. 1–3.

[168] M. E. Stuckelberger, T. Nietzold, B. M. West, R. Farshchi, D. Poplavskyy, J. Bailey, B. Lai, J. M. Maser, and M. I. Bertoni, "How does CIGS performance depend on temperature at the microscale?" *IEEE Journal of Photovoltaics*, vol. 8, no. 1, pp. 278–287, 2018.

[169] F. Werner, M. H. Wolter, S. Siebentritt, G. Sozzi, S. Di Napoli, R. Menozzi, P. Jackson, W. Witte, R. Carron, E. Avancini, T. P. Weiss, and S. Buecheler, "Alkali treatments of Cu(In,Ga)Se_2 thin-film absorbers and their impact on transport barriers," *Progress in Photovoltaics: Research and Applications*, pp. 1–13, 2018. [Online]. Available: `https://doi.org/10.1002/pip.3032`.

[170] A. Ferguson, P. Dippo, D. Kuciauskas, R. Farshchi, J. Bailey, G. Zapalac, and D. Poplavskyy, "Optical spectroscopic probes of degradation and metastability in polycrystalline (Ag,Cu)(In,Ga)Se_2 absorbers," in *2018 IEEE 45th Photovoltaic Specialists Conference (PVSC)*, 2018.

[171] C. R. Brown, V. R. Whiteside, D. Poplavskyy, K. Hossain, M. S. Dhoubhadel, and I. R. Sellers, "Flexible Cu(In,Ga)Se_2 solar cells for outer planetary missions: Investigation under low-intensity low-temperature conditions," *IEEE Journal of Photovoltaics*, vol. 9, no. 2, pp. 552–558, Mar. 2019.

[172] J. J. Loferski, "The effects of electron and proton irradiation on thin film solar cells," *Revue de Physique Appliquee*, vol. 1, no. 3, pp. 221–227, 1966. [Online]. Available: https://hal.archives-ouvertes.fr/jpa-00242721.

[173] J. Huang, Y. Yuan, Y. Shao, and Y. Yan, "Understanding the physical properties of hybrid perovskites for photovoltaic applications," *Nature Reviews Materials*, vol. 2, p. 17 042, 2017. [Online]. Available: http://dx.doi.org/10.1038/natrevmats.2017.42.

[174] M. Saliba, T. Matsui, J.-Y. Seo, K. Domanski, J.-P. Correa-Baena, M. K. Nazeeruddin, S. M. Zakeeruddin, W. Tress, A. Abate, A. Hagfeldt, and M. Grätzel, "Cesium-containing triple cation perovskite solar cells: Improved stability, reproducibility and high efficiency," *Energy & Environmental Science*, vol. 9, no. 6, pp. 1989–1997, 2016. [Online]. Available: http://dx.doi.org/10.1039/C5EE03874J.

[175] J. A. Christians, P. Schulz, J. S. Tinkham, T. H. Schloemer, S. P. Harvey, B. J. Tremolet de Villers, A. Sellinger, J. J. Berry, and J. M. Luther, "Tailored interfaces of unencapsulated perovskite solar cells for >1,000 hour operational stability," *Nature Energy*, vol. 3, no. 1, pp. 68–74, 2018. [Online]. Available: https://doi.org/10.1038/s41560-017-0067-y.

[176] F. Lang, N. H. Nickel, J. Bundesmann, S. Seidel, A. Denker, S. Albrecht, V. V. Brus, J. Rappich, B. Rech, G. Landi, and H. C. Neitzert, "Radiation hardness and self-healing of perovskite solar cells," *Advanced Materials*, vol. 28, no. 39, pp. 8726–8731, 2016. [Online]. Available: https://doi.org/10.1002/adma.201603326.

[177] F. Lang, O. Shargaieva, V. V. Brus, H. C. Neitzert, J. Rappich, and N. H. Nickel, "Influence of radiation on the properties and the stability of hybrid perovskites," *Advanced Materials*, vol. 30, no. 3, p. 1 702 905, 2017. [Online]. Available: https://doi.org/10.1002/adma.201702905.

[178] Y. Miyazawa, M. Ikegami, H.-W. Chen, T. Ohshima, M. Imaizumi, K. Hirose, and T. Miyasaka, "Tolerance of perovskite solar cell to high-energy particle irradiations in space environment," *iScience*, vol. 2, pp. 148–155, 2018. [Online]. Available: http://www.sciencedirect.com/science/article/pii/S2589004218300294.

[179] F. Lang, M. Jošt, J. Bundesmann, A. Denker, S. Albrecht, G. Landi, H.-C. Neitzert, J. Rappich, and N. H. Nickel, "Efficient minority carrier detrapping mediating the radiation hardness of triple-cation perovskite solar cells under proton irradiation," *Energy Environ. Sci.*, vol. 12, pp. 1634–1647, 5 2019. [Online]. Available: http://dx.doi.org/10.1039/C9EE00077A.

[180] J. Yoon, H. Sung, G. Lee, W. Cho, N. Ahn, H. S. Jung, and M. Choi, "Superflexible, high-efficiency perovskite solar cells utilizing graphene electrodes: Towards future foldable power sources," *Energy Environ. Sci.*, vol. 10, pp. 337–345, 1 2017. [Online]. Available: http://dx.doi.org/10.1039/C6EE02650H.

[181] L. Li, S. Zhang, Z. Yang, E. E. S. Berthold, and W. Chen, "Recent advances of flexible perovskite solar cells," *Journal of Energy Chemistry*, vol. 27, no. 3, pp. 673 –689, 2018. [Online]. Available: http://www.sciencedirect.com/science/article/pii/S2095495617309221.

[182] L. Johnson and J. A. Carr, "Deployable propulsion and power systems for solar system exploration," in *38th IEEE Aerospace Sciences Conference*, 2017. [Online]. Available: https://ntrs.nasa.gov/archive/nasa/casi.ntrs.nasa.gov/20170003413.pdf.

[183] L. Johnson, J. A. Carr, and D. Boyd, "The Lightweight Integrated Solar Array and anTenna (LISA-T) - big power for small spacecraft," in *68th International Astronautical Congress*, 2017. [Online]. Available: https://ntrs.nasa.gov/archive/nasa/casi.ntrs.nasa.gov/20170009097.pdf.

[184] S. Richey and B. Hine, "Mission design for deep space CubeSats," in *NASA Centennial CubeQuest Challenge*, 2017. [Online]. Available: https://ntrs.nasa.gov/archive/nasa/casi.ntrs.nasa.gov/20170010358.pdf.

[185] C. R. Brown, G. E. Eperon, V. R. Whiteside, and I. R. Sellers, "Potential of high-stability perovskite solar cells for low-intensity-low-temperature (LILT) outer planetary space missions," *ACS Applied Energy Materials*, vol. 2, no. 1, pp. 814–821, 2019. [Online]. Available: https://doi.org/10.1021/acsaem.8b01882.

[186] X. Chen, H. Lu, Y. Yang, and M. C. Beard, "Excitonic effects in methylammonium lead halide perovskites," *The Journal of Physical Chemistry Letters*, vol. 9, no. 10, pp. 2595–2603, 2018. [Online]. Available: https://doi.org/10.1021/acs.jpclett.8b00526.

[187] V. D'Innocenzo, G. Grancini, M. J. P. Alcocer, A. R. S. Kandada, S. D. Stranks, M. M. Lee, G. Lanzani, H. J. Snaith, and A. Petrozza, "Excitons versus free charges in organo-lead tri-halide perovskites," *Nature Communications*, vol. 5, p. 3586, 2014. [Online]. Available: http://dx.doi.org/10.1038/ncomms4586.

[188] J. Even, L. Pedesseau, and C. Katan, "Analysis of multivalley and multibandgap absorption and enhancement of free carriers related to exciton screening in hybrid perovskites," *The Journal of Physical Chemistry C*, vol. 118, no. 22, pp. 11 566–11 572, 2014. [Online]. Available: https://doi.org/10.1021/jp503337a.

[189] Z. Xiao and Y. Yan, "Progress in theoretical study of metal halide perovskite solar cell materials," *Advanced Energy Materials*, vol. 7, no. 22, p. 1 701 136, 2017. [Online]. Available: https://onlinelibrary.wiley.com/doi/abs/10.1002/aenm.201701136.

[190] R. L. Milot, G. E. Eperon, H. J. Snaith, M. B. Johnston, and L. M. Herz, "Temperature-dependent charge-carrier dynamics in $CH_3NH_3PbI_3$ perovskite thin films," *Advanced Functional Materials*, vol. 25, no. 39, pp. 6218–6227, 2015. [Online]. Available: https://onlinelibrary.wiley.com/doi/abs/10.1002/adfm.201502340.

[191] A. D. Wright, C. Verdi, R. L. Milot, G. E. Eperon, M. A. Pérez-Osorio, H. J. Snaith, F. Giustino, M. B. Johnston, and L. M. Herz, "Electron-phonon coupling in hybrid lead halide perovskites," *Nature Communications*, vol. 7, p. 11 755, 2016. [Online]. Available: http://dx.doi.org/10.1038/ncomms11755.

[192] C. C. Stoumpos, C. D. Malliakas, and M. G. Kanatzidis, "Semiconducting tin and lead iodide perovskites with organic cations: Phase transitions, high mobilities, and

near-infrared photoluminescent properties," *Inorganic Chemistry*, vol. 52, no. 15, pp. 9019–9038, 2013. [Online]. Available: https://doi.org/10.1021/ic401215x.

[193] H. Zhang, X. Qiao, Y. Shen, T. Moehl, S. M. Zakeeruddin, M. Grätzel, and M. Wang, "Photovoltaic behaviour of lead methylammonium triiodide perovskite solar cells down to 80 K," *Journal of Materials Chemistry A*, vol. 3, no. 22, pp. 11 762–11 767, 2015. [Online]. Available: http://dx.doi.org/10.1039/C5TA02206A.

[194] H. Esmaielpour, V. R. Whiteside, L. C. Hirst, J. G. Tischler, C. T. Ellis, M. P. Lumb, D. V. Forbes, R. J. Walters, and I. R. Sellers, "Effect of occupation of the excited states and phonon broadening on the determination of the hot carrier temperature from continuous wave photoluminescence in InGaAsP quantum well absorbers," *Progress in Photovoltaics: Research and Applications*, vol. 25, no. 9, pp. 782–790, 2017. [Online]. Available: https://onlinelibrary.wiley.com/doi/abs/10.1002/pip.2890.

[195] C. Wehrenfennig, M. Liu, H. J. Snaith, M. B. Johnston, and L. M. Herz, "Homogeneous emission line broadening in the organo lead halide perovskite $CH_3NH_3PbI_{3-x}Cl_x$," *The Journal of Physical Chemistry Letters*, vol. 5, no. 8, pp. 1300–1306, 2014. [Online]. Available: https://doi.org/10.1021/jz500434p.

[196] Y. Zou and R. J. Holmes, "Temperature-dependent bias poling and hysteresis in planar organo-metal halide perovskite photovoltaic cells," *Advanced Energy Materials*, vol. 6, no. 7, p. 1 501 994, 2016. [Online]. Available: https://doi.org/10.1002/aenm.201501994.

[197] H. J. Snaith, A. Abate, J. M. Ball, G. E. Eperon, T. Leijtens, N. K. Noel, S. D. Stranks, J. T.-W. Wang, K. Wojciechowski, and W. Zhang, "Anomalous hysteresis in perovskite

solar cells," *The Journal of Physical Chemistry Letters*, vol. 5, no. 9, pp. 1511–1515, 2014. [Online]. Available: https://doi.org/10.1021/jz500113x.

[198] S. N. Habisreutinger, N. K. Noel, and H. J. Snaith, "Hysteresis index: A figure without merit for quantifying hysteresis in perovskite solar cells," *ACS Energy Letters*, vol. 3, no. 10, pp. 2472–2476, 2018. [Online]. Available: https://doi.org/10.1021/acsenergylett.8b01627.

[199] I. Cardinaletti, T. Vangerven, S. Nagels, R. Cornelissen, D. Schreurs, J. Hruby, J. Vodnik, D. Devisscher, J. Kesters, J. D'Haen, A. Franquet, V. Spampinato, T. Conard, W. Maes, W. Deferme, and J. V. Manca, "Organic and perovskite solar cells for space applications," *Solar Energy Materials and Solar Cells*, vol. 182, pp. 121–127, 2018. [Online]. Available: http://www.sciencedirect.com/science/article/pii/S0927024818301272.

[200] H. Yu, H. Lu, F. Xie, S. Zhou, and N. Zhao, "Native defect-induced hysteresis behavior in organolead iodide perovskite solar cells," *Advanced Functional Materials*, vol. 26, no. 9, pp. 1411–1419, 2016. [Online]. Available: https://doi.org/10.1002/adfm.201504997.

[201] R. T. Ginting, E.-S. Jung, M.-K. Jeon, W.-Y. Jin, M. Song, and J.-W. Kang, "Low-temperature operation of perovskite solar cells: With efficiency improvement and hysteresis-less," *Nano Energy*, vol. 27, pp. 569–576, 2016. [Online]. Available: http://www.sciencedirect.com/science/article/pii/S2211285516303020.

[202] K. T. Cho, S. Paek, G. Grancini, C. Roldán-Carmona, P. Gao, Y. Lee, and M. K. Nazeeruddin, "Highly efficient perovskite solar cells with a compositionally engineered

perovskite/hole transporting material interface," *Energy & Environmental Science*, vol. 10, no. 2, pp. 621–627, 2017. [Online]. Available: http://dx.doi.org/10.1039/C6EE03182J.

[203] P. Calado, A. M. Telford, D. Bryant, X. Li, J. Nelson, B. C. O'Regan, and P. R. F. Barnes, "Evidence for ion migration in hybrid perovskite solar cells with minimal hysteresis," *Nature Communications*, vol. 7, p. 13 831, 2016. [Online]. Available: http://dx.doi.org/10.1038/ncomms13831.

[204] P. Schulz, J. O. Tiepelt, J. A. Christians, I. Levine, E. Edri, E. M. Sanehira, G. Hodes, D. Cahen, and A. Kahn, "High-work-function molybdenum oxide hole extraction contacts in hybrid organic-inorganic perovskite solar cells," *ACS Applied Materials & Interfaces*, vol. 8, no. 46, pp. 31 491–31 499, 2016. [Online]. Available: https://doi.org/10.1021/acsami.6b10898.

[205] M. Yamaguchi, A. Yamamoto, N. Uchida, and C. Uemura, "A new approach for thin film inp solar cells," *Solar Cells*, vol. 19, no. 1, pp. 85–96, 1986. [Online]. Available: http://www.sciencedirect.com/science/article/pii/0379678786900529.

[206] S. Hubbard, C. Bailey, S. Polly, C. D. Cress, J. Andersen, D. V. Forbes, and R. P. Raffaelle, "Nanostructured photovoltaics for space power," *Journal of Nanophotonics*, vol. 3, no. 1, pp. 1 –16, 2009. [Online]. Available: https://doi.org/10.1117/1.3266502.

[207] C. Kerestes, D. Forbes, C. G. Bailey, J. Spann, B. Richards, P. Sharps, and S. Hubbard, "Radiation effects on quantum dot enhanced solar cells," in *Physics, Simulation, and Photonic Engineering of Photovoltaic Devices*, A. Freundlich and J.-F. F. Guillemoles,

Eds., International Society for Optics and Photonics, vol. 8256, SPIE, 2012, pp. 317 –326. [Online]. Available: https://doi.org/10.1117/12.910835.

[208] C. Kerestes, C. D. Cress, B. C. Richards, D. V. Forbes, Y. Lin, Z. Bittner, S. J. Polly, P. Sharps, and S. M. Hubbard, "Strain effects on radiation tolerance of triple-junction solar cells with InAs quantum dots in the GaAs junction," *IEEE Journal of Photovoltaics*, vol. 4, no. 1, pp. 224–232, Jan. 2014.

[209] H. Esmaielpour, V. R. Whiteside, J. Tang, S. Vijeyaragunathan, T. D. Mishima, S. Cairns, M. B. Santos, B. Wang, and I. R. Sellers, "Suppression of phonon-mediated hot carrier relaxation in type-II InAs/$AlAs_xSb_{1-x}$ quantum wells: A practical route to hot carrier solar cells," *Progress in Photovoltaics: Research and Applications*, vol. 24, no. 5, pp. 591–599, 2016. [Online]. Available: https://onlinelibrary.wiley.com/doi/abs/10.1002/pip.2763.

[210] H. Esmaielpour, V. R. Whiteside, H. P. Piyathilaka, S. Vijeyaragunathan, B. Wang, E. Adcock-Smith, K. P. Roberts, T. D. Mishima, M. B. Santos, A. D. Bristow, and I. R. Sellers, "Enhanced hot electron lifetimes in quantum wells with inhibited phonon coupling," *Scientific Reports*, vol. 8, no. 1, p. 12 473, 2018. [Online]. Available: https://doi.org/10.1038/s41598-018-30894-9.

[211] V. R. Whiteside, B. A. Magill, M. P. Lumb, H Esmaielpour, M. A. Meeker, R. R. H. H. Mudiyanselage, A Messager, S Vijeyaragunathan, T. D. Mishima, M. B. Santos, I Vurgaftman, G. A. Khodaparast, and I. R. Sellers, "Valence band states in an InAs/AlAsSb multi-quantum well hot carrier absorber," *Semiconductor Science and*

Technology, vol. 34, no. 2, p. 025 005, Jan. 2019. [Online]. Available: https://doi.org/10.1088%2F1361-6641%2Faae4c3.

[212] V. R. Whiteside, H Esmaielpour, T. D. Mishima, K. R. Dorman, M. B. Santos, D. K. Ferry, and I. R. Sellers, "The role of intervalley phonons in hot carrier transfer and extraction in type-II InAs/AlAsSb quantum-well solar cells," *Semiconductor Science and Technology*, vol. 34, no. 9, p. 094 001, Jul. 2019. [Online]. Available: https://doi.org/10.1088%2F1361-6641%2Fab312b.

[213] M. P. Lumb, I. Vurgaftman, C. A. Affouda, J. R. Meyer, E. H. Aifer, and R. J. Walters, "Quantum wells and superlattices for III-V photovoltaics and photodetectors," in *Next Generation (Nano) Photonic and Cell Technologies for Solar Energy Conversion III*, L. Tsakalakos, Ed., International Society for Optics and Photonics, vol. 8471, SPIE, 2012, pp. 13–22. [Online]. Available: https://doi.org/10.1117/12.964654.

[214] H. Esmaielpour, V. R. Whiteside, L. C. Hirst, J. G. Tischler, R. J. Walters, and I. R. Sellers, "The effect of an InP cap layer on the photoluminescence of an $In_xGa_{1-x}As_{1-y}P_y$/$In_zAl_{1-z}As$ quantum well heterostructure," *Journal of Applied Physics*, vol. 121, no. 23, p. 235 301, 2017. [Online]. Available: https://doi.org/10.1063/1.4985614.

[215] A. M. Gilinsky, D. V. Dmitriev, A. I. Toropov, and K. S. Zhuravlev, "Defect-related luminescence in InAlAs on InP grown by molecular beam epitaxy," *Semiconductor Science and Technology*, vol. 32, no. 9, p. 095 009, Aug. 2017. [Online]. Available: https://doi.org/10.1088%2F1361-6641%2Faa78c6.

[216] M. Sacilotti, P. Abraham, M. Pitaval, M. Ambri, T. Benyattou, A. Tabata, M. A. G. Perez, P. Motisuke, R. Landers, J. Morais, A. L. Corre, and S. Loualiche, "Structural

and optical properties of AlInAs/InP and GaPSb/InP type II interfaces," *Canadian Journal of Physics*, vol. 74, no. 5-6, pp. 202–208, 1996. [Online]. Available: https://doi.org/10.1139/p96-032.

[217] D. Vignaud, X. Wallart, F. Mollot, and B. Sermage, "Photoluminescence study of the interface in type II InAlAs-InP heterostructures," *Journal of Applied Physics*, vol. 84, no. 4, pp. 2138–2145, 1998. [Online]. Available: https://doi.org/10.1063/1.368275.

[218] N. N. Ledentsov, J. Böhrer, M. Beer, F. Heinrichsdorff, M. Grundmann, D. Bimberg, S. V. Ivanov, B. Y. Meltser, S. V. Shaposhnikov, I. N. Yassievich, N. N. Faleev, P. S. Kop'ev, and Z. I. Alferov, "Radiative states in type-II GaSb/GaAs quantum wells," *Phys. Rev. B*, vol. 52, pp. 14 058–14 066, 19 Nov. 1995. [Online]. Available: https://link.aps.org/doi/10.1103/PhysRevB.52.14058.

[219] M. Jo, M. Sato, S. Miyamura, H. Sasakura, H. Kumano, and I. Suemune, "Origin of the blueshift of photoluminescence in a type-II heterostructure," *Nanoscale Res Lett*, vol. 7, no. 1, p. 654, 2012.

Appendix A

Basic Programming for Data Acquisition

A.1 C# programming basics

Most of the data acquisition is performed by programs written using C#.NET in Microsoft Visual Studio. A windows forms application is created, and then buttons, dialog boxes, charts, and other GUI tools can be placed in the program window. Each of these GUI tools requires a specific name, and creates code linked to the object. If/then statements, while loops, for loops, and other standard programming methods can then be used for generating the proper user interface, and for collecting, displaying, and saving data.

As most older scientific equipment comes standard with a GPIB interface, it is imperative to understand how to use this communication standard. Programming for GPIB instruments in C#.NET begins with the installation of a code interface library. The National Instruments Virtual Instrument Software Architecture (NI-VISA) provides an interface which is consistent between GPIB, USB, Ethernet, and other types of communication. In our case, the appropriate software typically accompanied the drivers for a GPIB-USB adapter, and can be found on either the National Instruments or Keysight (formerly Agilent) websites.

Once the NI-VISA software is installed, simple communication with the instrument can be initiated through the software, sometimes referred to as Interactive I/O. This simple method of sending commands and reading the response is useful for testing, and is similar to how the windows forms application will work with the instrument. Most scientific instruments have a

portion of their manual dedicated to programming and the types of commands that can be issued.

In order to access the NI-VISA commands, the appropriate reference will need to be included in your C#.NET project. Then a message based session can be defined, and opened at the proper GPIB address that is set on the instrument. With the session open, the program can now write commands to the instrument, and read the responses. Example code for opening a session, writing to the instrument, reading the response, and closing the session is shown below.

```
using NationalInstruments.VisaNS;

//Opening VISA session

private MessageBasedSession mySession;

//Connecting to instrument
//Open Message Based VISA session

try
{
        mySession = (MessageBasedSession)ResourceManager.GetLocalManager().
            Open(MyGlobals.mySession);
}
catch (InvalidCastException)
{
        MessageBox.Show("Resource selected must be a message-based session");
}
catch (Exception exp)
{
        MessageBox.Show(exp.Message);
        return;
}

//Writing to the instrument

try
{
        mySessions.Write("COMMAND HERE");
}
```

```
catch (Exception exp)
{
        MessageBox.Show(exp.Message);
}

//Reading from instrument - usually involves a previous write command
//In this case a string is read, and parsed to a double

new double value;

try
{
        mySession.Write("READ COMMAND HERE");
        Double.TryParse(mySession.ReadString(), out value);
}
catch (Exception exp)
{
        MessageBox.Show(exp.Message);
}

//Closing the session

mySession.Terminate();
```